Dissertation

submitted to the

Combined Faculty of Natural Sciences and Mathematics

of Heidelberg University, Germany

for the degree of

Doctor of Natural Sciences

Put forward by

Kathrin Bartelheimer

born in: Castrop-Rauxel

Oral examination: January 22nd, 2020

A Heterogeneous and Multi-Range Soft-Tissue Deformation Model for Applications in Adaptive Radiotherapy

Referees: Prof. Dr. Joao Seco

Prof. Dr. Oliver Jäkel

A Heterogeneous and Multi-Range Soft-Tissue Deformation Model for Applications in Adaptive Radiotherapy

During fractionated radiotherapy, anatomical changes result in uncertainties in the applied dose distribution. With increasing steepness of applied dose gradients, the relevance of patient deformations increases. Especially in proton therapy, small anatomical changes in the order of millimeters can result in large range uncertainties and therefore in substantial deviations from the planned dose. To quantify the anatomical changes, deformation models are required. With upcoming MR-guidance, the soft-tissue deformations gain visibility, but so far only few soft-tissue models meeting the requirements of high-precision radiotherapy exist. Most state-of-the-art models either lack anatomical detail or exhibit long computation times.
In this work, a fast soft-tissue deformation model is developed which is capable of considering tissue properties of heterogeneous tissue. The model is based on the chainmail (CM)-concept [1, 2], which is improved by three basic features. For the first time, rotational degrees of freedom are introduced into the CM-concept to improve the characteristic deformation behavior. A novel concept for handling multiple deformation initiators is developed to cope with global deformation input. And finally, a concept for handling various shapes of deformation input is proposed to provide a high flexibility concerning the design of deformation input.
To demonstrate the model flexibility, it was coupled to a kinematic skeleton model for the head and neck region [3, 4], which provides anatomically correct deformation input for the bones. For exemplary patient CTs, the combined model was shown to be capable of generating artificially deformed CT images with realistic appearance. This was achieved for small-range deformations in the order of interfractional deformations, as well as for large-range deformations like an arms-up to arms-down deformation, as can occur between images of different modalities. The deformation results showed a strong improvement in biofidelity, compared to the original chainmail-concept, as well as compared to clinically used image-based deformation methods. The computation times for the model are in the order of 30 min for single-threaded calculations, by simple code parallelization times in the order of 1 min can be achieved.
Applications that require realistic forward deformations of CT images will benefit from the improved biofidelity of the developed model. Envisioned applications are the generation of plan libraries and virtual phantoms, as well as data augmentation for deep learning approaches. Due to the low computation times, the model is also well suited for image registration applications. In this context, it will contribute to an improved calculation of accumulated dose, as is required in high-precision adaptive radiotherapy.

Ein Heterogenes und "Multi-Range" Deformationsmodell für Weichgewebe für Anwendungen in der Adaptiven Strahlentherapie

Anatomische Veränderungen im Laufe der fraktionierten Strahlentherapie erzeugen Unsicherheiten in der tatsächlich applizierten Dosisverteilung. Je steiler die Dosisgradienten in der Verteilung sind, desto größer wird der Einfluss von Patientendeformationen. Insbesondere in der Protonentherapie erzeugen schon kleine anatomische Veränderungen im mm-Bereich große Unsicherheiten in der Reichweite und somit extreme Unterschiede zur geplanten Dosis. Um solche anatomischen Veränderungen zu quantifizieren, werden Deformationsmodelle benötigt. Durch die aufkommenden Möglichkeiten von MR-guidance gewinnt das Weichgewebe an Sichtbarkeit. Allerdings gibt es bisher nur wenige Modelle für Weichgewebe, welche den Anforderungen von hochpräziser Strahlentherapie genügen. Die meisten Modelle berücksichtigen entweder nicht genügend anatomische Details oder benötigen lange Rechenzeiten.
In dieser Arbeit wird ein schnelles Deformationsmodell für Weichgewebe entwickelt, welches es ermöglicht, Gewebeeigenschaften von heterogenem Gewebe zu berücksichtigen. Dieses Modell basiert auf dem Chainmail (CM)-Konzept [1, 2], welches um drei grundlegende Eigenschaften erweitert wird. Rotationsfreiheitsgrade werden in das CM-Konzept eingebracht, um das charakteristische Deformationsverhalten zu verbessern. Es wird ein neues Konzept für multiple Deformationsinitiatoren entwickelt, um mit globalem Deformationsinput umgehen zu können. Und zuletzt wird ein Konzept zum Umgang mit verschiedenen Formen von Deformationsinput vorgestellt, welches eine hohe Flexibilität für die Kopplung zu anderen Modellen ermöglicht.
Um diese Flexibilität des Modells zu zeigen, wurde es mit einem kinematischen Skelettmodell für die Kopf-Hals-Region gekoppelt [3, 4], welches anatomisch korrekten Input für die Knochen liefert. Basierend auf exemplarischen Patientendatensätzen wurde gezeigt, dass das gekoppelte Modell realistisch aussehende, künstlich deformierte CTs erzeugen kann. Dies war sowohl für eine kleine Deformation im Bereich von interfraktionellen Bewegungen als auch für eine große Deformation, wie z.B. eine arms-up zu arms-down Bewegung, welche zwischen multimodalen Bildern auftreten kann, möglich. Die Ergebnisse zeigen eine starke Verbesserung der Biofidelity im Vergleich zum CM-Modell, und auch im Vergleich zu klinisch eingesetzten bildbasierten Deformationsmodellen. Die Rechenzeiten für das Modell liegen im Bereich von 30 min für single-threaded Berechnungen. Durch einfache Code-Parallelisierung können Zeiten im Bereich von 1 min erreicht werden.
Anwendungen, die realistische CTs aus Vorwärtsdeformationen benötigen, werden von der verbesserten Biofidelity des entwickelten Modells profitieren. Mögliche Anwendungen sind die Erstellung von Plan-Bibliotheken und virtuellen Phantomen sowie Daten-Augmentation für deep-learning Ansätze. Aufgrund der geringen Rechenzeiten ist das Modell auch für Anwendungen in der Bildregistrierung gut geeignet. In diesem Kontext wird es zu einer verbesserten Berechnung der akkumulierten Dosis beitragen, welche für hochpräzise adaptive Strahlentherapie benötigt wird.

Erklärung

Ich erkläre hiermit, dass ich die vorgelegte Dissertation selbst verfasst und mich dabei keiner anderen, als der von mir ausdrücklich bezeichneten Quellen und Hilfen bedient habe.

Heidelberg, den 11.11.2019

.....

Contents

Acronyms

ART	Adaptive radiotherapy
CBCT	Conebeam computed tomography
CM	Chainmail
CT	Computed tomography
CTV	Clinical target volume
DIR	Deformable image registration
DVF	Displacement vectorfield
ECM	Enhanced chainmail
FE	Finite element
HN	Head and neck
HU	Hounsfield
IGRT	Image-guided radiotherapy
IMRT	Intensity modulated radiotherapy
MR	Magnetic resonance
OAR	Organ at risk
TPS	Thin-plate splines

1. Introduction

In radiotherapy, dose application is planned based on a patient CT which is obtained prior to treatment. However, this planning CT is only a snapshot of the patient anatomy. In the course of fractionated treatment, anatomical changes occur, due to e.g. posture changes or volume changes. The resulting anatomical uncertainty increases the risk of considerable deviations between the planned dose distribution and the actually delivered dose [5]. Especially for steep dose gradients as are applied in particle therapy, even small interfractional deformations can result in an underdosage of the tumor or an overdosage of the organs at risk (OARs). Therefore, the anatomical uncertainties compromise the potential of high-precision conformal irradiation techniques like intensity modulated radiotherapy or particle therapy.
An exemplary body site, in which conformal treatment is required since target volumes are located close to OARs, is the head-and-neck region. In this highly flexible region, anatomical changes occur due to local setup variations [6] or volume regression [7]. The main dosimetric consequences were shown to be significantly increased doses to OARs and normal tissue [8].
One approach to correct for the observed anatomical uncertainties is adaptive radiotherapy (ART). Based on patient images, the dose which is actually applied to the deformed anatomy can be monitored, with the goal to achieve a better sparing of OARs and normal tissue. For the monitoring, a spatial correspondence between the planning CT and the fraction CTs is required. This correspondence is obtained by deformation models which provide displacement vector fields (DVFs) describing the observed anatomical deformations.

Deformation models provide representations of volumetric objects in combination with rules describing their deformation behavior. In the field of radiotherapy, such models are often embedded into deformable image registration algorithms which optimize model parameters to find the best deformation between two given images. In this context, the role of the deformation model is to limit the space of all possible transformations to physically plausible and anatomically reasonable ones [9].
In general, the level of model detail is limited by the computational efficiency. On the one hand, there are interpolation-based models like radial basis-functions or thin-plate-splines. These models require only low computation times, but also have a low level of detail. Moreover, for model input a regular distribution of control points is needed which is difficult to provide for patient data used in radiotherapy, especially in regions of homogeneous tissue.
On the other hand, there are physical-based models like mass-spring or finite-element models. Such models are capable of considering anatomical information during the deformation process, in the form of e.g. tissue properties and anatomical boundary conditions. However, the increased level of detail comes at the cost of increasing times for model set-up and computation. Especially for large-range deformations, the model parameterizations become more complex and computation time further increases.

The goal of this work is to develop a concept for a biomechanical soft-tissue deformation model. This model has to describe small-range deformations as occur between different treatment fractions, as well as large-range deformations as occur between images from different modalities. Deformation magnitudes shall range from posture changes in the order of millimeters to extreme deformations like an arms-up to arms-down movement. The main requirements to the model results are low computation times in combination with a high biofidelity of deformation results. The soft-tissue deformation model is based on the chainmail (CM)-approach [1, 2], which is faster than most physical-based models, but offers a higher level of anatomical detail

than interpolation-based models. Major advantages of this approach are the possibility to consider tissue heterogeneity [10], and a fast model set-up due to automatic image-based model parameterization. Moreover, the CM-approach exhibits low runtimes in the order of minutes for high-resolution deformations on voxel level. By code parallelization even real-time performance can be achieved [11]. Major limitations of the existing CM-approaches are missing rotational degrees of freedom and the consideration of only single control points for deformation input, as well as missing concepts for controlling the voxel volumes during the deformation process.
The final deformation model is required to consider anatomical information like tissue properties and to handle complex anatomical input to achieve a high biofidelity. The quantitative evaluation of the deformation results will be based on the Jacobian as an exemplary DVF regularity index, as well as on anatomical landmarks for an estimation of the model accuracy.

2. Background

In this chapter, a brief overview of the influence of patient deformations during the radiotherapy process and the different ways to handle them in clinical applications is given. Then the basic concepts of relevant deformation models are presented, concerning the advantages and disadvantages for applications in radiotherapy. Finally, detailed deformation models, which are applied in radiotherapy are presented, together with the different methods used for model validation and exemplary model applications.

2.1. Patient Deformation in Radiotherapy

This section describes the radiotherapy process, as well as irradiation techniques and imaging modalities, focusing on those aspects relevant for the management of patient deformations. Then the different patient deformations occurring during radiotherapy as well as the techniques applied to minimize the effect of deformations on the radiotherapy outcome are outlined. Finally, occurring deformations and their handling for head and neck patients are depicted.

2.1.1. Relevant Radiotherapy Processes and Techniques

Radiotherapy Treatment Process This paragraph follows the description of the radiotherapy treatment process in the bookchapter of Karger [12]. The principal process of radiotherapy treatment is depicted in Fig. 1a. It can be divided into the planning phase and the treatment phase. Prior to treatment, in the planning phase, the patient is immobilized in a posture as similar as possible to the future treatment position. Then a planning computed tomography (CT) image is acquired, which represents a snapshot of the patient's anatomy. In Fig. 1b a sagittal slice of such a planning CT of a head and neck (HN)-patient is shown. In the next step, the planning CT is used to delineate relevant anatomical structures, which are the clinical target volume (CTV) and relevant organs at risk (OARs). In Fig. 1c the contours for the CTV (red and pink) and for the spinal cord (yellow) and the brain stem (green) as exemplary OARs are depicted. Contouring is usually done manually, automatic segmentation still is a field of research. Based on the patient anatomy and on the dose prescribed by the physician, in a third step the treatment plan is generated. The plan generation is an iterative process, during which parameters of the treatment device are optimized to obtain a dose distribution with high doses in the tumor while sparing the OARs and the surrounding tissue. In Fig. 1d an exemplary dose distribution is illustrated, which applies a high dose (red) to the tumor and low doses (blue) to the OARs. In between steep dose gradients occur. These first three steps make up the planning phase, which is followed by the irradiation phase.
Before each treatment, the patient is immobilized in the treatment position, to achieve small deviations from the position in the planning CT. Then the patient is usually imaged in treatment position to verify correct positioning, in case of large deviations, the patient has to be repositioned. In the last step, the dose is applied according to the treatment plan.
For radiobiological reasons, the delivery of the total prescribed dose is often split into several fractional treatments, so that the total duration of the irradiation phase makes up 6-7 weeks with 20-30 fractions.

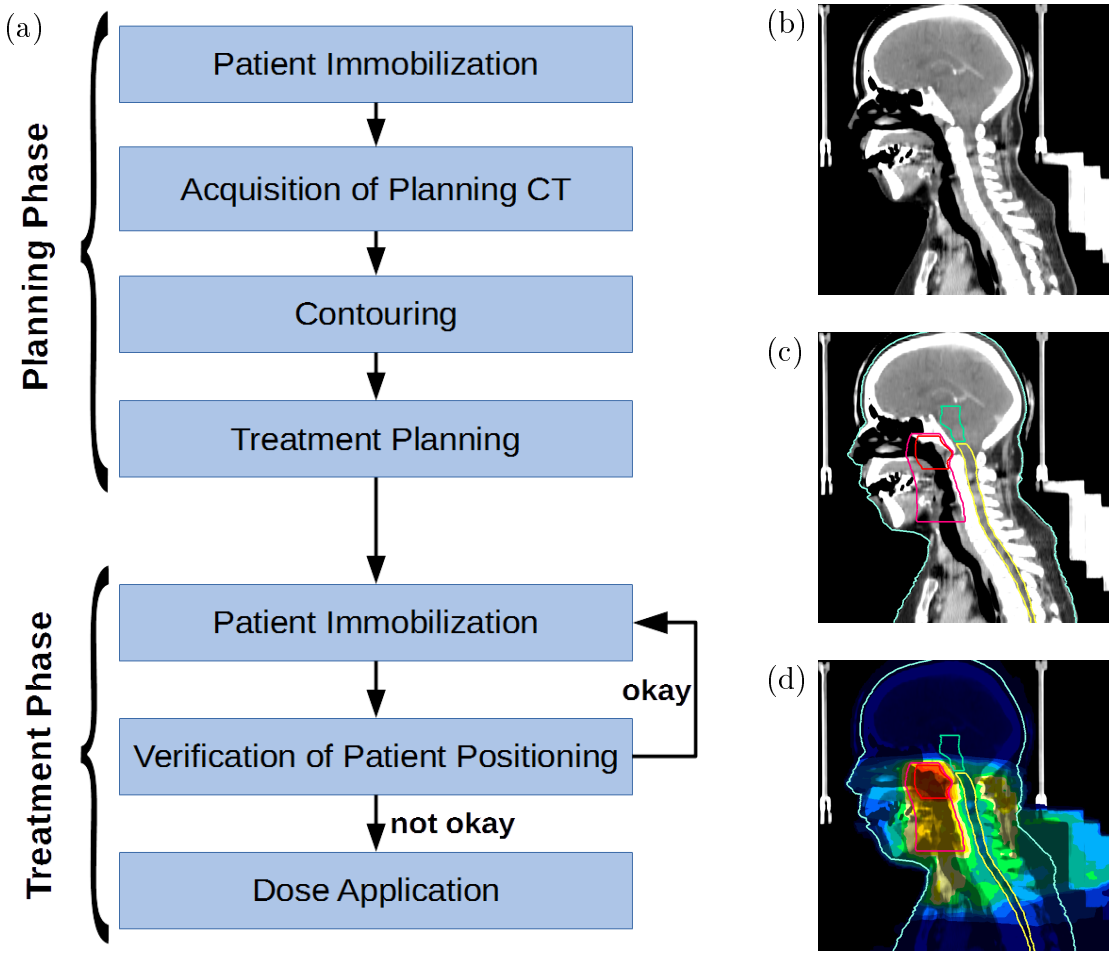

Figure 1.: (a) Flowchart, illustrating the basic RT process, which is divided into a planning and a treatment phase. (b-d) Sagittal slices of an exemplary HN-patient, illustrating the different steps of the planning phase. (b) Planning CT (c) Contoured planning CT (d) Dose distribution overlayed on the planning CT. The color map illustrates the transitions from high dose (red) to low dose (blue).

Irradiation Techniques The two main types of radiation used in radiotherapy are photons and ions. For photons, the depth-dose-curve depicting the energy deposition along the beam path follows an exponential decay (Fig. 2a). Therefore, the highest dose is deposited close to the patient's surface. The dose distribution is focused to the tumor region, by using irradiation fields from different directions. For complex geometries, however, this is not sufficient, since e.g. OARs cannot be spared (Fig. 2b). For such complex geometries of tumor and OARs, the highly conformal intensity-modulated radiotherapy (IMRT) was developed (Fig 2c). In IMRT, complex irradiation fields are realized by modulating the intensity of the individual beams (Fig 2c). This results in a conformal radiation field with steep dose gradients, which allow for a better sparing of OARs. For particles, the deposited energy does not exponentially decrease along the beam path, but the major part of the energy is released in a very small local area, the Bragg peak (Fig. 2a). The position of the Bragg peak highly depends on the tissue densities types along the beam path. Due to the shape of the depth-dose curve, particle therapy inherently allows for steep dose gradients and therefore for conformal treatment. The main goal of conformal techniques like IMRT and particle therapy is a better sparing of the OARs. This is achieved by a more

conformal dose application, resulting in the already mentioned steep dose gradients in the final dose distribution.

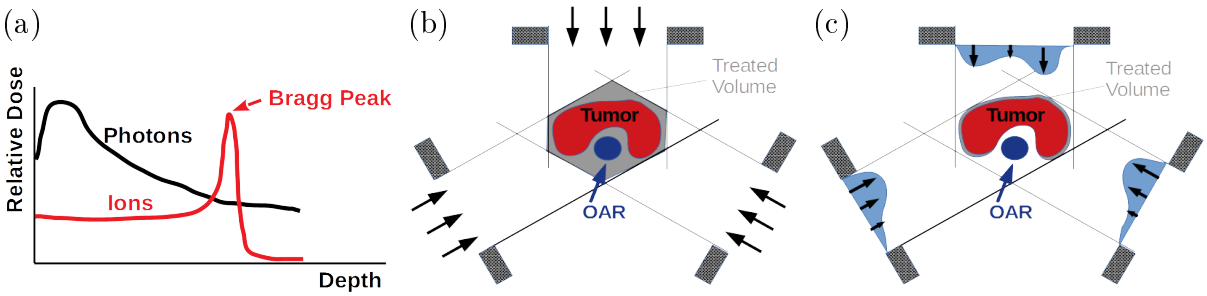

Figure 2.: (a) Schematic depth-dose-curves for photons (black) and ions (red). The Bragg Peak is indicated by the red arrow. (b) Illustration of non-conformal treatment with three beam directions. The irradiated area, which also covers the OAR, is indicated in dark grey. (c) Illustration of conformal IMRT treatment with three beam directions. The irradiated area, which is conformal to the tumor, is indicated in dark grey. Subfigures b and c are adjusted according to Figure 1 in [13].

Imaging Modalities In the following, a short overview of the role of different imaging modalities in radiotherapy is given [14]. Imaging plays a very important role in radiotherapy application since it offers the possibility to locate the tumor and OARs as well as to observe and possibly correct for anatomical changes in the patient. The most important modalities are computed tomography (CT) and magnetic resonance (MR) imaging. CT images are the standard imaging modality in radiotherapy. They are currently the only means for quantitatively characterizing the electron densities in tissue, which are required for dose calculation in photon irradiation and for an approximation of the stopping power map in ion irradiation. The two main techniques to obtain CT images are fan-beam CT and cone-beam CT (CBCT). Fan-beam CTs provide better soft-tissue contrast and bone resolution and are therefore suitable for diagnostics and planning. CBCTs involve lower doses than fan-beam CTs and are therefore better suited for regular control imaging. However, they have higher beam scattering and often a smaller field of view, offering only limited image quality. In contrast to CT images, MR images are acquired with non-ionizing radiation and have a much higher soft-tissue contrast. This makes them well suited for daily imaging. However, MR imaging is sensitive to disturbances of the magnetic field, which can result in image distortions.

2.1.2. Anatomical Changes in the Patient

In the course of radiotherapy, changes in the patient anatomy occur on different time-scales and introduce uncertainties into the irradiation process. During the individual treatment sessions, intrafractional deformations like organ motion due to breathing occur. In between the fractions, interfractional deformations occur, which mainly result from set-up variations and volume changes due to weight loss or tumor response. In the following, the focus is set to interfractional deformations, their consequences, and the appropriate handling.
Figure 3 illustrates typical deformations for an exemplary head and neck (HN)-patient between the planning CT and a fraction CT. Especially for the spinal cord (yellow contour), the positional changes between the fractions are visible. Anatomical deformations as those depicted in Fig. 3 have an influence on the planned dose distribution (Fig. 1d). For photon irradiation, deformations smear out the dose distribution. For particles, however, the dose deposition is much more

sensitive to the tissue densities along the beam path, so deformations even influence the shape of the dose distribution. In summary, anatomical changes compromise the accuracy that can be achieved by conformal irradiation techniques like IMRT or particle therapy. In regions of steep dose gradients, even small deformations can result in underdosage of the tumor or overdosage of OARs and normal tissue. Therefore, approaches for the handling of deformations are required.

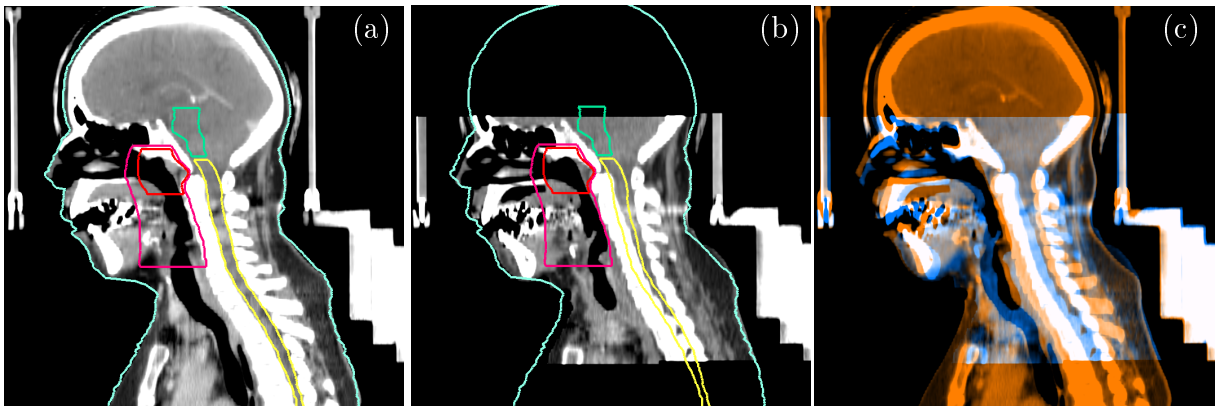

Figure 3.: Illustration of typical interfractional anatomical changes. (a) Contoured planning CT. (b) Fraction CT with a limited field of view. The contours of the planning CT are shown as an overlay. The contour of the spinal cord (yellow) does not fit the deformed anatomy any more. (c) Image fusion of planning CT (orange) and fraction CT (blue).

2.1.3. Management of Deformations

The traditional approach for handling anatomical changes is to introduce margins around the clinical target volume to take into account the smeared out dose distribution [15]. In this way, target coverage is ensured in the presence of positional uncertainties, however at the cost of increased doses to the surrounding organs and healthy tissue. To fully exploit the technically possible accuracy of conformal dose application techniques, new concepts for motion management are required. In this context, image-guided radiotherapy (IGRT) was established [16]. Right before each treatment session, a 3D patient image is obtained in treatment position. This is used to control the position of the tumor and OARs. If deviations concerning the positions in the planning CT occur, the couch position is readjusted to realign relevant structures. However, relative patient deformations like posture changes, weight loss or tumor regression are still not corrected for in this approach.

Adaptive Radiotherapy Corrections for such relative deformations are addressed in adaptive radiotherapy (ART), which was introduced first by Yan et al. [17]. In ART image feedback is used for a patient-specific adjustment of the whole treatment process of imaging, treatment planning and dose delivery (Fig. 1a). The basic idea is to monitor the patient during each treatment fraction to adjust the treatment plan in case of relevant anatomical deformations. During each treatment fraction, the actual influence of the anatomical changes on the dose distribution is determined by recalculation of the dose distribution, the so-called dose-of-the-day. This recalculation can be performed directly on the daily CBCT if the quality is sufficient. If not, a deformation model is used to describe the deformation that has taken place between the timepoint of the planning CT and the fraction CBCT. Based on this deformation, the planning CT is artificially deformed and used for the dose recalculation. The recalculated dose distribution

is used as a decision criterion to evaluate if the original treatment plan, obtained from the planning CT is suitable for the deformed anatomy or if replanning is required.
The main advantage of ART is a greater sparing of OARs and normal tissue, since it allows for the application of steep dose gradients, even in the presence of patient deformations. However, the application of ART, in general, is very time-consuming, so that it is not regularly used in clinical routine.

2.1.4. Head and Neck Patients

An exemplary body site, in which target volumes are located close to OARs and in which conformal treatment planning is required, is the head-and-neck (HN) region. In Fig. 4 the anatomy of the HN-region is depicted. The most relevant OARs that have to be considered during treatment planning, are the parotid glands, the spinal cord, the brainstem, and the optical nerves.

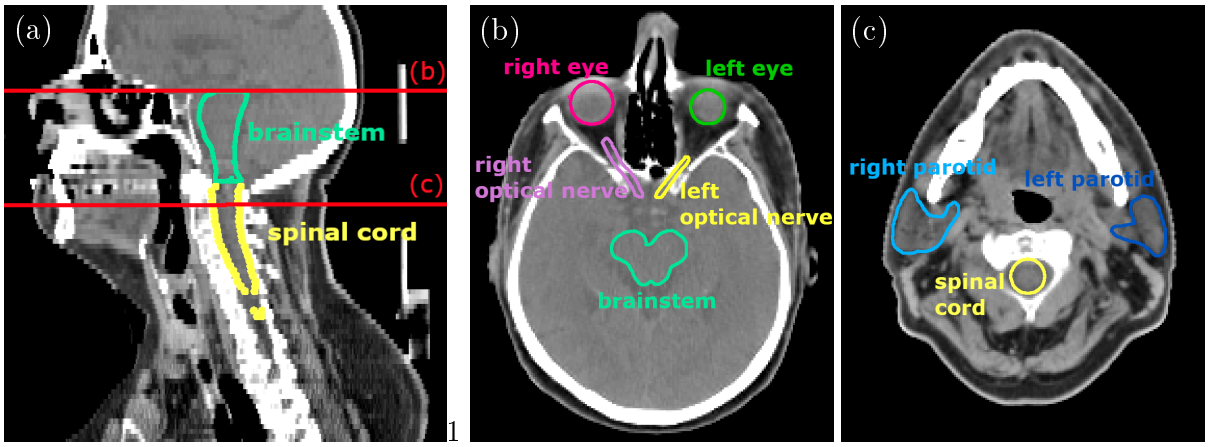

Figure 4.: Illustration of OARs in the HN-region. The positions of the transversal slices (b) and (c) are indicated by the red lines in the sagittal slice (a).

Due to local setup variations [6] or volume regression [7], large anatomical changes can occur in the HN-region. Exemplary posture changes during setup are neck flexion, head turn, spine flexion and variations in the shoulder positioning. Resulting local setup uncertainties are in the range of 3-4 mm [6]. Exemplary volume changes that can occur are tumor growth or shrinkage, volume regression in OARs or general weight loss of the patient. The dosimetric consequences of these anatomical changes are overdosage of OARs [8, 18, 19] as well as of underdosage of the target volume [20]. The magnitude of the dosimetric consequences depends on several factors like the location of target volumes, the proximity of OARs to high-dose regions or local dose gradients [8].
For the immobilization of HN-patients, thermoplastic facemasks are used which are built prior to treatment. For patient alignment, external markers can be placed on the mask [18]. Based on the alignment of these markers with lasers installed in the treatment room, offline setup corrections can be performed. However, this considers neither patient setup displacements inside the facemask nor internal anatomic variations [21]. Van Kranen et al. report the application of 5 mm margins for such offline setup corrections [6]. Since the mean parotid dose is reported to linearly increase with increasing margins, with approximately 1.3 Gy per 1 mm [21], a reduction of these margins is desirable. With IGRT, pre-treatment images are used for improved patient

alignment. Based on e.g. the alignment of the bones, patient setup displacements inside the facemask can be ruled out. This allows a reduction of margins to 3-4 mm [18]. However, internal relative anatomic variations are still not considered. The huge amount of images acquired during IGRT can be further exploited by ART.
The main dosimetric benefit of ART in the HN-region is a decreasing mean dose to the parotids [22, 23]. Additional benefits were reported for the oral cavity [8, 22], the base of the tongue and larynx [22] as well as for the spinal cord [8]. The optimal number and time of replannings are unclear [24]. It was shown that one replan during mid-treatment can provide relevant dosimetric improvements compared to IGRT [25]. Castelli et al. [24] propose a daily registration of the bones to correct for set-up errors combined with a weekly replanning to correct for anatomical variations. Since replanning, in general, is very resource-intensive, it is further proposed to predict patients who will benefit from ART most [26].

2.2. Basic Deformation Models

This section gives an overview of the basic concepts of commonly applied deformation models in radiotherapy. In the end, a summary of the advantages and disadvantages of the different models concerning soft-tissue deformations in radiotherapy will be given.
Deformation models, in general, provide representations of volumetric objects and define deformation rules describing the deformation behavior. Rigid transformations resulting from translation and rotation can be completely described by physical laws and exact analytical solutions are available. For soft tissue, however, the deformation behavior has to be predicted based on initial forces or displacements and under consideration of additional constraints. Due to the complexity of soft-tissue deformations, classical physics approaches are not analytically solvable any more. Therefore, numerous non-physical and approximating physical models have evolved. Depending on the requirements of the particular application, all such models have to find a compromise between the level of detail and the computational efficiency.

2.2.1. Splines

Splines are functions that are defined by piecewise-polynomials. Deformation models based on splines use these functions to interpolate a set of known displacements at certain control points. Depending on the particular approach, spline-based models can have global support like e.g. the free form deformation or the thin-plate splines as well as local support like the B-splines. Some exemplary spline-based models are explained in the following.

Free Form Deformations Free form deformation (FFD) is the simplest form of spline deformation since no additional constraints are assumed [27]. The object to be deformed is embedded into space. Then a rectangular grid, representing the whole space, is deformed under the influence of given control points. Therefore, the embedded object is not actively deformed, but only according to the deformation of the surrounding space.

Radial Basis Functions Radial basis functions (RBFs) have global support and are radially symmetric with respect to the distance to a given point in space. The most general form of a RBF, mapping image points p to deformed image points $t(p)$ is [28]:

$$t(p) = ap + b + \sum_{i=1}^{N} c_i R(p - p_i). \tag{2.1}$$

The deformation consists of a global rotation and translation ($ap + b$) and a local deformation represented by the sum over the radial basis functions $R(p - p_i)$. They can take the form of e.g. Gaussians, multiquadrics, inverse multiquadrics or thin-plate splines (TPS). The coefficients a, b and c_i are determined by solving the given system of equations for all N control points.

Thin-Plate Splines Thin-plate splines (TPS) are one commonly used representative of the RBFs [29]. In two dimensions, its basis function is defined as $R(p - p_i) = (p - p_i)^2 \ln(p - p_i)$. Originally, it is associated with the bending of thin metal pieces, since it minimizes a sort of "bending energy", considering the "bending" forces to act in the given control points.

Basis-Splines The basis-splines (B-splines) define a deformation field on a uniform grid of automatically selected control points Φ_i [30].

$$t(p) = \sum_{i=0}^{N} B_l(p)\Phi_i \tag{2.2}$$

with p being a point in the uniformly spaced deformation grid and $B_l(p)$ representing the lth B-spline basis function. The deformation field cannot be obtained as a closed-form solution but is calculated by optimization of the locations of the control points on the underlying grid. Rueckert et al. [30] introduced the following cost function $C(\Phi) = C_{similarity}(S, M(T)) + \lambda C_{smooth}(T)$, which optimizes image similarity under consideration of a cost function associated with the smoothness of the deformation.

2.2.2. Chainmail Models

Chainmail (CM) models are discrete models, for which the basic concept was proposed by Gibson [1]. They describe a deformable object by a grid of connected CM-elements (Fig.6a). The relative displacement between neighboring CM-elements is restricted by geometric constraints, similar to those of linked elements in a chain (chainmail). If an initial CM-element is displaced, the neighboring CM-elements absorb this deformation by moving closer together or farther away from each other as illustrated in Fig. 6b. The relative displacement between neighboring CM-elements is restricted by geometric constraints, which parameterize material elasticity. These constraints not directly correspond to real, measurable material properties, but are a measure for material stiffness. In a very elastic material, the constraints allow large relative displacements, so that a small displacement is quickly absorbed and only has a very local effect. In a stiff material, relative displacements are small and even small initial displacements are hardly absorbed and have a global effect. Since the resulting configuration usually not is a minimum energy configuration, the deformation is followed by a second step, in which an elastic relaxation is applied to the grid as a kind of regularization [1].

2.2.3. Mass-Spring Models

Mass-spring models are also discrete deformation models. They describe a deformable object by a mesh of nodes, which are considered as mass points, and of edges, which are considered as massless springs connecting adjacent nodes [31]. The dynamic behavior of the system follows Newton's Second Law, which is defined separately for the individual mass points x_i with mass m_i:

$$m_i\ddot{x} = -\gamma_i\dot{x}_i - k_i x_i + f_i \tag{2.3}$$

with γ_i being the damping constant, k_i the spring constant approximating material stiffness and f_i an external force. The resulting system of first order differential equations for the whole system is solved by numerical methods.
For the model parameterization, m_i and k_i have to be defined for each mesh node. These parameters do not directly correspond to real material properties and are usually derived in an optimization process. In data-driven approaches, the parameters are optimized to reproduce an observed deformation behavior of the underlying system. In model-driven approaches, the parameters are optimized to reproduce known properties of a reference model [32].

2.2.4. Finite-Element Models

Finite-element (FE) models are a method to solve the partial differential equation (PDEs) which describe the deformation behavior of deformable objects in continuum mechanics. For this purpose, the continuum is discretized by regularly-shaped finite elements, which define a mesh of nodes. This allows the transformation of the PDEs into a system of ordinary differential equations for the displacements of the mesh nodes x:

$$M\ddot{\boldsymbol{x}} + D\dot{\boldsymbol{x}} + K\boldsymbol{x} = \boldsymbol{f} \tag{2.4}$$

with M being the matrix holding all element masses, D being a damping matrix, K being the stiffness matrix and $\boldsymbol{f}$ being the external forces. This system of equations is solved by numerical methods.
For homogeneous and isotropic linear elastic materials, FE-models can be parameterized by Young's modulus Y and the Poisson ratio ν. Young's modulus is a measure of the relation between stress σ and strain ϵ. It is defined as:

$$Y = \frac{\sigma}{\varepsilon}. \tag{2.5}$$

The Poisson ratio is a measure for the relation between transverse strain ϵ_y and axial strain ϵ_x:

$$\nu = -\frac{d\varepsilon_y}{d\varepsilon_x}. \tag{2.6}$$

2.2.5. Summary

In Fig. 5 a classification of the presented models according to their level of detail and the required computation times is given. For spline models, the number and distribution of the control points used as model input, highly influences the quality of the deformation result. Especially for the

description of large-range deformations, a large number of control points is required. Except for the B-splines, most spline-based models have global support, meaning that changes in a single control point, influence the whole deformation field. Tissue properties cannot explicitly be considered in spline-based models. The general computation times of spline-based models are in the order of seconds and therefore very low. However, with an increasing number of control points as required e.g. for large-range deformations, the computational cost increases.
For the chainmail algorithm, the displacement in control points or controlling structures is used as model input. The control points and controlling structures not necessarily have to be equally distributed, but it is important, that they reflect the basic aspects of the underlying deformation. The chainmail is a local model, the individual input information only influences nearby areas. Tissue properties are parameterized by geometric constraints and explicitly considered in the deformation process. The parameterization is tuned to describe realistic deformation behavior, but does not directly correspond to physical material properties. Typical computation times range from minutes to real-time deformations and are not significantly affected by the deformation magnitude.
Mass-spring models are initialized by external forces, which are usually also derived from control points or controlling structures. Tissue properties are parameterized into the node masses and spring constants and tuned to the desired deformation behavior by optimization. Especially stiff tissue like bones requires high spring constants, which results in high computation times. Typical computation times are in the range of several minutes to real-time applications. Overall, MS-models reflect a larger level of anatomical details, at the cost of higher computation times.
Finite element models are initialized by external forces, as well as boundary conditions. The input corresponds directly to the underlying anatomy, in contrast, to e.g. those models, which only use the information of control points. FE-models are the only models, in which the parameterization is based on macroscopic parameters corresponding to actual physical material properties. In most models, deformation behavior is limited to linear elasticity, i.e. small deformations. Modeling of the non-linear regime strongly increases the computation time. Typical computation times are in the order of hours, with additional time required for the model setup, including e.g. the mesh generation.

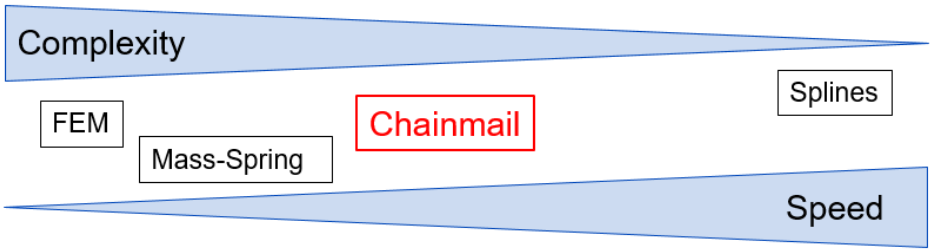

Figure 5.: Classification of the different deformation models according to their level of complexity and computational speed.

All in all, the aspects that should be considered for finding a deformation model suited for a certain application are the required model input, the ability to model tissue heterogeneity and anatomical details in general, the deformation ranges that can be described and the overall time required for model set-up and computation.

2.3. Soft-Tissue Deformation Models in Radiotherapy

In radiotherapy, it can be distinguished between two main application concepts of deformation models - the forward deformation and image registration. For forward deformations, an initial patient image A and the deformation input, initializing the deformation to be described, are required. As output, a displacement vector field (DVF) of the modeled deformation and an artificially deformed image A' are provided. For image registration [9] two patient images A and B, the definition of a metric and an optimizer, as well as possibly additional deformation input, are required. As output, a DVF for the deformation between images A and B is provided. The respective artificially deformed image A', approximating image B, can also be provided. In image registration, the deformation model defines the level of detail of the deformation and it is supposed to restrict the search space for the optimizer to physiologically reasonable results. The provided DVF is therefore not only influenced by the deformation input and the model itself, but also by the choice of metric and optimizer.
Image-based deformation models cannot be applied for forward deformations, since the image information of a second image B is required as model input. Deformation models requiring sets of control points as model input like the spline-based models are also better suited for image registration than for forward deformations, since it is difficult to generate anatomically sensible sets of control points without the guidance of a second image B. For registrations of e.g. HN-patients such models are commonly applied [33].
In the following, the focus is set to models that are suited for forward deformations as well as image registrations. Such models like FE-models, mass-spring models or the CM-model can handle more complex deformation input like boundary conditions derived from the underlying anatomy. Moreover, models of this type allow to include information about the underlying anatomy, e.g. tissue elasticity, into the deformation process.

In radiotherapy, deformation models are needed to account for geometrical changes occurring in the course of the therapy. The development of biomechanical models aims at obtaining physiologically plausible deformations, which are realistic and as accurate as possible. In the following, state-of-the-art biomechanical models for the HN-region, with a focus on soft-tissue deformation, are depicted. Then established evaluation methods, as well as common applications of such biomechanical models in radiotherapy, are presented.

2.3.1. Biomechanical State-of-The-Art Models

Al-Mayah et al. [34] developed a FE-based deformation model for the HN-region. For the model input, the vertebrae (C1-C7), mandible, larynx and the body contour were segmented in the planning CT, as well as in a fraction CT. Each vertebra and the mandible, as well as the body contour, are individually aligned rigidly between the two images. Additional input can be included from modeling dose-induced shrinkage of tumor and salivary glands [35]. The registration of the bones and body contour, as well as the modeling of the volume changes, provided the boundary conditions from which the soft-tissue deformations were calculated by FE-analysis [36].
Kim et al. [37] also developed a FE-based HN deformation model. For the model input, the skull, the mandible and the cervical vertebrae are segmented in two patient images taken at different treatment session. The registration of the bone segmentation provided displacement and force boundary conditions for the bones, from which the respective overall DVF in soft-tissue

was calculated by FE-analysis. Soft tissue is treated as a homogeneous linear elastic material.
Neylon et al. [38] developed a biomechanical HN-model based on mass-spring models. For the model input, tumor and rigid structures were manually contoured in the planning CT. Manual actuation of the rigid skeletal structures provided the deformation input for the soft tissue deformations. For modeling tumor regression, the additional input of the tumor contours is used. The soft tissue is assigned elastic material properties, which correspond to the underlying anatomy.
Vidal et al. [39, 40] developed a CM-based model for describing organ behavior during respiration. For the model input, the deformation of the rib cage is modeled rigidly by a kinematic model. The resulting displacements of the rib cage are used as the boundary conditions for the CM-deformations of the soft tissue in diaphragm and liver.
Pukala et al. [41] developed a biomechanical model for HN-patients, which combines two kinds of basic deformation models. In the first step, head position, mandible position, and weight loss are adjusted locally, allowing only biomechanically sensible deformations of the bones [42]. From the resulting DVF, an intermediate artificially deformed image is created. In this step, the soft tissue is treated heterogeneously, muscles and fat are distinguished as two different tissue categories. In the next step, the intermediate image is used for manual landmark definition with the help of the ImSimQA software. Then a global TPS deformation was applied to successively model spine flexion, shoulder position, and hyoid movement as well as tumor and parotid shrinkage. In this step, soft tissue heterogeneity is not considered. In the end, the DVFs of the biomechanical algorithm and of the manual TPS deformations are combined to a single DVF by DVF composition techniques.

All of the presented HN-models use the bone transformations for initialization of the soft-tissue deformations. Some of them use additional input from the patient outline or from volume changes. Therefore, all of these models require segmentation of the bones, at least in the planning CT. Based on an additional deformation model for the bony structures or on an image registration of the bones, the input for soft tissue deformations is obtained. The soft tissue deformation itself is treated by different methods, which are finite elements, mass-spring, chainmail, and a combination of a not further specified biomechanical deformation and a TPS deformation.
The FE-models are limited to the linear elasticity regime and therefore address only small-range deformations. For the mass-spring model, it is stated to describe clinically relevant ranges of posture changes. Similarly, Pukala et al. state, that their biomechanical model is suited only for deformation magnitudes of typical interfractional posture changes. For the CM-model, deformations in the range of shallow breathing were simulated.
Soft tissue heterogeneity is considered in the mass-spring model and in the model of Pukala et al., which both distinguish between muscle and fat. The elasticity parameters are assigned by automatic segmentation. The FE-models and the CM-model only distinguish between different tissue elasticity for certain organs, but not for the surrounding soft tissue. The elasticity parameters are assigned based on organ segmentation.
Computation times and resolution of the deformation grids, also vary between the models. Neylon et al. [38] achieve real-time deformations for a grid with a 5x higher resolution than the original in-plane data resolution. Al-Mayah et al. [34] use a 5x lower resolution than the original data resolution, with deformation times in the order of 10 minutes. For the remaining models, no information about the computation times was indicated.

2.3.2. Model Validation

Deformation models as the ones describe above, promise to improve radiotherapy treatment outcomes as well as clinical workflows. However, all deformation models show modeling uncertainties, since they only approximate the complex real patient variations. The uncertainties are patient- and case-specific and are influenced e.g. by the quality and content of the underlying patient images, the occurrence of tissue changes like growth and shrinkage and by the choice of the deformation model and the resulting physical fidelity of the DVF [43]. For save clinical applications, a thorough evaluation of model accuracy and physical plausibility is required.
The lack of a gold-standard or ground truth for the modeled deformations, make a straightforward evaluation impossible. Therefore, a large number of evaluation metrics, addressing different deformation characteristics has been proposed [43, 44]. The suitability of the different metrics depends on the particular clinical deformations and on the desired applications [33]. A comprehensive model evaluation requires the combination of different qualitative and quantitative evaluation methods as outlined in a recent AAPM task group report[44]. In the following, a selection of state-of-the-art evaluation methods for radiotherapy applications is presented.

Visual Assessment For visual assessment of the quality of a deformation, visualizations of the DVF itself, as well as of the artificially deformed images A' are used. The DVF is usually visualized by either displacement vectors or by a deformation grid. For 3D deformations, these visualizations can be difficult to interpret. However, obvious irregularities like grid folding or extreme directional changes within the DVF can be detected. The artificially deformed image is obtained by a resampling method. The influence of the resampling method on the image quality should be considered when interpreting resampled images. The image helps to detect deformation errors, which can be visualized by implausible image artifacts like deformed bones or disrupted structures. If a target image B exists, as is the case for image registration applications, a fusion view of A' and B can further help to identify deformation errors. Depending on the specific anatomical site and deformation, different fusion methods are applied [44].

Landmark Evaluation Landmarks are anatomical points defined in the patient images. For landmark evaluation, pairs of landmarks, defined in two corresponding images A and B are required. Therefore, image pairs corresponding to the modeled deformation have to be available. They offer the possibility to estimate the geometric accuracy of a deformation model. This method is not suited for the evaluation of forward deformation modeling. For evaluation, landmarks are defined in image A, deformed by the model DVF to image A' and then compared to landmark positions in image B. The calculation of the residual errors offers a quantitative evaluation metric. Perfect accuracy would result in mean residual values of 0. However, uncertainties in landmark identification in the order of the voxel dimensions are expected, so that the mean residuals are expected to be in a similar order for an accurate deformation model [44].
Landmark evaluation is successfully used in contrast-rich anatomical sites as e.g. lung and thorax [45, 46]. However, error estimation is valid only in the vicinity of defined landmarks. If model accuracy is assessed solely in contrast-rich regions, the results not necessarily reflect the model accuracy in low-contrast regions [47]. For a comprehensive analysis, a regularly distributed and dense landmark distribution is required. Since the definition of landmarks is limited by the image quality and observer performance, its quality and availability vary between anatomical sites. For HN-patients it is hard to find an appropriate distribution of landmarks, so a comprehensive analysis based solely on landmarks is not possible.

Contour-Based Evaluation Contours define the delineations of anatomical structures in patient images (or phantoms). Similar to landmark evaluation, image pairs corresponding to the modeled deformation are required and this method is not suited for the evaluation of forward deformation modeling. Structures are delineated in image A, deformed by the model DVF to image A' and then compared to the delineated structures in image B. The alignment of the contours also is a quantitative measure for model accuracy. A commonly used metric for evaluation is the Dice similarity coefficient (DICE), which is defined as "two times the volume where the two contours overlap, divided by the total volume of both contours combined" [44]. For perfect alignment the DICE-value would approach 1, for diverging contour volumes, it would approach 0. However, similar to landmarks, the quality of contouring is observer-dependent, so that uncertainties in the order of inter-observer variation are expected [43]. Moreover, it should be noted, that small contours inherently have a lower DICE than larger contours [48, 49]. Alternative metrics for contour comparison are the mean distance to agreement(average distance between contours) [44], the center of mass distance (distance between the centers of mass of the contours) and the Hausdorff distance (maximum distance between contour points) [43].
Contour comparisons are widely used for the evaluation of deformations in various anatomical sites [33], including the HN-region [24, 33, 49–52]. However, alignment of contours does not assure, that the DVF is plausible within the contours [33] so that depending on the application further validation methods have to be applied.

DVF Regularity Indices DVF regularity indices are more abstract mathematical methods, that are used to estimate how physically plausible a deformation is [44]. These indices do not refer to image-based information as e.g. landmark- or contour-based evaluation, so only to the DVF itself is required for the evaluation. In contrast to the previously described methods, DVF regularity indices can also be applied to forward deformation modeling. However, DVF regularity indices cannot estimate model accuracy - a DVF can be physically consistent, but still differ from the ground truth. As stated by Paganelli et al. "the consistency check is in fact a necessary but not sufficient condition for an accurate deformation method..." [43]. Therefore, a combination of DVF regularity indices with e.g. landmark evaluation should be executed. In the following, some of the most used regularity indices are presented.
The Jacobian determinant is proposed as a metric that measures the relative volume changes of each image voxel [44]. Jacobian values between 0 and 1 indicate volume reduction, Jacobian values larger than 1 indicate volume expansion and a Jacobian value of 1 represents volume conservation. Negative Jacobians indicate grid-folding. For realistic DVFs the Jacobian should be larger than 0, only in exceptional cases like for sliding motion, grid folding is expected. Moreover, large local changes like differences in the Jacobian values of >10 for neighboring voxels, indicate deformation errors [43, 44]. The Jacobian is widely used for the evaluation of DVF regularity [33, 41], as well as for indication of the shrinkage of structures like the parotids in the HN region [53].
The curl operator is proposed as a metric to identify vortexes in a DVF [54]. If neighboring voxels show large directional changes, the values of the curl operator are high. If neighboring vectors show only small directional changes curl values are low, indicating a physically plausible DVF. Since in soft tissue no circular rotations are expected, the curl-values should ideally be zero. In a first investigative study, clinically valid DVFs showed curl-values between 0 and 5 mm and non-physical DVFs curl-values from 5-10 mm [54].
The inverse consistency error is another metric to estimate the plausibility of a DVF. It requires the modeling of the forward (A to A'/B) and according backward (B/A' to A) deformation and indicates the deviation between the respective DVFs [43]. Low values for the inverse consistency

error "provide evidence of a stable and well understood system" [44]. The absolute error should be in the range of voxel-dimensions [44].

Physical Phantoms Physical phantoms are used to produce an approximated ground truth for a deformation. A set of test images (e.g. A and B) is generated by imaging the phantom in different deformation states. This set of test images is then used as input for the model validation [44]. An advantage of physical phantoms is that markers can be included, even in homogeneous tissue regions, where no landmarks can be found in real patients. These markers provide ground truth landmark positions in the original, as well as in the deformed image. Some phantoms even allow for dosimetric measurements [55, 56]. There exist geometrical phantoms [55, 56], which depict the complex anatomy in a strongly simplified way, and anthropomorphic phantoms [57, 58] tailored for certain anatomical sites. For example, Singhrao et al. [58] developed a detailed anthropomorphic phantom for the HN-region, which allows for a 3D deformation representing neck flexion. A grid of radiotransparent markers with 5 mm spacing in a specified deformation plane, allows for a detailed deformation evaluation.
In general, physical phantoms, especially anthropomorphic ones, require a high workload, so that it is not possible to comprise all clinical scenarios. Still, for exemplary evaluations, physical phantoms do provide an estimated ground truth.

Computational Phantoms Computational phantoms are also used to produce an approximated ground truth. Such phantoms are derived by deforming a patient image A, based on a deformation model, which should be different from the model to be evaluated. The phantom generation results in an approximated ground truth DVF as well as in an artificially deformed image A'. This set of test images (A and A') together with the approximated ground truth DVF is then used as input for the model validation [44]. Since the ground-truth DVF is provided on voxel-basis, detailed spatial errors of the evaluated deformation model can be reported. An advantage of computational phantoms is that they are derived from actual patient images, which improves the clinical relevance in comparison to e.g. physical phantoms. In contrast to physical phantoms, realistic noise and artifact scenarios have to be considered for the creation of computational phantoms [59]. The majority of the virtual phantoms are based on CT images [33, 38, 41, 59], but also some based on MR image exist [60]. Exemplary phantoms for the HN-region model a large neck flexion [33], head rotation and mandible movement [59] as well as volume changes [38, 59].
Depending on the underlying deformation model, the creation of such phantoms is also time-consuming, however, a larger variability of deformations than with physical phantoms can be described. Moreover, it has to be considered, that the phantom is created based on a deformation model, so that a bias towards certain model types can arise. By the combination of different deformation methods during phantom creation, this bias can be weakened [41]. Since models do never completely capture the complexities of real physical processes, it further has to be considered that the underlying DVFs, similarly to DVFs from physical phantoms, are only an approximation of the real deformation process.

Summary In clinical practice, a comprehensive quantitative evaluation is not feasible since it is very time-consuming and since landmarks and contour delineations can only be defined in certain (contrast-rich) regions [43]. The recent AAPM report [44] proposes to use phantoms for general quality assurance. In clinical routine qualitative evaluation should always be performed, with selected complementary quantitative evaluations. Remaining uncertainties have to be interpreted in the anatomical context [54] and if necessary, incorporated into e.g. planning margins. [43].

2.3.3. Model Applications in Radiotherapy

Most applications of deformation models in radiotherapy are found in the context of deformable image registration (DIR). The DVF resulting from the registration is used to map information like structure contours, or dose maps from one image to the other. Applications involving forward deformations are found e.g. in the creation of computational phantoms for DIR benchmarking. Depending on the particular application, the DVFs have to satisfy different accuracy requirements, as discussed in the following.

Contour Propagation

The recontouring of patient data makes up a very time-consuming part of the replanning process of ART. The complete delineation of a single patient data set can take up to 2.5 hours [24]. Automatic contour propagation, applied based on the DVF obtained from image registration, can significantly reduce the delineation time by up to a factor of 3 [24, 50, 61]. However, especially for CT images, the contours should be thoroughly reviewed by physicians [62]. For multimodal image registration, another application of contour propagation is the fusion of information from different image modalities, e.g. between PET, MR, and CT.
For an application in contour propagation, visual assessment is a good indicator of the quality of the deformation results. In a quantitative validation, the model accuracy has to be assessed by contour-based evaluation metrics. For this kind of application, the deformation accuracy within and outside of the structures is not important, so the other validation metrics can be neglected. Different studies comparing commercially available DIR platforms for different anatomical sites showed that the quality of contour propagation is site-specific. For the HN-region, the majority of the deformation models and algorithms obtained more accurate deformation results than for e.g. thorax and pelvis [59, 63]. Moreover, contour propagation was shown to be more accurate for large structures than for smaller structures [41, 49, 59].

Dose Mapping and Dose Accumulation

In the process of ART, the patient anatomy is imaged during each treatment session. The DVFs between the planning CT and the fraction CTs are required for the assessment of the dose-of-the-day as well as for dose accumulation. The forward DVFs are required for the assessment of the dose-of-the-day. This dose can be either calculated based on the anatomy of the day, or by warping the dose distribution of the planning CT based on the DVF. Computing the dose-of-the-day based on the fraction CTs is often problematic since they usually are of lower quality than the planning CT, showing more artifacts, reduced contrast and a limited field of view [64, 65]. Therefore, the forward DVF is required to either generate a synthetic fraction CT [64] for dose calculation or by directly warping the dose. The backward DVFs are required for dose accumulation, i.e. for remapping the dose-of-the-day back to the planning CT [66], where the doses of all fractions are accumulated.
For the application of deformation models in dose mapping and accumulation, a more comprehensive model evaluation than for contour propagation is required. Visual evaluation is useful only to rule out extreme errors in the DVF. However, this does not allow for the validation of the physical plausibility and accuracy of DVFs, which is important for the process of dose accumulation. When comparing different DIR methods, Nobnop et al. [52] showed that the method resulting in the best alignment of contours, correlated with the best dose accumulation. However, other studies have shown that an evaluation based only on the performance of contour transfor-

mation does not guarantee accuracy in dose warping [41, 67]. Rigaud et al. [68] also state that instead of contour-based evaluation criteria, a local point-to-point matching is required. Tilly et al. [69] modeled the influence of DIR uncertainties on dose distributions and found that the mean absolute error has to be less than 2 mm to obtain an uncertainty of less than 3% for the dose in the target volume (D_{95}). Larger margins were shown to relax the uncertainty requirements to the deformation models, but at the cost of higher doses to OARs. DVF consistency errors have been shown to correlate with the accuracy of dose accumulation, the lower the consistency errors, the more accurate the according dose accumulation is [70]. Moreover, the Jacobian determinant has to be larger than 0 to rule out the occurrence of grid folding, at least in relevant anatomical regions [69].
The overall effect of DVF uncertainties on dose warping and dose accumulation depends not only on the magnitude of the uncertainties, but to a large extent on the spatial location of DVF errors and dose gradients[71, 72]. Veiga et al. [66] also showed, that models with similar overall geometric accuracy, had different impact on warped dose, especially in regions of poor image quality and high dose gradients. Pukala et al. [73] further found, that the correlation of landmark errors and dose errors not only depends on the magnitude of the landmark residuals, but also on the dose distribution, the slope of dose-gradients and on the distance to critical structures. Therefore, the greatest DVF accuracy is needed in areas of high dose gradients [43]. Saleh et al. [74] propose an a-priori estimation of the needed accuracy by calculating the distance to dose difference. They found that an accuracy of 1mm is required in high dose gradient regions, whereas large errors of up to 20mm can be tolerated in low dose gradient regions.

Computational Phantom Creation

The use of computational phantoms in radiotherapy is explained in detail in Sec. 2.3.2. The role of the deformation model in the process of phantom creation is the deformation of a given patient image A to an artificially deformed image A'. The deformation can either be derived from an image registration [41] or from a forward deformation based on manual deformation input, e.g. in the form of bone displacements [37]. Based on the resulting DVF, the artificially deformed image A' is resampled by suitable methods [75].
For the application of deformation models in phantom creation, the deformation results should in a first step be validated against an anthropomorphic physical phantom. After such a general validation, for each generated phantom visual assessment of the artificially deformed images is an indicator of the quality of the deformation results. Obvious deformation artifacts can be detected in this way. Additionally, the DVF properties should be checked for physical plausibility by DVF regularity indices.

Multimodality Image Matching

In order to combine the information of different imaging modalities, multi-modal image registration is required. This is challenging due to the different intensities in the different images, but also because the patients are positioned differently in different imaging devices, so that possibly extreme deformations can occur. The challenge for this application is to describe also the extreme deformations like an arms-up to an arms-down posture change.
For an application of multimodal image matching, usually only the image information like the location of the tumor is of importance. Therefore visual assessment of the deformation results is a good indicator for the quality the results.

Summary

The missing gold standard for model evaluation slows down the transfer of deformation models to clinical applications [43]. As described in the previous section, specific validation for individual applications and treatment sites are possible. Still, deformation models should be applied carefully, always being aware of the existing uncertainties and their influence on the individual application.

2.4. The Chainmail-Concept

In this section, the concept of the chainmail-models (CM), which were briefly introduced in Sec. 2.2.2, as well as related work are presented in detail. In the CM-concept, a deformable object is divided into a grid of CM-elements, each connected to its nearest neighbors as illustrated in Fig. 6a for a 2D grid. The deformation behavior is based on geometric constraints and approximates the deformation propagation through a real chainmail (Fig. 6b).

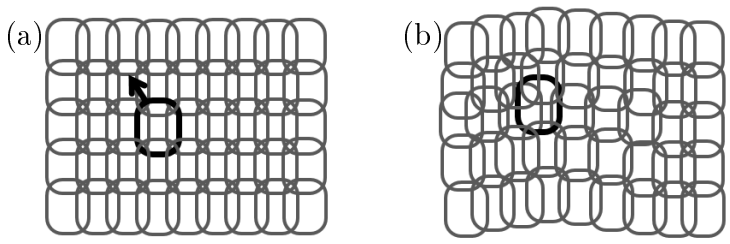

Figure 6.: Illustration of a 2D-grid of connected chainmail elements. (a) The CM-element initiating the deformation is highlighted in black, its displacement is indicated by the black arrow. (b) Illustration of resulting deformed grid.

The geometric constraints restrict the relative displacement between a CM-element P_e and a neighboring CM-element P_n. These constraints define a valid region for P_n with respect to P_e, as illustrated in Fig. 7a. The uniaxial size of the valid region is defined by a minimum (min) and maximum (max) value for the parallel link length, the size of the valid region in perpendicular direction is defined by the shear value ($shear$). For a right neighbor, the valid region is for example defined by:

$$\begin{aligned} x_e + min < x_n &< x_e + max \\ y_e - shear < y_n &< y_e + shear \\ z_e - shear < z_n &< z_e + shear \end{aligned}$$

For the remaining neighbors the valid regions are defined analogically.
A deformation is initialized by displacing an initial CM-element within the CM-grid. Since the valid regions for the neighboring CM-elements are defined relative to the position of this initial CM-element, they are displaced accordingly (Fig. 8b,c). If this displacement is too large, the neighboring elements are outside their valid regions and consequently violate the geometric constraints (Fig. 8c). In a next step, these elements are shifted to a new location inside their displaced valid regions (Fig. 8d). These shifts of the neighbors can then in turn result in constraint violations of further CM-elements, for which the described process is repeated. In this way, the deformation propagates through the CM-grid until all CM-elements meet the geometric

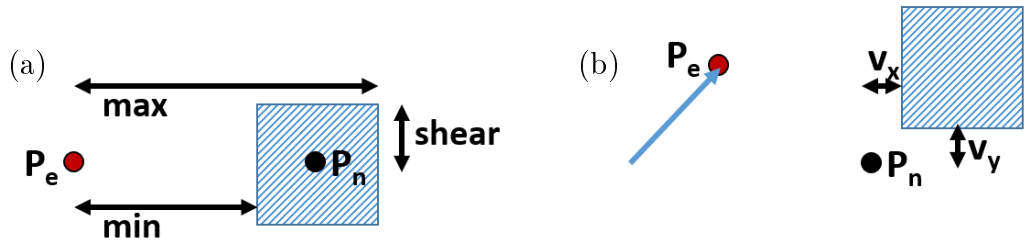

Figure 7.: (a) Illustration of the geometric constraints *min*, *max* and *shear* for a CM-element P_e, relative to its neighboring CM-element P_n. They define the valid region for P_n, as illustrated in blue. (b) Illustration of a displacement of P_e, that results in P_n being outside its valid region. The resulting violations v_x and v_y are indicated.

constraints with respect to their neighbors (Fig. 8e). In this basic chainmail-concept, those CM-elements that are moved first, are also the ones that are processed first.

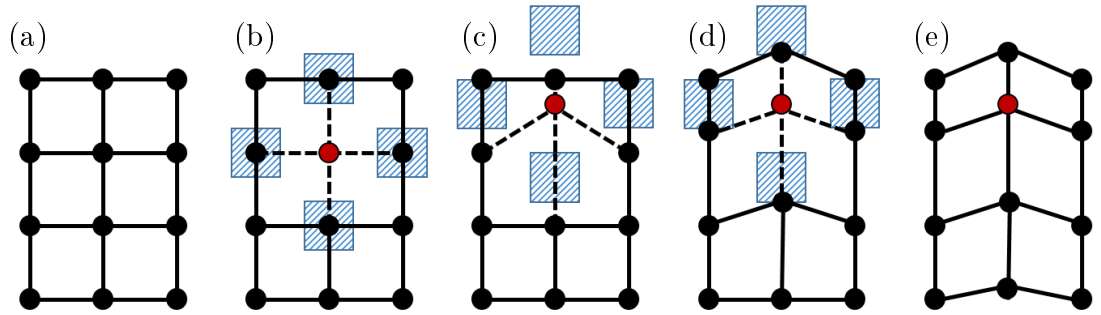

Figure 8.: Illustration of a 2D CM-deformation. (a) Initial CM-grid configuration. (b) Illustration of the initiating CM-element (red) and the valid regions for the nearest neighbors (blue). (c) A displacement of the initiating CM-element also displaces the valid regions. (d) The neighboring CM-elements are shifted to the displaced valid regions in order to fulfill the geometric constraints. (e) Final CM-grid configuration after deformation propagation through the whole CM-grid.

The presented original CM-concept is limited to objects with homogeneous material, in which the geometric constraints are identical for all CM-elements. For objects with heterogeneous material, however, each CM-element would have individual geometric constraints. In order to handle the deformation propagation in a heterogeneous CM-grid, Schill [10] proposed the enhanced chainmail (ECM)-algorithm, in which the processing order of CM-elements is adjusted. He proposes to handle the deformation propagation through heterogeneous material in analogy to the physical process of sound wave propagation as explained in the following paragraph.

Analogy to Sound Wave Propagation

The speed of sound increases with increasing material stiffness, since the coupling between adjacent elements becomes tighter. Schill [2] now assumes that also the propagation of deformation information becomes faster with increasing material stiffness. In the CM-grid, the link stiffness between adjacent CM-elements is determined by the geometric constraints of the individual CM-elements. In case of neighboring CM-elements with different geometric constraints, the two sets of constraints are simply averaged. The stiffer a link between two elements is, the smaller the respective valid region (Fig. 7a) becomes. Therefore, Schill introduces a violation weight $v = |\boldsymbol{v}|$,

which increases with increasing tissue stiffness. For the neighboring CM-element P_n, which is illustrated in Fig. 7b, v_x and v_y are exemplary calculated as:

$$v_x = \begin{cases} |(x_n - x_e) - min| & \text{if } (x_n - x_e) < min \\ 0 & \text{if } min < (x_n - x_e) < max \\ |(x_n - x_e) - max| & \text{if } (x_n - x_e) < max \end{cases} \tag{2.7}$$

$$v_y = \begin{cases} |y_n - y_e| - shear & \text{if } |y_n - y_e| > shear \\ 0 & \text{if } |y_n - y_e| < shear \end{cases}$$

The increasing deformation speed in stiff material is achieved by adjusting the processing order of the CM-elements. For this purpose, Schill introduces a priority queue, in which those CM-elements with the largest violation weight are processed first. In this way, the deformation always transverses the object along the paths of largest constraint violations, i.e. the path of highest tissue stiffness. This especially ensures, that rigid structures maintain their shape and are not torn apart.

Related Work

For heterogeneous tissue, each CM-element has to be assigned individual geometric constraints, which correspond to the tissue stiffness of the underlying deformable materials. For this purpose, the model is set up based on medical images. Material transfer functions mapping the grey values of the images to geometric constraints were introduced for CT [11, 76] as well as for MRI [11].
The original CM is restricted to the topology of Cartesian grids. In this way, a direct correspondence between CM-elements and image-data can be established. However, the deformation results show image artifacts, resulting from the Cartesian configuration. Li and Brodlie [77] extended the CM-concept from Cartesian grids to arbitrary grid configurations, e.g. tetrahedral grids. For this purpose they define the geometric constraints as relative values of the original link lengths.
In order to speed up the CM-algorithm to real-time performance, Roessler [78] designed a parallel version of the CM-algorithm, which was further improved by Rodriguez et al. [11, 79] concerning the computation time for large deformations. With parallel computation, however, the inverse proportional relation between constraint violation (Fig. 7b) and propagation speed cannot be applied any more, since it limits the processing to serial computation. Therefore, Rodriguez et al. [11] further propose a timestamp-based instead of a violation-based processing order of the CM-elements. They define the time that is required to travel through a single element-link inversely proportional to the link stiffness, in order to ensure that the traversal times decrease with increasing tissue stiffness. In this way, the general concept of deformation traveling fastest through stiff tissue is still valid. The timestamps themselves are calculated by summing up the traversal times through all links along the according deformation path. In case that a CM-element is reached by two different paths, the pathway with the shortest time is prioritized, since this corresponds to the pathway along the strongest constraints.
The original CM moreover lacks the ability to handle multiple initial displacements, which are required to model complex deformations. Rodriguez et al. introduce an approach of handling multiple initial information by information prioritization. Following the concept of wavefront propagation, each initiator sends out a deformation wave. If concurrent wavefronts meet in the course of deformation propagation, the deformation pathway with the smallest timestamp is pri-

oritized as explained in the previous paragraph. In this way, multiple initiators can be handled, however a concept for true interaction is still missing.
The deformation propagation by the CM-concept results in a deformed object which, however, not necessarily is in a minimum energy configuration. Therefore, Gibson [80] proposed an elastic relaxation process, during which the relative CM-element positions are locally readjusted in order to reduce the system energy. Rodriguez et al. [11] extended the relaxation concept to the heterogeneous CM.

Summary

The CM-concept approximates the deformation of volumetric objects based on displacements and geometric deformation rules. This approximation is not directly based on phycial laws, but related to biomechanical tissue properties, since the geometric constraints reflect tissue stiffness. Tissue stiffness is very generally defined as the "force needed to achieve a certain deformation of a structure" [81] and varies with the exact description of the applied load configuration and localization. Because of this dependency on load localization, the geometric constraints are defined relative to a particular neighboring CM-element and differ e.g. for the top and the right neighbor, since these represent different directions of loading.
The CM-concept, and therefore also the soft-tissue model developed in this work, can be classified in between those models which require low computation times while not considering the underlying anatomy, and those models, which require large times for model set-up and computation while considering a high level of detail (Fig. 5). As argued above, the deformation rules are not entirely based on the underlying physics, but consider the underlying (physical) material properties. The simplicity of the deformation rules enables low computation times for deformation of data with resolutions up to 1 mm. By code parallelization it es even expected to achieve real-time deformations [11].
Additional advantages of the basic model concept are, that the local topology, represented by the relative positions of neighboring CM-elements, is maintained, so that local physical consistency with regard to topology is achieved. Moreover, the model input can be initiated on voxel-level, so that the model is very flexible concerning the potential input.
Major limitations of the existing CM-concepts are the inability to model inter-element rotation, and the limitation to handling only single initiating CM-elements. Moreover, the final configuration is not in a minimum-energy configuration. The latter is commonly addressed by a subsequent model relaxation, which however will tamper the deformation result, if multiple initiators are introduced. As a last important aspect, the CM does not model volume conservation. There is one approach, aiming at including volume conservation [82], which includes approaches from position-based dynamics, however the concept has not been proven to work for real patient data.

Most of the applications of the CM-concept were developed in the context of surgical simulations and aim at describing the realistic appearance of deformed data sets. In radiotherapy, however, different requirements become important, especially the physical plausibility of the final displacement vectorfield (DVF). In the following, the most important aspects limiting a model-application in radiotherapy are addressed in different stages of model development. First, the parameterization of patient data is established. Then the consistency of the local deformation behavior is investigated and improved based on the processing order within the CM-algorithm and on the introduction of rotational degrees of freedom. Most of the existing CM-approaches only describe local deformations, with one or a few CM-elements initiating the deformation. However, in radiotherapy multiple input structures are required in order to address the global

complexity of the human anatomy. With regard to this, the locality of the model is transferred to a global scale by considering multiple simultaneous initiators and deformation initialization with arbitrarily shaped structures.

3. Purpose

The goal of this work is to develop a heterogeneous, multi-range soft-tissue deformation model which describes biomechanical tissue deformation on voxel-level. It has to achieve low computation times and a high physical and anatomical plausibility, to be suited for adaptive radiotherapy applications. Most state-of-the-art image-based deformation models do achieve low computation times but do not consider the actual anatomy of the underlying images. They require deformation input in the form of anatomical landmarks, which can only be obtained in regions with high image contrast. Therefore, the overall deformations match the appearance of images but the final displacement vectorfield (DVF) reflects unrealistic results like bones being distorted. Most state-of-the-art physically-based models do produce deformation results of high biofidelity, since they consider high levels of detail of the underlying anatomy. However, the improved deformation behavior comes at the cost of increased computation times, which are often not feasible for clinical applications. In addition to high computation times for the deformation also the model set-up is usually time consuming. Moreover, most biomechanical models are tailored to a specific anatomical site and deformation range.

To compromise the described advantages and limitations of the image-based and biomechanical models, the developed soft-tissue deformation model is based on the chainmail (CM)-concept (Sec. 2.4). This concept is faster than most physically-based models but still offers a more detailed description of the underlying anatomy than image-based models. In the context of radiotherapy applications, two major advantages of the CM-concept are the capability to consider heterogeneous soft tissue [2] and the corresponding model parameterization by material-transfer functions [11, 76]. The latter allows for a fast model set-up, rendering tedious delineations as required e.g. for finite element modeling, redundant. Moreover, the CM-approach models deformations on voxel-level, which is of advantage for applications in dose accumulation. Even for deformation on voxel-level, low runtimes in the order of minutes are achieved, with the potential to realize real-time deformations by code parallelization [11]. For clinical applications in adaptive radiotherapy, such low computation times are indispensable.
Most of the existing applications of the CM-concept were developed in the context of surgical simulations and aim at describing the realistic appearance of deformed data sets. In radiotherapy, however, additional requirements become relevant. The most important requirement is the physical and anatomical plausibility of the final DVF.
In the complex human anatomy, rotations make up an important part of the appearing deformations and therefore have to be considered for the description of physiological deformations. In the currently existing CM-concepts, however, a handling of rotational degrees of freedom is missing. Moreover, the modeling of anatomical deformations requires multiple deformation input in different regions of the patient. In most applications of the CM-concept, deformations are initiated by single control points. One approach for handling multiple input information was proposed by Rodriguez et al. [11]. However, even in this approach no information exchange between different initiators is considered. For obtaining a regular deformation grid, the introduction of such an information exchange is required. Additionally, not only the number of initiators, but also their shape, becomes relevant. In human anatomies, the deformations of whole structures like organs, bones or muscles have to be used as model input. However, even those CM-applications in which multiple input information is considered, use only point initiators. For applications in radiotherapy, a concept for handling initiators with complex geometrical shapes is required.

In this work, a new soft-tissue deformation model is constructed, based on the CM-concept. The deformation behavior is tailored to consider the tissue properties of the underlying anatomy instead of only the underlying image intensities. The described limitations of the CM-concept will be solved to achieve deformation results of high biofidelity, as are required for applications in adaptive radiotherapy.

4. Material and Methods

4.1. Patient Data

For the evaluation of the soft-tissue deformation model, two exemplary data sets of HN-patients are used. The first data set depicts a small-range deformation typical for interfractional deformations (patient 1), the second data set depicts a large-range deformation as occurs between a pre-treatment (planning) and post-treatment CT (patient 2).

Patient 1 The image data for patient 1 illustrate a typical small-range interfractional deformation for a HN-patient. They comprise a planning CT and a fraction CT, both with a resolution of 0.98 x 0.98 x 3 mm^3. The planning CT extends from the 6th thoracic vertebra up to the cranial end of the skull and comprises a total number of 512 x 512 x 126 voxels. The fraction CT has a smaller field of view, ranging from the 5th thoracic vertebra to the mid of the skull. The images are taken from a retrospective HN-study [83].
For image analysis, the two images are pre-registered based on the stereotactic frame with which patients are fixated. In both images, all visible bones are manually delineated (42 in total). Figure 9 illustrates the anatomy of the HN-patient based on exemplary slices of the planning CT (upper row). The extent of the deformation range is illustrated by a fusion view of the planning CT and the fraction CT (lower row).

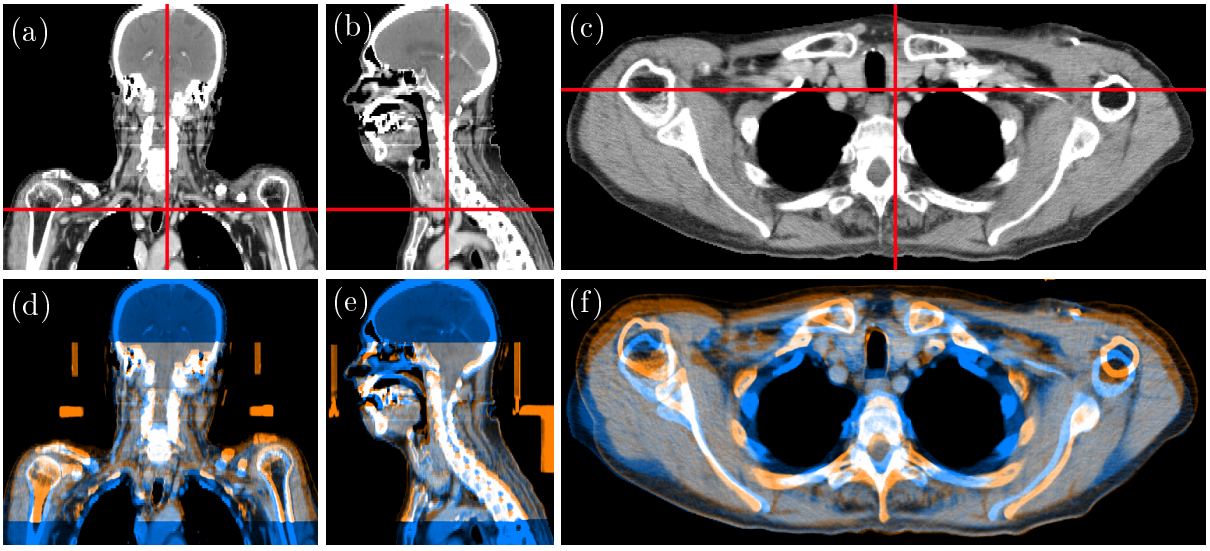

Figure 9.: Exemplary slices of the planning CT (upper row) and a color fusion (lower row) of the planning CT (blue) with the fraction CT (orange) for patient 1. Illustrated are a frontal slice (first column), a sagittal slice (second column) and a transversal slice (third column). The red lines indicate the locations of the respective other two slices.

Patient 2 The image data for patient 2 illustrate a large-range deformation from an arms-up to an arms-down position for a HN-patient. They comprise a pre-treatment (planning) CT and a post-treatment CT, both with a resolution of 1.37 x 1.37 x 3.75 mm^3. The pre-treatment CT is cropped to the field-of-view of the post-treatment CT, which ranges from the 6th thoracic vertebra to the middle of the skull. Both images comprise a total number of 512 x 512 x 80

voxels. The images are taken from 'The Cancer Imaging Archive' [84], Head-Neck Cetuximab collection [85].
The images were already pre-registered, an additional rigid registration focusing on the alignment of the scapulae was executed. In both images, all visible bones are manually delineated (32 in total). Figure 10 illustrates the anatomy of the patient based on exemplary slices of the planning CT (upper row). The fusion view of the pre-treatment and the post-treatment CT, further illustrates the covered deformation range (lower row).

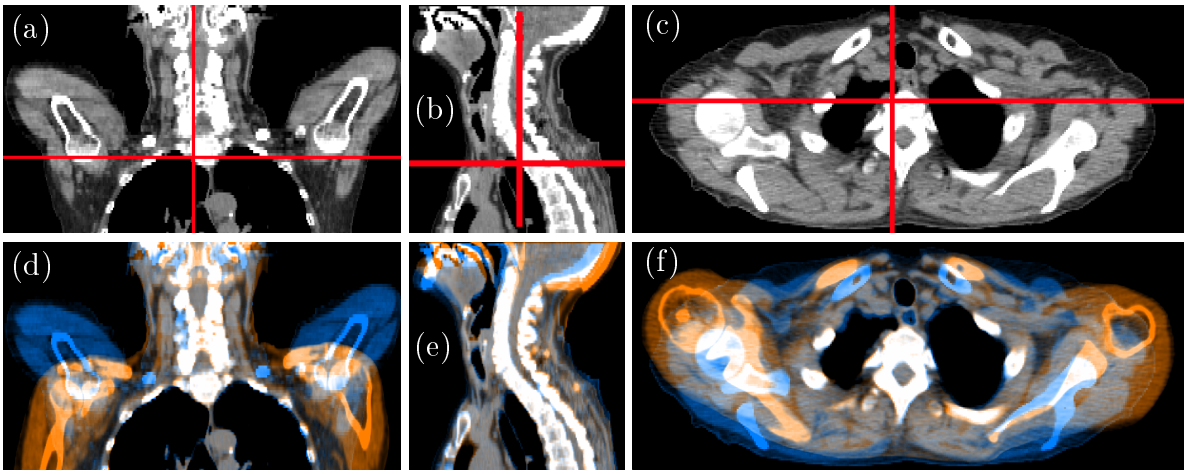

Figure 10.: Exemplary slices of the planning CT (upper row) and a color fusion (lower row) of the planning CT (blue) with the fraction CT (orange) for patient 2. Illustrated are a frontal slice (first column), a sagittal slice (second column) and a transversal slice (third column). The red lines indicate the locations of the respective other two slices.

4.2. Transformation Modeling

4.2.1. Kinematic HN-Skeleton Model

The input for the investigated soft-tissue transformations is generated by a kinematic HN-model for the skeleton. This model connects rigid bones by physiological joints and thereby allows for biomechanically reasonable motion. For the extraction of the kinematic model from patient images, the delineations of all bones are required. Joint positioning is executed automatically. The displacement of the bones is modeled by kinematic laws, which propagate the motion through the whole skeleton [3, 4]. The output of this model are the translation and rotation parameter for each individual bone.
For forward deformation modeling, mimicking artificially created skeletal postures, the skeleton is manually manipulated. The manually enforced transformations are propagated through the whole skeleton by the kinematic model [3], resulting in the required transformation parameters for each bone. For image registration of the bones, the kinematic model is coupled to an optimizer for fitting the transformation parameters to the underlying images [4].

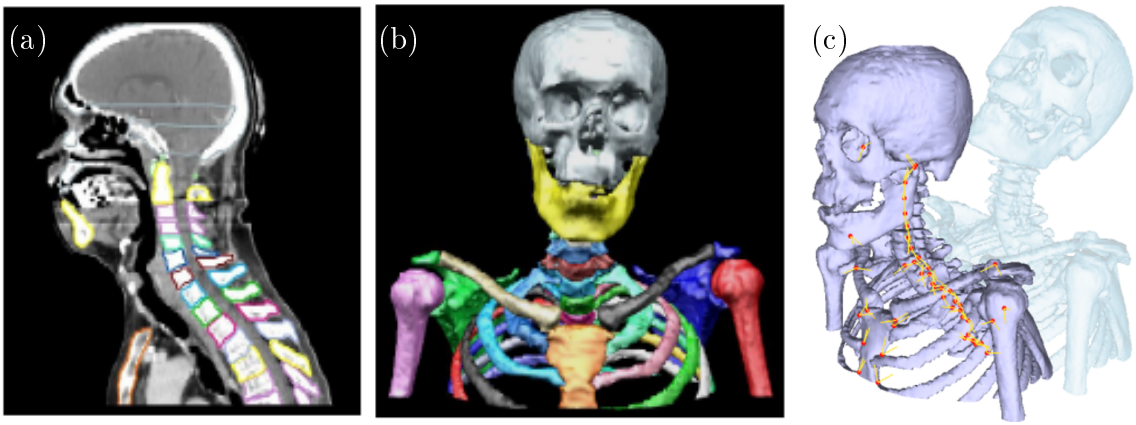

Figure 11.: Illustration of the creation of the HN-skeleton model. The bone contours from the planning CT (a) are used to build up the skeleton model (b). This model can be articulated according to kinematic deformation rules (c).

4.2.2. Chainmail-Model

The chainmail (CM)-concept (Sec. 2.4), originally proposed by Gibson [1] and extended to heterogeneous tissue deformation by Schill et al. [10], is the basis for the developed soft-tissue deformation model. The CM-grid is set up based on the patient CT images, with each image voxel corresponding to a chainmail-element in the chainmail-grid. CM-elements corresponding to HU-values <-500 were excluded from the transformations.
The deformations are initialized by assigning an initial displacement to each CM-element that corresponds to a voxel in a bone. For identification of the individual bones, bone segmentations are used. The actual displacement vectors are derived from the output of the kinematic model, which provides the translation and rotation for each bone.

4.2.3. Thin-Plate Splines

An inhouse implementation of a thin-plate splines model (Sec. 2.2.1) is used for comparison against the deformation behavior of the developed soft-tissue model for patient 1. For the model input, on each bone 5-6 evenly distributed control points are defined on the bone surfaces. Similarly as for the soft-tissue model, the target positions of the control points are derived from the output of the kinematic model, which provides translation and rotation parameters.

4.2.4. ANACONDA-Algorithm

The ANACONDA-algorithm [86] as implemented into the commercial RayStation planning system is used for comparison against the developed model for the data set of patient 2. For model input, the image information from the pre- and post-treatment CT of patient 2, as well as the contours of the skull and both humeri and scapulae are used. The ANACONDA-algorithm is not a pure transformation model, but a registration algorithm. In the optimization process, an objective function considering image similarity, grid regularity and the shapes of the controlling structures is minimized. The resulting DVFs were not available for export, so only an image-based evaluation could be executed.

4.2.5. Image Sampling

The deformation models generate voxel-wise displacement vectorfields. The vectorfields, however, do usually not map voxel mid-points to voxel midpoints. To visualize the resulting deformed patient anatomy, therefore, an interpolation methods that resamples the deformation information on a regular target grid is required. For this purpose, the parallel resampling method proposed by Rodriguez et al. [75] is implemented on the GPU via CUDA API [3].
This resampling approach is based on an implicit sampling mesh. Each voxel of the original CT image is associated with a vertex of the sampling mesh in which the respective HU-values are stored. Eight adjacent vertices define a hexahedron, which is further decomposed into five tetrahedrons as illustrated in Fig. 12. In this way, a continuous and complete sampling mesh is generated. Assuming that no grid folding occurs, it is guaranteed that each grid point in the target grid can be assigned to exactly one of the tetrahedrons. The HU-values for the artificially deformed image are obtained by barycentric interpolation between the HU-values stored in the vertices of the respective tetrahedrons. In case of grid folding, the assignment of grid points to tetrahedrons is not unique, so for DVFs with large areas of grid folding, the resampling method fails.

4.3. Evaluation Methods

4.3.1. Visual Evaluation

All deformation results are visually inspected for obvious DVF irregularities or image artifacts. Moreover, the application of color fusions is used for comparing artificially deformed images against actual target images.

4.3.2. The Jacobian Determinant

For evaluating the DVF regularity of modeled deformations, the Jacobian determinant (Sec. 2.3.2), in the following simply termed as 'Jacobian', is used. For continuous deformation functions T it is defined by the partial derivatives of T at voxel positions $\boldsymbol{r}$. However, the deformation models applied in this work provide discrete DVFs. Therefore, the Jacobian is explicitly calculated by the relative volume change of each voxel [87]:

$$J = |J(\boldsymbol{T}(\boldsymbol{r}))| = \left| \left(\frac{\partial T_i}{\partial x_j}(\boldsymbol{r}) \right)_{i=1,2,3;j=1,2,3} \right| = \frac{V_{initial}}{V_{deformed}}(\boldsymbol{r}). \tag{4.1}$$

A Jacobian of $J = 1$ indicates a volume conserving deformation, a Jacobian of $J > 1$ indicates volume growth and a Jacobian $J \in [0, 1[$ indicates volume shrinkage. Jacobians $J < 0$ indicate grid folding.
The volume of a voxel is defined by the eight adjoining grid-points. For mapping the volumes to grid-points, each voxel volume is assigned to the grid point with the lowest grid indices as illustrated in Fig. 12a. For the actual volume calculation, each voxel is split into 5 tetrahedrons as proposed by Rodriguez et al. [75] (Fig. 12b). This is necessary since a simple triple product can yield wrong results for deformed voxels. The volume of each tetrahedron is calculated by a simple triple product, for which the orientations are chosen in a way that topology changes result

in negative triple products. If any of the 5 tetrahedrons yields a negative volume, the whole voxel is assigned a Jacobian of -1, i.e. the extent of grid folding is not explicitly calculated.

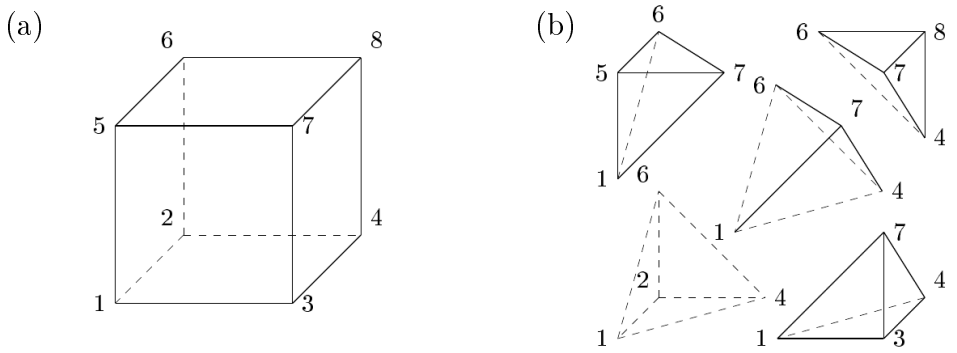

Figure 12.: (a) Illustration of the definition of a voxel volume. The grid point to which the illustrated volume is assigned is grid point 1. (b) Illustration of the used tetrahedral voxel decomposition [75].

For a global analysis of grid regularity, the Jacobian distribution is analyzed for the whole image. Voxels with an $HU < -500$, which are not considered during the deformation process, are excluded from the analysis. For a better comparison of different Jacobian distributions, five characteristic values are defined, which are summarized in Tab. 2. The overall percentage of voxels with a negative Jacobian are depicted by $J_{<0}$. The remaining positive values of the Jacobian distribution are further described, by the percentage of voxels showing extreme volume changes, i.e. which more than double their volume ($J_{>2}$) or shrink to less than half of their original volume ($J_{<0.5}$). The overall volume change of the patient is represented by $J_{\varnothing}$. And finally, the maximum Jacobian of the distribution, J_{max}, indicates how far the tail of the distribution extends. Moreover, Jacobian maps which depict the Jacobian values in the anatomical context are used for further evaluation of the biofidelity of the deformation results.

$J_{<0}$	Percentage of voxels showing grid folding
$J_{>2}$	Percentage of voxels with a relative volume growth of more than 2
$J_{<0.5}$	Percentage of voxels with a relative volume shrinkage of less than 0.5
$J_{\varnothing}$	Average Jacobian value
J_{max}	Maximum Jacobian value of the distribution

Table 2.: Definition of characteristic values for a Jacobian distribution. The value $J_{<0}$ is defined relative to the overall Jacobian distribution, all other values are defined relative to the positive part of the Jacobian distribution.

For illustrating the Jacobians in the context of the underlying anatomy, Jacobian maps are introduced. These are similar to the maps used by Schreibmann et al. [54] for illustration of the vector curl. The maps represent the same data structure as the original patient CT image, with the grey values being replaced by a color-map, visualizing the Jacobian values for each voxel. Red values represent Jacobians $J > 1$, blue values represent Jacobians $J \in [0, 1[$ and white values represent a Jacobian of $J = 1$. Areas with a negative Jacobian $J < 0$ which indicates grid folding are colored in black (compare e.g. Fig. 28b).

4.3.3. Landmark Errors

For estimating the accuracy of the modeled soft-tissue deformations, landmark evaluation is used (Sec. 2.3.2). For patient 1, a set of 16 soft-tissue landmarks is manually defined in the planning CT ($\boldsymbol{x}_{planning}$), as well as in the fraction CT ($\boldsymbol{x}_{fraction}$), based on anatomical features like vessel calcification or vessel bifurcations. Due to the limited occurrence of such features, the landmarks are not regularly distributed. For patient 2, the definition of such landmarks was not possible at all, due to the extremely large deformation range.
The landmark positions in the artificially deformed anatomy($\boldsymbol{x}_{deformed}$) are calculated from the respective DVFs. The mean relative landmark error $\bar{\Delta}$ is calculated according to:

$$\bar{\Delta} = \frac{1}{|\boldsymbol{\Delta}_{orig}|} \cdot \left(\frac{1}{16} \cdot \sum_{i=1}^{16} |\boldsymbol{\Delta}_{model}| \right). \tag{4.2}$$

with $\boldsymbol{\Delta}_{orig} = \boldsymbol{x}_{planning} - \boldsymbol{x}_{fraction}$ and $\boldsymbol{\Delta}_{model} = \boldsymbol{x}_{deformed} - \boldsymbol{x}_{fraction}$. The mean standard deviation $\sigma_{\bar{\Delta}}$ is calculated according to:

$$\sigma_{\bar{\Delta}} = \sqrt{\frac{\sum_{i=1}^{16} \left(|\frac{\boldsymbol{\Delta}_{model}}{\boldsymbol{\Delta}_{orig}}| - \bar{\Delta} \right)^2}{15}}. \tag{4.3}$$

4.4. Software Toolkit

The functionalities to load and visualize patient data, as well as the methods for contour delineation, were provided by the in-house developed radiotherapy planning system 'Virtual radiotherapy simulation' (VIRTUOS) [88]. This system also provides the used implementation of the Thin-Plate-Splines deformation algorithm (Sec. 4.2.3).

5. Conceptual Model Development

The concept of the chainmail approach (CM), which is explained in detail in Sec. 2.4, is used for the development of a soft-tissue deformation model. Different material transfer functions, mapping the values of the hounsfield units (HUs) of CT scans to elasticity, are introduced to model the deformation of CTs. Further, three new aspects, relevant for radiotherapy applications are included into the CM-concept. First, two new approaches for how to consider rotational degrees of freedom in the CM-concept are developed. Second, a new concept for how to handle multiple deformation initiators is introduced, and third, instead of single point initiators, more complex deformation input is considered. In the following, the different stages of model development are described in detail and discussed concerning their influence on the deformation behavior.

5.1. Parameterization

For modeling CT images, the CM-grid (Fig. 8a) is set up in a way that each CM-element corresponds to a voxel in the CT scan. A material transfer function is defined which maps the HU-values of a patient CT to the geometric constraints of the according CM-elements. The geometric constraints are defined relative to the original link lengths in the CM-grid. The material transfer function is piecewise-defined, covering three different tissue categories as illustrated in Fig. 13. For rigid material like bones, the original link lengths are fixed ($min = max = 1$, $shear = 0$). For totally elastic material as assumed for air, the links are allowed to be expanded by up to a factor of 2 ($max = 2$), totally compressed ($min = 0$), and to shear against each other by one link length ($shear = 1$). For the third category, which covers all deformable soft tissues, the constraint values are linearly interpolated between the values of the other two categories. For this category, two different elasticity levels are distinguished. A stiff parameter set restricts the soft tissue to deform like very stiff tissue and an elastic parameter set describes very elastic tissue deformations. Both are illustrated in Fig. 13. In the following, all references to the geometric constraints refer to the constraints for a particular link in the CM-grid. These constraints are obtained by summing up the relative constraint values of two adjoining CM-elements and by multiplication with the original link length.

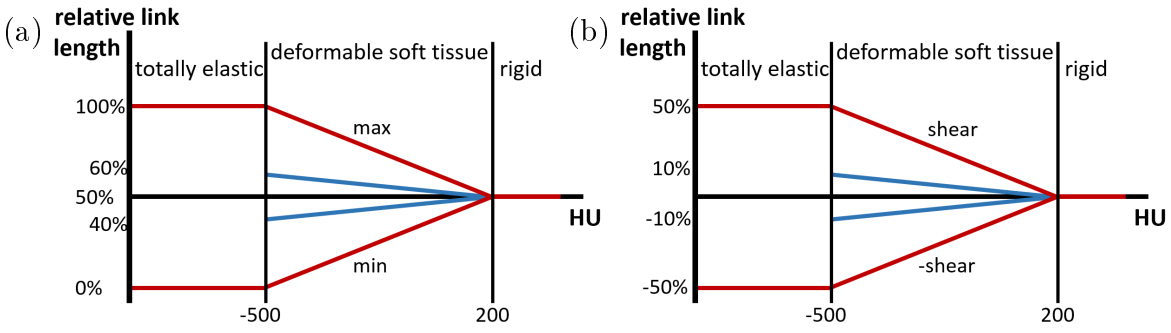

Figure 13.: Illustration of the introduced material transfer functions for (a) the compression and expansion constraints and (b) shear constraints. For the totally elastic regime, as well as for the rigid regime, the functions are identical for both parameter sets. For the regime of deformable soft tissue, the stiff parameter set is indicated in blue.

In the remaining part of this chapter, the elastic parameter set is used, since it allows larger

deformations and therefore a better exploration of general deformation effects. However, the patient deformations in radiotherapy are expected to be less elastic, which is why both parameter sets will be investigated in the next chapter.

5.2. Processing Order

As elaborated in detail by Schill et al. [10], the processing order of CM-elements within the CM-algorithm is highly relevant for deformation of heterogeneous tissue. The processing order is defined by the sorting criterion of the priority queue, which is introduced in the enhanced chainmail concept (Sec. 2.4). In the following, the two different sorting criteria are investigated for deformation propagation in heterogeneous tissue.

5.2.1. Constraint Violation

The violation weight was defined by Schill et al. [10] as an indicator for how strong the geometric constraints are violated by the displacement of neighboring CM-elements (Fig. 7b). It is assumed to increase with increasing tissue stiffness and is calculated according to Eq. 2.7.

5.2.2. Timestamps

The timestamps were defined by Rodriguez et al. [11] as a measure for the time a deformation takes to travel through the links between neighboring CM-elements. This time is assumed to decrease with increasing tissue stiffness. During deformation propagation, the traversal times for all links along a deformation path are accumulated and stored in an element-specific timestamp. Therefore, also the timestamp depends on the stiffness of the material along the propagation path. When a CM-element that was already reached by a certain deformation path is reached again, the timestamp-marks for the two paths are compared and the fastest deformation is imposed over the other one.
According to the proposition of Rodriguez et al., the time for deformation propagation from one element to the next is derived from the geometric constraints. For the soft-tissue deformation model it is defined as the inverse of the geometrical shear constraint: $t = \frac{1}{shear}$.

5.2.3. Deformation Results

The influence of the sorting criterion on the deformation results is illustrated based on a translation in y-direction, which is initiated within a homogeneous soft-tissue object with an embedded rigid structure (Fig. 14a). The resulting processing order is illustrated based on heatmaps of the processing indices (Fig. 14b and c). For both sorting criteria the deformation is uniformly propagated outwards, until the rigid structure is reached. The shape of the deformation propagation in the homogeneous soft tissue is rhombus-like. When the rigid structure is reached, all CM-elements belonging to this rigid structure are processed first, before the deformation is further propagated into the surrounding soft-tissue. For the further deformation propagation, the heatmap for the sorting based on constraint violation shows irregularities in proximity to the rigid structure, whereas for the sorting based on timestamps a regular wavelike propagation is observed.

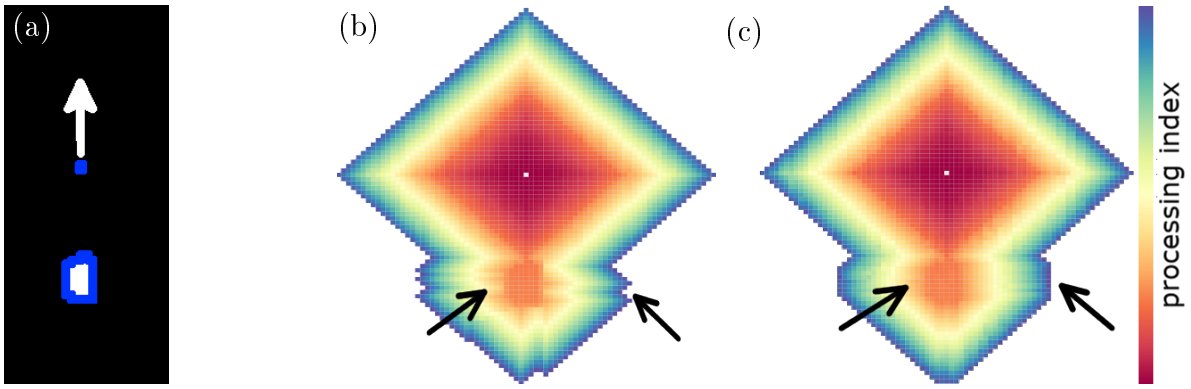

Figure 14.: Propagation of a translation in y-direction in heterogeneous tissue. (a) Initial tissue structure: Homogeneous soft tissue (black) with an embedded rigid structure (white, contoured in blue). The position of the initiating CM-element is indicated by the blue dot, the deformation direction by the white arrow. (b) Heatmap of the processing indices for a processing based on constraint violation. Exemplary irregularities are marked by the arrows. (c) Heatmap for processing based on timestamps. The resolved irregularities are marked by the arrows.

Figure 15a illustrates the deformation grid resulting for the sorting based on constraint-violation. It depicts the same rhombus-like deformation behavior, which was observed in the heatmaps. This results from the cartesian topology of the CM-grid and from the decoupling of deformation propagation into x,y and z-direction. Figures 15b and c further illustrate the grid-irregularities occurring for a sorting based on the constraint-violation and the regular deformation grid for the sorting based on timestamps. In the following, only the superior timestamp-based deformation propagation will be considered.

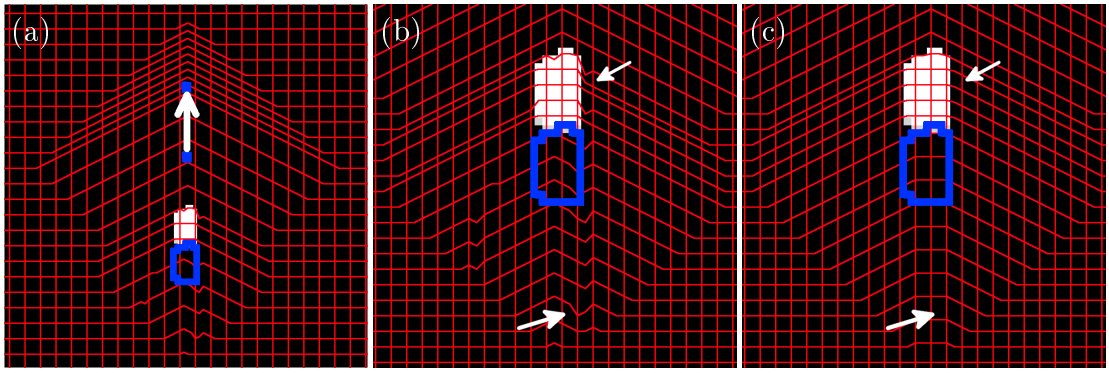

Figure 15.: (a) Deformation grid resulting from a propagation based on constraint-violation for the deformation illustrated in Fig. 14a, overlaid on the deformed anatomy. The blue contour indicates the original position of the rigid structure. (b) Close-up of the deformation grid resulting from constraint-based propagation. Exemplary grid irregularities are marked by the arrows. (c) Close-up for the deformation grid resulting from timestamp-based propagation. The resolved grid irregularities are marked by the arrows.

5.3. Rotational Degrees of Freedom

The existing CM-approaches are missing a concept to handle inter-element orientation. To solve this problem, two new approaches to introduce the orientation of CM-elements into the overall CM-concept are developed. The orientation of a CM-element is represented by a rotation angle, with respect to a fixed rotation axis. These two parameters are depicted by means of a quaternion q (App. A.1). It is important to note that rotating a CM-element around a given rotation point and axis always induces a change in position. The extent of positional change depends on the rotation angle as well as on the distance to the rotation point. Regardless of how the rotation angle is calculated during deformation propagation, it is essential that the according rotated position depicts the correct positional change.

5.3.1. Constraint-Based Approach

For each CM-element an individual coordinate system, with the orientation defined by a quaternion q is introduced. When propagating the rotation of a CM-element P_e, the valid region for the neighboring element P_n co-rotates (Fig. 16a,b). The position of P_n being shifted into the valid region is $\boldsymbol{p}_n^{rot}$ and is used to calculate the propagated rotation angle α_n, with respect to the given rotation plane (Fig. 16c):

$$\alpha_n = \alpha \left[\text{proj}(\boldsymbol{p}_n^{rot}) - \boldsymbol{r},\ \text{proj}(\boldsymbol{p}_n) - \boldsymbol{r} \right]. \tag{5.1}$$

The projections of the respective positions into the rotation plane are termed as $\text{proj}(\boldsymbol{p}_n^{rot})$ and $\text{proj}(\boldsymbol{p}_n)$ and the position of the rotation point is $\boldsymbol{r}$. An exception occurs, if the rotation axis is identical to one of the cardinal axes in the CM-grid. In this case the new angle is calculated as $\alpha_n = \alpha_e - \arctan\left(\frac{shear}{min}\right)$. However, following this procedure the distance $d(\text{proj}(\boldsymbol{p}_n^{rot}) - \boldsymbol{r})$ is not necessarily equal to the distance $d(\text{proj}(\boldsymbol{p}_n) - \boldsymbol{r})$, as illustrated in Fig. 16d. Therefore, the artificial, rotated-only position $\boldsymbol{p}_n^{rot*}$ is introduced, which is obtained by rotating $\boldsymbol{p}_n$ by the calculated rotation angle α_n around the rotation axis. The angle and axis define the quaternion q_n:

$$\boldsymbol{p}_n^{rot*} = \boldsymbol{r} + q_n \cdot (\boldsymbol{p}_n - \boldsymbol{r}) \cdot q_n^{-1}. \tag{5.2}$$

In the course of propagation, the position $\boldsymbol{p}_n^{rot*}$ is used for calculation of propagated rotation angles, whereas the position $\boldsymbol{p}_n^{rot}$ is used for calculation of the propagated final positions of the CM-elements.
When combining a rotation with a translational movement, no adaption of the described rotation handling is required. The overall target position is determined independently from the artificial rotated position, by shifting the original CM-element position into the co-translated and co-rotated valid region.

5.3.2. Linear-Decay Approach

In the linear-decay approach the orientation of each CM-element is also defined by a quaternion representing the rotation angle and axis. The angle propagation from a CM-element P_e to a neighboring CM-element P_n is calculated from a linear decay function, which is defined as:

$$\alpha_n = \alpha_e - \frac{\alpha_0}{\lambda}, \tag{5.3}$$

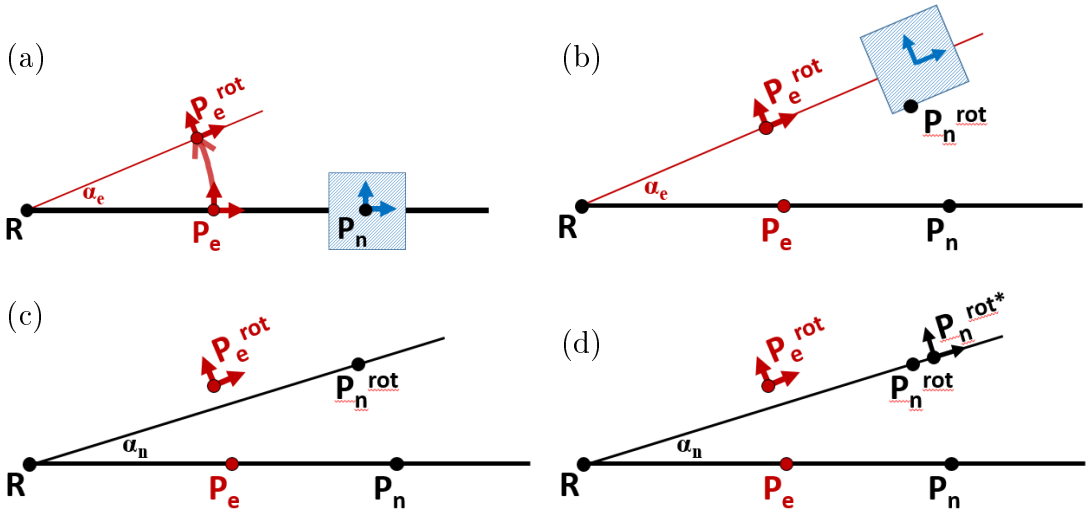

Figure 16.: Illustration of a 2D rotation propagation according to the constraint-based approach. (a) Original position of the rotation point R, element P_e, its neighboring element P_n and the respective valid region. (b) Initial rotation of P_e, co-rotation of the valid region and adjusted position P_n^{rot}. (c) Definition of the propagated angle α_n. (d) Definition of the artificial rotated position $P_n^{rot\,*}$.

with α_0 being the rotation angle of the initiating CM-element, α_e the rotation angle of CM-element P_e and λ the decay constant. An initial rotation displacement Δ^{rot} is expected to decay over the same number of elements as an equivalent initial translation. Therefore, the decay constant λ is defined as the maximum number of CM-elements, through which the deformation has to propagate, until the initial displacement vector $\boldsymbol{\Delta}^{rot}$ is completely decayed. It is assumed that the initial displacement is reduced by either the shear constraint or the difference between the original link length l_{orig} and the compression/extension constraints in each CM-element along the propagation path:

$$\lambda = \max\left(\frac{\Delta_i^{rot}}{l_{orig} - min}, \frac{\Delta_i^{rot}}{shear},\right), \quad i = x, y, z. \tag{5.4}$$

The initial displacement vector is defined as $\boldsymbol{\Delta}^{rot} = \alpha_0 \cdot d(\boldsymbol{r}, \mathrm{proj}(\boldsymbol{p}_n)) \cdot \frac{\boldsymbol{u}}{u}$. Its length is equal to the arc length of the rotation. Its direction $\boldsymbol{u}$ lies in the rotation plane and is a tangent to the rotation curve. Especially for large rotation angles, it is very important that $\boldsymbol{\Delta}^{rot}$ is defined tangential to the rotation curve and reflects the actual positional displacement. If it was approximated as the connecting vector between the original and final position, which would be the according chord, the decay constant would be underestimated and grid folding would occur. This is also the reason why λ has to be defined as the maximum over all directions. The following example for a 2D-rotation of the initial CM-element P_0 around the z-axis illustrates the dependencies of λ:

$$\begin{aligned} \boldsymbol{p}_0 &= (d, 0),\ \boldsymbol{r} = (0, 0) \\ \boldsymbol{\Delta}^{rot} &= (d \cdot \cos(\alpha_0), d \cdot \sin(\alpha_0)) \\ \lambda(d, \alpha_0) &= d \cdot \max\left(\frac{\cos(\alpha_0)}{l_{orig} - min}, \frac{\cos(\alpha_0)}{shear}, \frac{\sin(\alpha_0)}{l_{orig} - min}, \frac{\sin(\alpha_0)}{shear}\right). \end{aligned} \tag{5.5}$$

The final rotated position P_n^{rot*} is calculated in the same way as the artificial rotated-only position in the constraint-based approach (Eq. 5.2).
When combining a rotation with a translational movement, both are treated separately in the linear-decay approach. First, the initial rotation is propagated as described above, resulting in the rotation angle α_n (quaternion q_n) and in the final rotated position $\boldsymbol{p}_n^{rot*}$. Then the initial translation is propagated in the global coordinate system as suggested in the existing CM-approaches without consideration of rotations, resulting in a translated position $\boldsymbol{p}_n^{trans}$. The overall target position $\boldsymbol{p}_n$ is then calculated as:

$$\boldsymbol{p}_n = \boldsymbol{p}_n^{rot*} + q_n \cdot \boldsymbol{p}_n^{trans} \cdot q_n^{-1}. \tag{5.6}$$

5.3.3. Deformation Results

In both approaches, the propagation of orientation is influenced by the initial rotation angle and by the location of the rotation point as illustrated in Fig. 17 for a 1D-propagation in homogeneous elastic material. The closer the initiating CM-element (tip element of each curve) is located to the rotation point, the steeper the respective overall angle decay function is. The individual decay functions differ between the constraint-based and the linear-decay approach. For the constraint-based approach, the slope increases for propagation in direction of the rotation point and decreases for propagation away from the rotation point. Moreover, for certain distances to the rotation point the decay function shows a kink. The linear-decay approach shows a uniform slope regardless of the direction of propagation and no kinks.

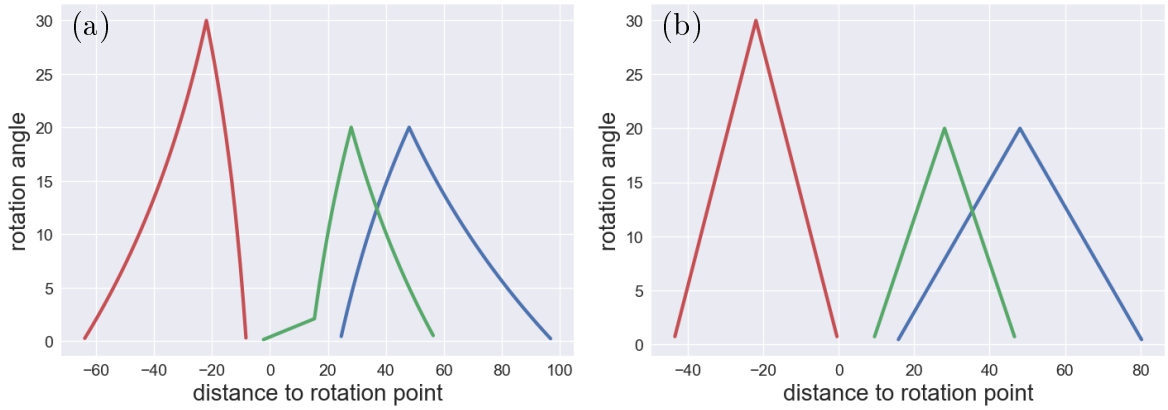

Figure 17.: Illustration of three angle decay functions for different initial rotation angles (tip of the curves) and different distances to the rotation point (location on x-axis). (a) Constraint-based approach. (b) Linear-decay approach.

The shape of the angle decay functions for the constraint based approach results from the fact that for constant rotation angles the absolute positional displacement increases with increasing distance from the rotation point. The geometric constraints which limit the relative positional change between neighboring CM-elements on the other hand remain constant. If a deformation propagation approximates the rotation point, a shift by the constant geometric constraints correspond to a large angle and therefore a fast rotation angle decay. If a deformation propagates away from the rotation point, the constant geometric constraints correspond to small angles, resulting in a decreasing slope of the angle decay function.
For an exemplary 2D-rotation in homogeneous tissue, the resulting deformation grids are illus-

trated in Fig. 18. The figure shows that the constraint-based approach results in a less regular deformation grid than the linear-decay approach. The reason for this is that the valid regions for relative displacements between neighboring CM-elements are defined along the cardinal axes. Therefore, it can happen that constraint violations in one direction (e.g. compression) are totally resolved before those in the other directions (e.g. shear) are. This phenomenon is indicated by the white arrow in Fig. 18a.

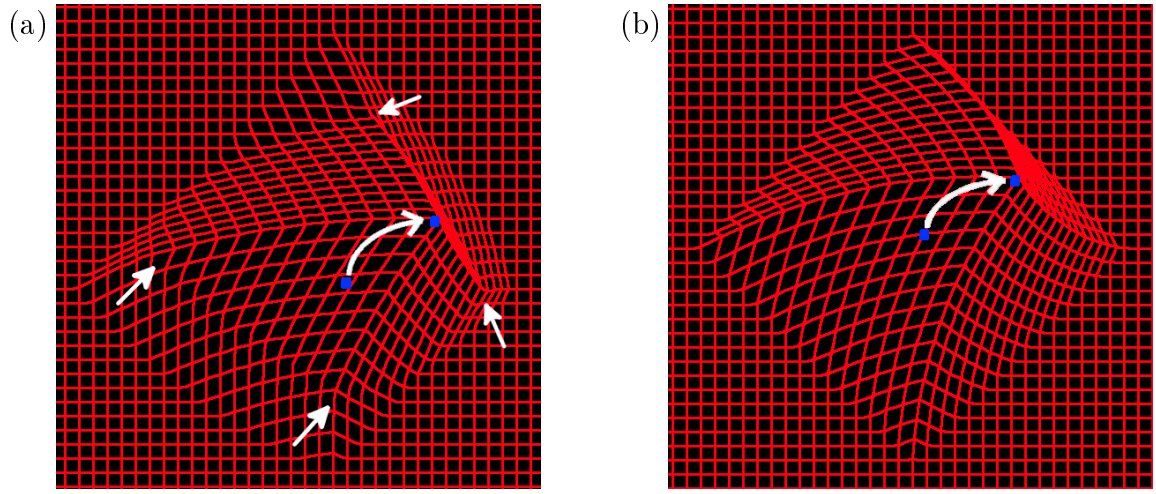

Figure 18.: Illustration of 2D deformation grids for propagation of an initial rotation of 20 deg in homogeneous tissue. The initial and final position of the initiating CM-element are indicated by the blue points, connected by the white curved arrow. (a) Constraint-based approach, grid irregularities are marked by the white arrows. (b) Linear-decay approach. The grid irregularities are resolved.

At such a point, the slope of the angle-decay function changes, resulting in a kink as observed in one of the illustrated decay functions (Fig. 17a). Such a non-uniform angle decay can result in grid folding for disadvantageous positioning of the rotation point and therefore has to be applied with care. The linear-decay approach resolves this problem by explicitly defining a uniform angle decay function. The uniform angle decay results in a deformation grid without the grid irregularities observed for the constraint-based approach.

5.4. Multiple Initiators

The existing CM-approaches are missing sophisticated concepts to handle multiple initiators. While most approaches simply use single initiators, Rodriguez et al. [11] introduced a prioritization approach, in which deformation information is prioritized by timestamps. However, even this approach does not consider an exchange of information between the different initiators. In the following, first the prioritization approach of Rodriguez et al. is presented. Then a new approach is developed in which the interaction of deformation information between the different initiators is considered.

5.4.1. Prioritization

In the prioritization approach, all initiators are assumed to start their deformation at the same time 0. During propagation, the time the deformation takes to reach the surrounding CM-

elements is stored in timestamps (Sec. 5.2.2). If a CM-element is reached by deformation paths originating from different initiators, the information from the initiator with the shortest deformation time is prioritized as proposed by Rodriguez et al. [11]. In this way, each initiator influences a clearly defined area in the deformation grid.

5.4.2. Superposition

In the following, a new approach which allows to consider the interaction of different initial deformations is proposed. The deformation of each initiating structure is separately propagated through the whole CM-grid, neglecting deformation information of the other initiating structures. In this way, the regions of influence of the different initiators increase. The only restriction is that CM-elements located within any other initiating structuremay not be moved. If an initiator initially has zero displacement, or if a deformation has decayed to a zero displacement, this information of no displacement is also propagated. This is important since zero displacements can be interpreted as forces fixating the surrounding tissue. Zero displacements are propagated for timestamps $t < 800$, for larger timestamps the influence on the overall deformation is assumed to be negligible. Moreover, this cut-off limits the computation time.
To consider interaction between the different initiators, the individual deformations are interfered by a weighted superposition. A non-weighted superposition would have the draw-back that bones with large displacement would have a much larger influence or weight than those with small displacements (similar to the problem observed for the sorting by constraint violation, Sec. 5.2.1). To consider also the fixation of tissue, which is represented by zero initial displacements, a weighted superposition is introduced. The weight of the individual deformations is assumed to decrease with increasing distance to the initiator, as well as with increasing tissue stiffness along the deformation path. Therefore, it is assumed to be $\propto \frac{1}{t^n}$, $n \in \mathbb{N}$. The final displacement vector $\boldsymbol{x}_{tot}$ for each CM-element is therefore calculated by a timestamp-based weighting with $\alpha_i = \frac{1}{t_i^n}$ of the individual displacement vectors $\boldsymbol{x}_i$:

$$\boldsymbol{x}_{tot} = \left(\sum_i \alpha_i\right)^{-1} \cdot \left(\sum_i \alpha_i \boldsymbol{x}_i\right). \tag{5.7}$$

For two initiators, separated by the overall deformation time t, the weighting function derived from Eq. 5.7 is the following:

$$w(t_i) = \frac{(t - t_i)^n}{t_i^n + (t - t_i)^n}. \tag{5.8}$$

Figure 19 illustrates this function for exemplary values of n. For $n = 1$ the weighting function shows a simple linear dependency on t_i, with increasing exponent n, the function approximates a step-function, which represents the approach of prioritization.

5.4.3. Deformation Results

Figure 20 illustrates the deformation grids resulting from two exemplary initial deformations, generated by two point initiators. For information prioritization, grid irregularities occur at the boundary between the areas influenced by the two initiators. For the initiators being torn apart (Fig. 20a), the element links at the boundary are overstretched whereas for the initiators being pushed together (Fig. 20b), grid folding occurs. With the new approach of superposition, the

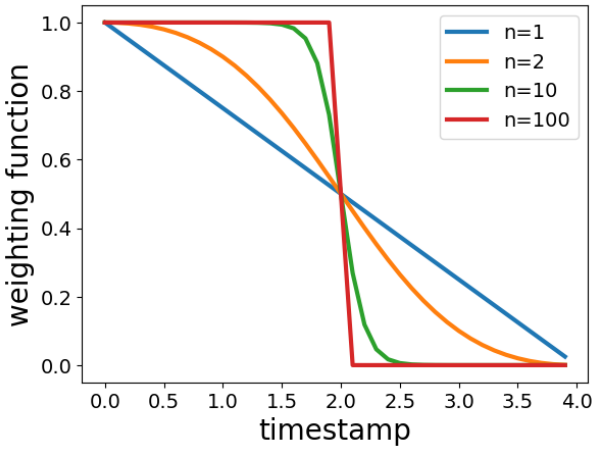

Figure 19.: Exemplary weighting functions for the weighting of local versus global deformation information in the superposition approach. The initiating elements are located at $t = 0$ and at $t = 4$. With increasing exponent n, the local weightings increase, approaching a step-function, which represents the prioritization approach.

folding and respective overstretching are evenly distributed between the two initiators, resulting in more regular deformation grids (Fig. 20c,d).

5.5. Initiating Structures

In the existing CM-approaches the deformations are initiated only by point initiators. However, in complex anatomies also complex geometric shapes are required for deformation initialization. In the following, a new approach to improve the deformation results in the presence of initiating structures is presented.
A rigid initiating structure can be considered as a collection of multiple initiating CM-elements, each carrying the same deformation information. Each CM-element at a structure surface sends out a deformation wave. CM-elements on the same wave-front have equal timestamps. So for a simple processing order based only on timestamps (Sec. 5.2.2), CM-elements on the same wave front are processed in an arbitrary order without exchanging deformation information. The missing exchange of information is similar to the problems described for multiple point initiators (Sec. 5.4). For large structures, however, a superposition of each of the deformation waves according to the concept proposed in Sec. 5.4.2 is computationally not feasible. Therefore, a different approach for handling the superposition of deformation information from initiating structures is introduced. The exchange of deformation information is approximated by adjusting the flow of deformation information along the wave-fronts, i.e. by adjusting the processing order during deformation propagation.

5.5.1. Basic Shapes

Since the CM-elements are arranged in a rectangular CM-grid, the surface of arbitrary initiating structures is composed of a limited number of geometric shapes. In the following, the general concepts for how to adjust the processing order are explained in detail for basic 2D-shapes.

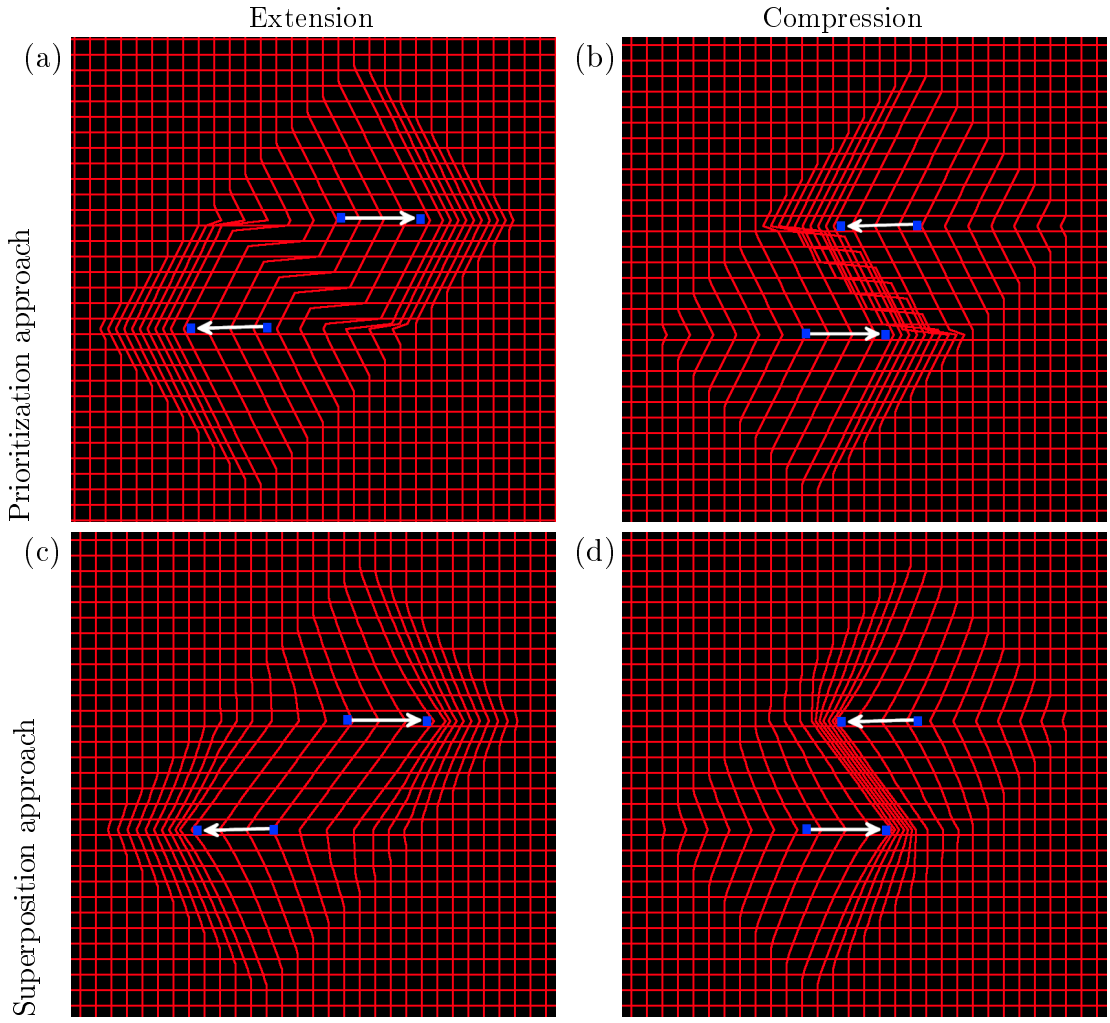

Figure 20.: Illustration of 2D deformation grids, resulting from the prioritization approach (upper row) and from the superposition approach with $n = 1$ (lower row). The grids result for two initiators being torn apart (left columns) and being pushed together (right column). The initial and final positions of the initiators are indicated by the blue points, the displacement directions by the white arrows.

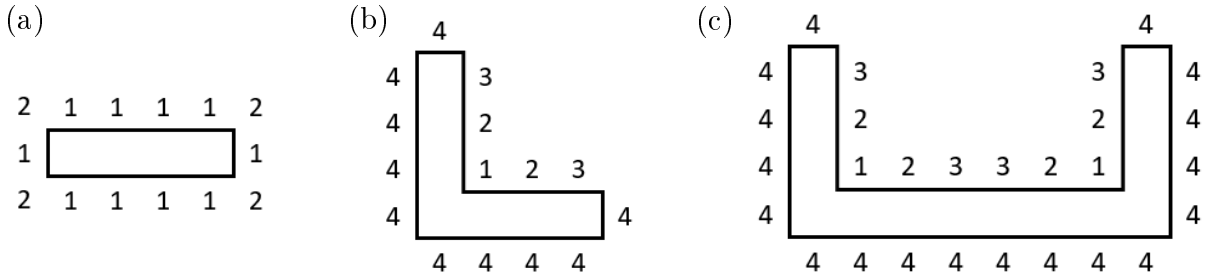

Figure 21.: Depiction of the priorities, with which CM-elements are processed during deformation propagation, for basic 2D-shapes (a) Rectangular shape (b) L-shape (c) U-shape. Elements with equal priority are processed in a random order.

Rectangular Shape

The simplest shape of an initiating structure is a rectangle (Fig. 21a). For this shape all CM-elements on a wave-front have the same priority, no adjustment of the processing order is required. The handling of the multiple initiators within the rectangle is in accordance with the concept of prioritization proposed for multiple initiators in Sec. 5.4.1.

L-shape

The next level of complexity is introduced by an L-shaped structure (Fig. 21b). Inside the L-shape superposition of deformation information is required, whereas deformation propagation directed outside of the L-shape can be treated in the same way as for the rectangular structure. In order to simplify the process of superposition (Sec. 5.4.2), the averaging of deformation information is directly integrated into the process of propagation. CM-elements on the same wave-front are allowed to affect neighboring CM-elements, if they carry more deformation information than the respective neighbor. This behavior is implemented by introducing a second sorting criterion for the priority queue (Sec. 2.4) which prioritizes those elements that have obtained deformation information from more than one neighboring element. For these elements, deformation information is averaged according to Eq. 5.7.

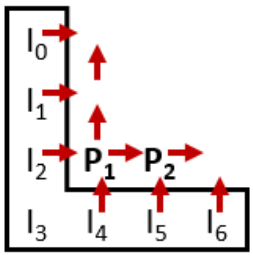

Figure 22.: Exemplary processing of deformation propagation for the inner area of an L-shaped structure. Those CM-elements that obtain deformation information from the largest number of neighbors, are assigned the highest priority. In this way, the deformation propagation along the wave-front starts in the edge of the L and is sequentially propagated along the bars.

An exemplary deformation propagation for an L-shaped structure is illustrated in Fig. 22. The initiating CM-elements I_2 and I_4 both propagate their deformation information to the common neighboring CM-element P_1, which is processed with highest priority. Its final position $\boldsymbol{p'_1}$ is determined by superposition of the position $\boldsymbol{p'_1}(I_2)$ obtained from the deformation information of I_2 and of the position $\boldsymbol{p'_1}(I_4)$ obtained from I_4. The positions are weighted by the respective timestamps $t(I_2, P_1)$ and $t(I_4, P_1)$ according to Eq. 5.7:

$$\boldsymbol{p}'_1 = \left(\frac{1}{t(I_2,P_1)} + \frac{1}{t(I_4,P_1)}\right)^{-1} \cdot \left(\frac{1}{t(I_2,P_1)} \cdot \boldsymbol{p'_1}(I_2) + \frac{1}{t(I_4,P_1)} \cdot \boldsymbol{p'_1}(I_4)\right). \tag{5.9}$$

When CM-element P_1 is processed, it functions as an initiating element for the CM-element P_2, which is the next to be processed. The final position for P_2 is calculated according to:

$$\boldsymbol{p}'_2 = \left(\frac{1}{t(I_5,P_2)} + \frac{1}{t(I_{2/4},P_1,P_2)}\right)^{-1} \cdot \left(\frac{1}{t(I_5,P_2)} \cdot \boldsymbol{p'_2}(I_5) + \frac{1}{t(I_{2/4},P_1,P_2)} \cdot \boldsymbol{p'_2}(P_1)\right), \tag{5.10}$$

with $t(I_{2/4}, P_1, P_2)$ being the time the deformation takes for propagation along the path from I_2, respectively I_4, to P_1 to P_2. Deformation propagation is continued along both bars of the L-shape until the surface boundary is reached. Only then the other CM-elements at the outer surface of the L-shape are processed. In this way it is ensured that an element only affects a certain neighboring element if the element itself carries more deformation information than the respective neighbor.

U-shape

The third level of complexity is introduced by a U-shaped structure (Fig. 21c). This structure can be considered as a combination of two L-shapes so that superposition is required for deformation information inside the U-shape. In this case it has to be ensured that the deformation information originating from the two corners is uniformly propagated inwards as illustrated in Fig. 21c. This is implemented by introducing a third sorting criterion for the priority queue (Sec. 2.4) which prioritizes those CM-elements that have the most CM-elements with averaged information along their propagation path. The final displacement vectors are calculated in the same way as for the L-shape (Eqs. 5.9, 5.10).

3D shapes

The handling of 3D-initiating structures works according to the same principles as for 2D-structures. The newly introduced sorting criteria are based on the number of CM-elements along the deformation path, which show certain characteristics. In 3D, the number of neighboring elements increases from 4 to 6. Therefore, the range of values each sorting criterion can take increases. The transfer of the presented concepts to 3D needs no further adaptions.

5.5.2. Deformation Results

Figure 23a shows the deformation grid resulting from a translation of a rigid rectangular structure in homogeneous soft tissue for a processing order based on timestamps. It shows no grid irregularities. For simple structures like the rectangular shape, all deformation waves originating from the surface are propagated outwards so that they do not directly meet. Therefore, even with a simple processing order only by timestamps no deformation information gets lost.
Figure 23b and 23c show the deformation grids resulting from a translation of an L-shaped structure in homogeneous soft tissue for a processing order based only on timestamps and based on the newly introduced second sorting criterion. For a processing order based only on timestamps, the grid shows irregularities in the area between the bars of the L (Fig. 23b). A diagonal borderline is observed which separates elements which have obtained deformation information from the vertical bar, from those which have obtained information from the horizontal bar. This observation results from the deformation waves directing inside the L-shape, which directly meet. CM-elements closer to the horizontal bar of the L-shape obtain only shear information, whereas CM-elements closer to the vertical bar obtain only compression information, resulting in the observed diagonal borderline.
This behavior is improved by introducing a flow of information along the wave fronts. On each wave-front inside the L-shape, the flow of information is assumed to start in the corner of the L-shape where the deformation information of the two bars of the L-shape is averaged. Based on the newly introduced second sorting criterion, this averaged information is propagated outwards along the bars. In this way the deformation on the individual wave-fronts is propagated along

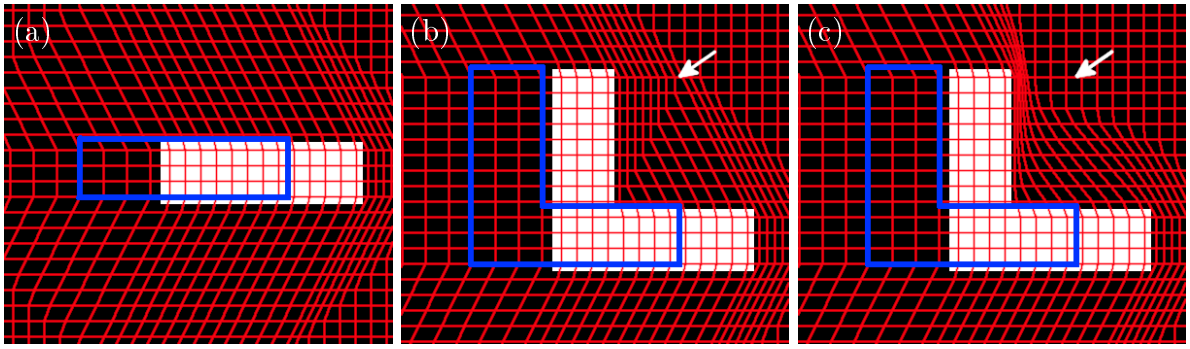

Figure 23.: Illustration of 2D-deformation grids for propagation of an initial translation in x-direction of initiating structures. The original position of the structures is indicated by the blue contours. (a) Rectangular shape with timestamp-based propagation. (b) L-shape with timestamp-based propagation. The arrow marks the observed grid irregularity. (c) L-shape with timestamp-based propagation and the additional second sorting criterion. The arrow marks the location of the grid irregularity indicated in b.

the path of 'highest information'. With introduction of the second sorting criterion no borderline is observed any more. CM-elements close to the vertical bar are compressed, the amount of compression increases with increasing distance from the horizontal bar. CM-elements close to the horizontal bar are sheared, with the amount of shear increasing with increasing distance from the vertical bar. The overall grid shows no unexpected irregularities (Fig. 23c).
Figure 24 shows the deformation grids for translation of a U-shaped structure in homogeneous soft tissue, for a processing order based on timestamps and the newly introduced second and third sorting criterion. For a U-shaped structure, even after the introduction of the second sorting criterion, grid irregularities occur for deformation waves originating from inside the U-shape as indicated in Fig. 24. They result from differences in the processing order along subsequent wave fronts. On each wave front the deformations start in the corners of the U-shape. However, only the direction of propagation (inside along the horizontal bar), but not the order of propagation is specified. Therefore, on some wave fronts CM-elements at the center of the horizontal bar obtain deformation information from the left bar and on other wave fronts they obtain information from the right bar. The introduction of the third sorting criterion ensures that deformation propagation takes the same path on all wave fronts and in this way resolves the grid folding observed before (Fig. 24b).
Realistic structures combine all aspects discussed for the basic shapes. Additional shapes that could be considered are an O-shape. The introduction of the new sorting criteria highly improves the physical plausibility of the deformation grid, as illustrated for the example of a vertebra (Fig. 25). For the simple timestamp propagation, irregularities as observed for the L-shape occur as indicated by the white arrows (Fig. 25a). With introduction of the second sorting criterion, these irregularities are dissolved. However grid folding as observed for the U-shape occurs, as indicated by the white arrow (Fig. 25b). With the introduction of a third sorting criterion, also this problem is resolved (Fig. 25c).

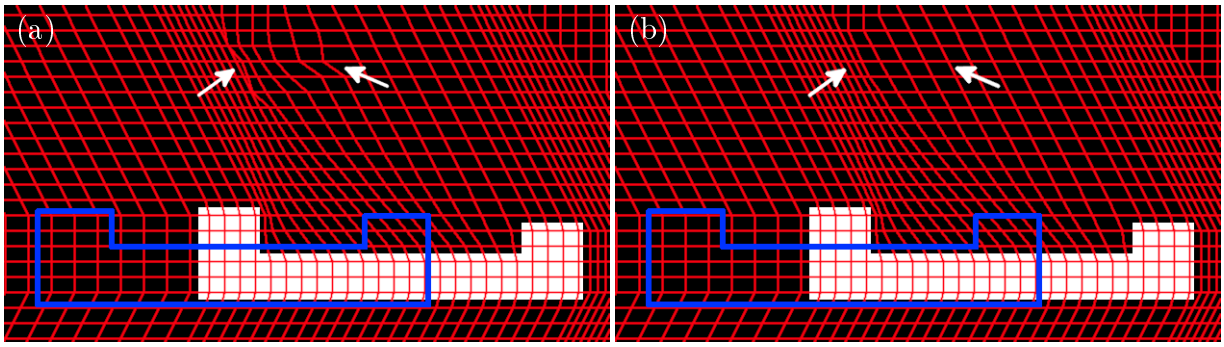

Figure 24.: Illustration of 2D-deformation grids for propagation of an initial translation of an initiating U-shape in x-direction. The original position of the U-shape is indicated by the blue contours. (a) Timestamp-based propagation with the additional second sorting criterion. The arrows mark exemplary grid irregularities. (b) Timestamp-based propagation with the additional second and third sorting criterion. The arrows mark the resolved grid irregularities.

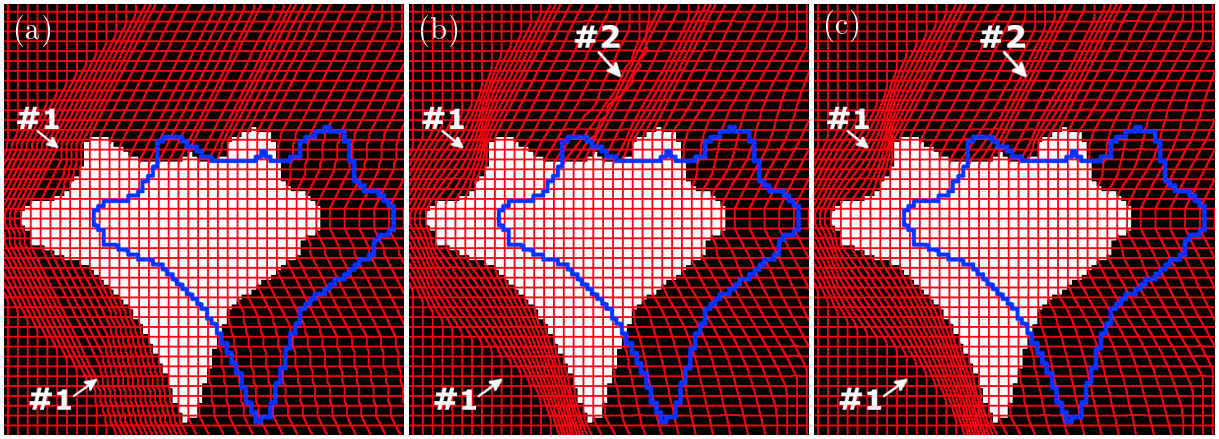

Figure 25.: Illustration of 2D-deformation grids for propagation of an initial translation in x-direction of a vertebra. The original position of the vertebra is indicated by the blue contours. (a) Timestamp-based propagation, grid irregularities resulting from an L-shape are marked by arrows 1. (b) Timstamp-based propagation with the additional second sorting criterion. The irregularities marked by 1 are resolved. New grid irregularities, resulting from a U-shape are marked by arrow 2. (c) Timstamp-based propagation with the additional second and third sorting criterion. The grid irregularities resulting from L-and U-shape are resolved.

Summary

In this section, the processing order within the CM-concept was enhanced by additional sorting criteria, which compensate for deformation artifacts that occur due to initiating structures. The considered basic shaped were an L- an a U-shape. Combinations of these shapes, e.g. to an O-shape are expected to also be covered by the developed concepts.
However, e.g. in the middle of the U-shape (Fig. 29c, Fig. 24) a sharp borderline reminding of the borderlines observed in the prioritization approach (Sec. 5.4.1) are observed. At this point an exchange of information between the vertical bars of the U is missing. For complex combinations of basic shapes as occur in the human anatomy this missing information exchange could result in grid irregularities and should be addressed in future work.

6. Deformation Results for Human Anatomies

In this chapter, the different stages of model development are evaluated based on two head and neck CT data sets which represent two different deformation ranges. The evaluation of the model performance is focused to the physical and anatomical plausibility of the DVFs, since this is a necessary condition for the biofidelity of a deformation model. The resulting final version of the soft-tissue deformation model is compared to two exemplary state-of-the art deformation models, also with the focus on the biofidelity of the deformations. The model input is approximated by the bone transformations, i.e. by a system of multiple initiating structures. In the following, the terms initiators and bones will be used equivalently. The transformation parameters of the bones are obtained from a biomechanically driven image registration of the skeleton, between the planning CT and respectively fraction or post-treatment CT (Sec. 4.2.1).

6.1. Model Evaluation

In the following, the deformation results for the different stages of model development are presented. For a qualitative evaluation of the deformation properties, visualizations of the DVF, Jacobian maps (Sec. 4.3.2) and the artificially deformed images are investigated. For a quantitative evaluation, the characteristic values of the Jacobian distributions are analyzed. For patient 1, additionally a set of exemplary landmarks is used for estimating the model accuracy. However, the significance of the landmark evaluation is limited since the number of landmarks within soft tissue is low and they are not evenly distributed.

6.1.1. Model Input

The basic model input are the patient images, which are the basis for generating the CM-grid. The grid is set up in a way that each CM-element corresponds to an image voxel, so that the deformation is modeled at the same resolution as the provided data. The deformation is initialized by the transformation parameter of the bones. Figure 26 and Fig. 27 illustrate the quality of the deformation input for patient 1 and respectively 2, based on fusion views for the bones. For patient 1, which represents a small-range deformation, the alignment is very good. For patient 2, representing a large-range deformation, the alignment is good for the skull, mandible, humeri and scapulae, but obvious deviations are present for the claviculae and some vertebrae.

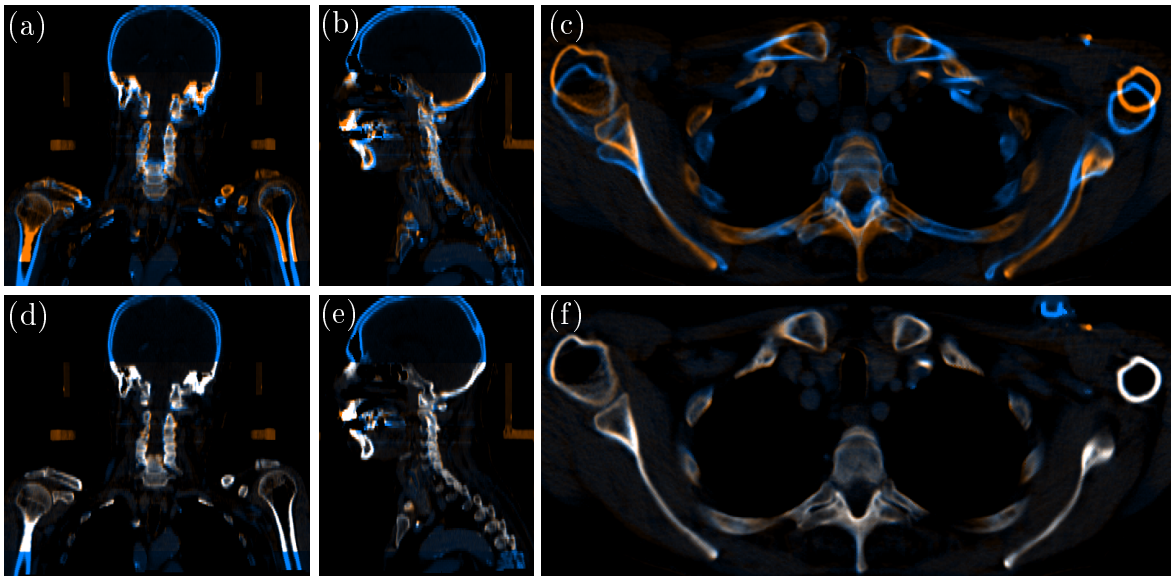

Figure 26.: Illustration of the quality of the deformation input for patient 1, based on an exemplary frontal (first column), sagittal (second column) and transversal (third column) slice. In the upper row, a color fusion of the planning CT (blue) with the fraction CT (orange) is shown. In the lower row, a color fusion of the planning CT (blue) with the bone configuration used for model input (orange) is shown.

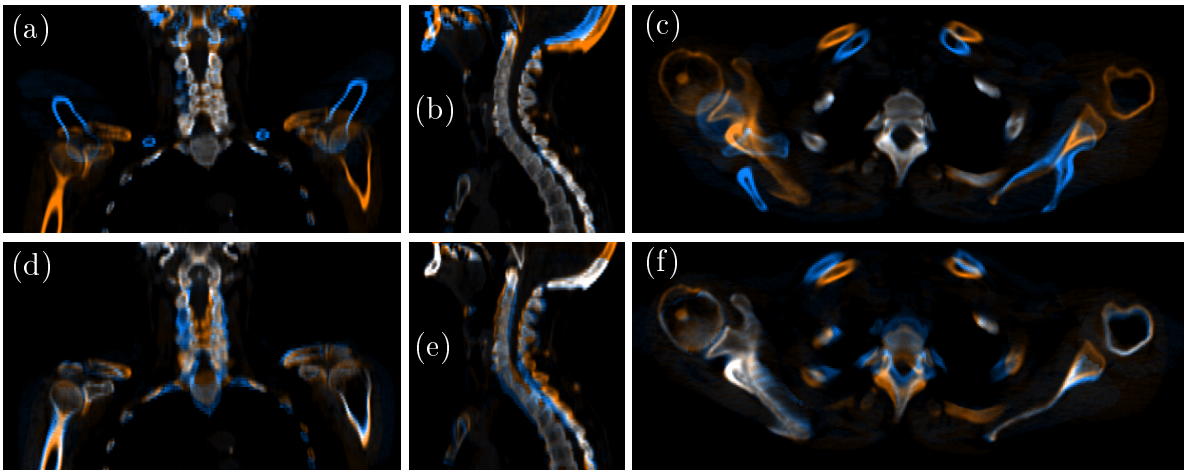

Figure 27.: Illustration of the quality of the deformation input for patient 2, based on an exemplary frontal (first column), sagittal (second column) and transversal (third column) slice. In the upper row, a color fusion of the planning CT (blue) with the fraction CT (orange) is shown. In the lower row, a color fusion of the planning CT (blue) with the bone configuration used for model input (orange) is shown.

6.1.2. Processing Order

In the following, the influence of the two sorting criteria introduced in Sec. 5.2 on the overall processing order and deformation results is investigated for real patient data. To investigate the local deformation behavior without any interaction between the different initiators, multiple initiators are handled by the prioritization approach (Sec. 5.4.1). So each initiator has a

restricted region of influence to which its deformation information is propagated. These regions are separated by sharp borderlines.

Figure 28 illustrates the deformation results for the two sorting criteria, based on parameterization by the stiff parameter set (Sec. 5.1) for the small deformation magnitude, represented by patient 1. The extent of the regions of influence, illustrated by different colors overlayed on the original planning CT, strongly dependens on the sorting criterion (first column). For a processing order based on constraint violation (upper row), the region of influence for the humerus (yellow) dominates almost the whole depicted image slice. The borderlines between the regions of influence are mainly located directly at or close to the surface of the other bones. For a processing order based on timestamps (lower row), the extent of the region of influence for the humerus decreases, while the regions of influence of the other bones, especially of the scapula (turquoise), increase. The borderlines between the different regions are shifted from the bone surfaces into soft tissue regions.
At these borderlines, DVF irregularities occur, as illustrated by the DVFs (first column) and by the Jacobian maps (second column). For a processing order based on constraint violation, the borderline irregularities are very large. The Jacobian map shows either grid folding (black areas, arrow 1) or an extreme volume increase (red areas, arrow 2) for borderline voxels. For a processing order based on timestamps, the borderline irregularities are less prominent. The Jacobian map in Fig. 28e shows less grid folding and less extreme volume increase, however, especially at the borderline between the regions of influence of scapula and ribs grid folding still occurs (arrows 1,2). This will be addressed in Sec. 6.1.4.
In addition to the DVF at the borderlines, also the DVF within the individual regions of influence has to be investigated. For a processing order based on constraint violation, most voxels in the depicted slice lie in the region of influence of the humerus. At the surface of the humerus, which is mostly located within the region of influence, grid irregularities, similar to the borderline irregularities are observed (Fig. 28b, arrows 3,4). These irregularities indicate a failure of the processing based on constraint violation. By introduction of a processing order based on timestamps, the DVF irregularities at the humerus surface are dissolved. However, new small DVF irregularities arise within the individual regions of influence (Fig 28e, arrow 5). These will be addressed in the next sections.
The artificially deformed images (Fig. 28, third column) show image artifacts in those regions in which DVF irregularities were observed. For the processing order based on constraint violation, the artifacts are most prominent in the bones, which are not correctly resampled. The scapula is even torn apart (Fig. 28c, arrow 6). For a processing order based on timestamps, the bones are resampled correctly (Fig. 28f). The borderline irregularities are mainly located in soft tissue regions with low image contrast, so although they are detected in the Jacobian map they are hardly visible in the artificially deformed image.

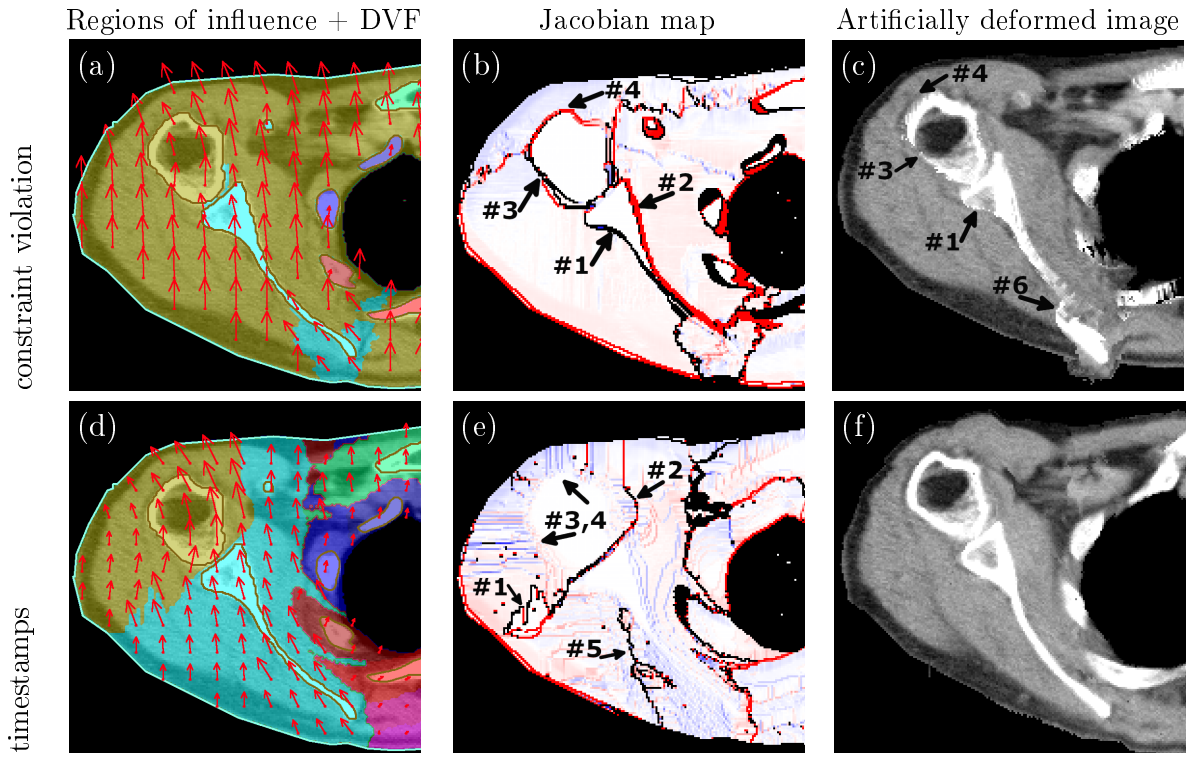

Figure 28.: Illustration of the influence of the processing order on the deformation results for patient 1 and the stiff parameter set. For the sorting by constraint violation (upper row), as well as for the sorting by timestamps (lower row), a detail of a transversal slice shows the regions of influence for the individual bones, and the according DVF, both overlayed on the planning CT (first column), the Jacobian map (second column) and the artificially deformed image (third column). A general explanation of Jacobian maps can be found in Sec. 4.3.2. Arrows 1 and 2 mark borderline irregularities between the regions of influence of scapula and humerus. Arrows 3-5 mark DVF irregularities within regions of influence. Arrow 6 marks the disrupted scapula, as an example for an obvious image artifact which results from grid irregularities.

Figure 29 illustrates the deformation results for the different sorting criteria for patient 1, with the elastic parameter set, instead of the rigid one presented in Fig. 28. For the processing order based on constraint violation (upper row), the regions of influence show a strong dependency on the parameterization. Compared to the stiff parameter set, the region of influence of the humerus (yellow) decreases in size, while the other initiators gain influence. For a processing order based on timestamps (lower row), the regions of influence show no dependency on the parameterization.

For both sorting criteria, the resulting DVFs (first column) show similar borderline irregularities as observed for the stiff parameter set, although they are less distinct. This is also depicted in the corresponding Jacobian maps (second column). Compared to the stiff parameter set, the Jacobian maps show an overall broader distribution of Jacobian values in soft tissue, i.e. larger volume changes of the individual voxels. For the processing order based on timestamps, the initial displacements are absorbed faster during the process of deformation propagation, so that certain regions at the patient surface are not deformed at all (Fig. 29e, arrow 1). An example for an unrealistically large volume change, is the compression of fatty tissue at the frontal surface of the patient. In the Jacobian map this appears as a bluish region (Fig. 29e, arrow 2).

The artificially deformed images show the same artifacts as for the stiff parameterization, only

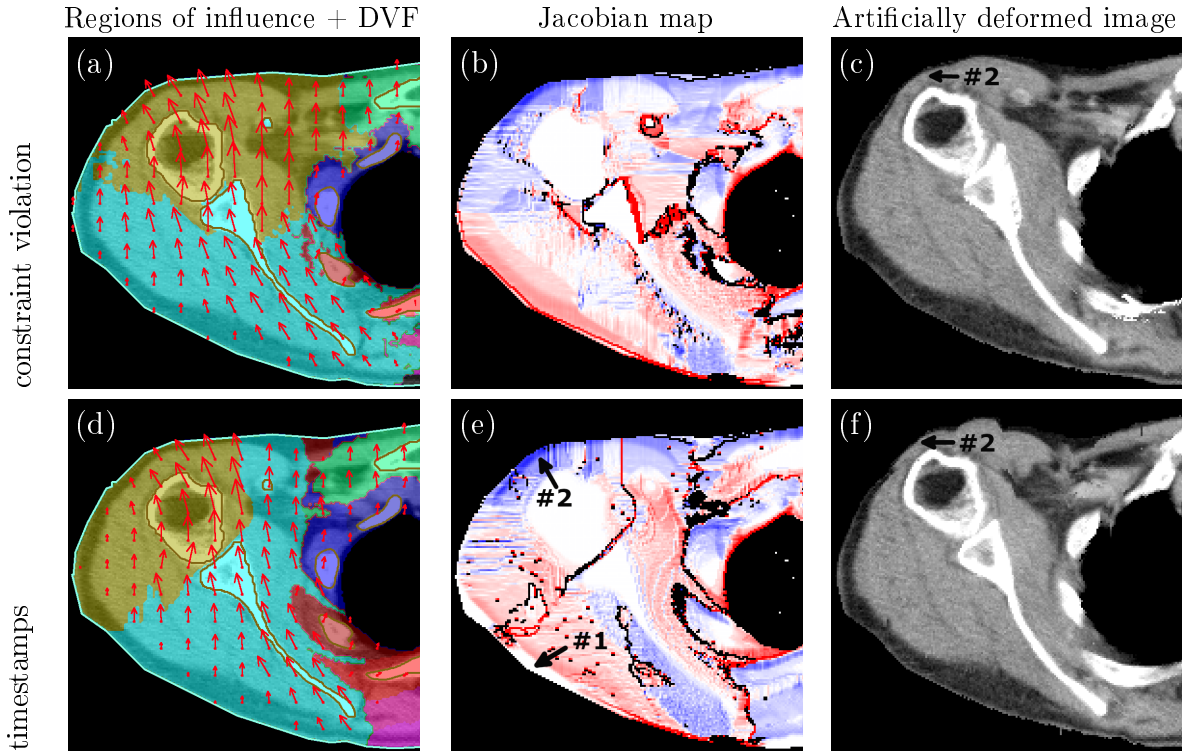

Figure 29.: Illustration of the influence of the processing order on the deformation results for patient 1 and the elastic parameter set. For the sorting by constraint violation (upper row), as well as for the sorting by timestamps (lower row), a detail of a transversal slice shows the regions of influence for the individual bones and the according DVF, both overlayed on the planning CT (first column), the Jacobian map (second column) and the artificially deformed image (third column). Arrow 1 marks CM-elements at the patient's surface, that are not reached by deformation propagation with the elastic parameter set. Arrow 2 marks strong compression of fatty tissue at the patient's surface.

less distinct (Fig. 29, third column). The compression of the fatty tissue, observed in the Jacobian map, becomes visible for both sorting criteria, as marked by arrow 2.

Figure 30 illustrates the deformation results for the timestamp-based processing, based on parameterization by the elastic parameter set for patient 2. For the constraint-based processing order, the DVF shows severe irregularities, which result in a failure of the resampling of the artificially deformed images. Therefore, in the following only the results for the superior timestamp-based processing order are investigated.
The Jacobian maps (Fig. 30, second column) show large areas of grid folding (black areas), not only at borderlines between regions of influence but also within the individual regions of influence, mainly for the humerus. This is also reflected in the artificially deformed images (third row), which show many artifacts, like soft tissue being folded onto bones (arrow 1), or the arm being only partly visible (arrow 2).

Table 3 compares the characteristic values of the Jacobian distributions for the two sorting criteria, both parameter sets, and for both patients. For patient 1, the introduction of timestamps results in decreasing characteristic values for the stiff parameter set and in increasing Jacobian values for the elastic parameter set. Overall, the elastic parameter set yields better results concerning the physical plausibility of the deformations. For patient 2, which represents a large-

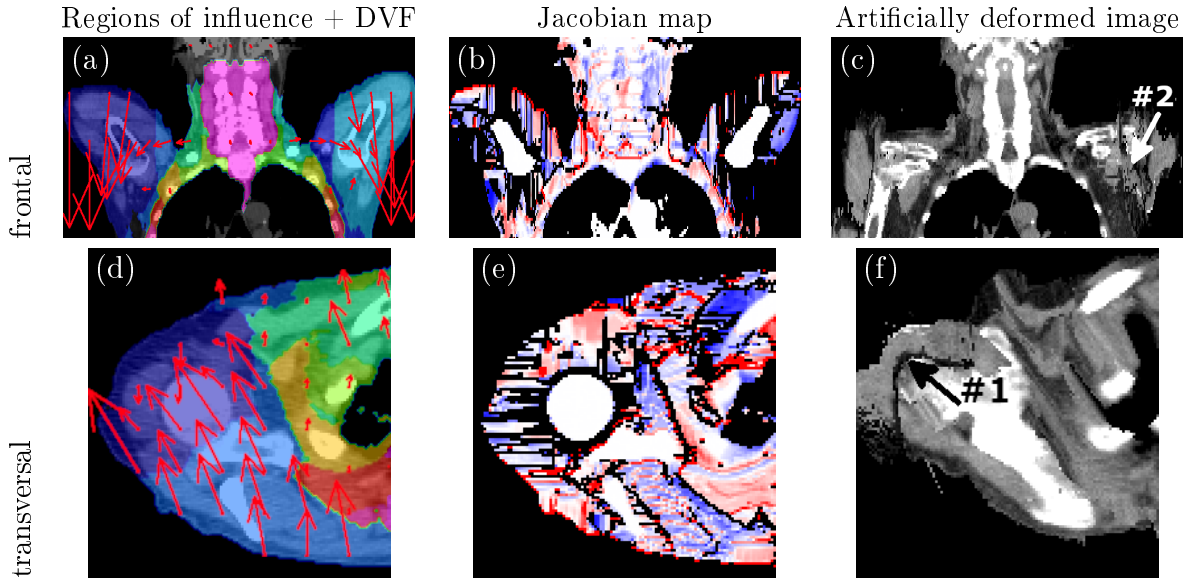

Figure 30.: Illustration of the deformation results for a processing order based on timestamps for patient 2 and the elastic parameter set. For a frontal slice (upper row) and a detail of a transversal slice (lower row), the regions of influence for the individual bones and the according DVF, both overlayed on the planning CT (first column), the Jacobian map (second column) and the artificially deformed image (third column) are shown. Arrow 1 marks an area, where soft-tissue is folded onto the humerus. Arrow 2 marks an area where the resampling of the humerus fails, due to an erroneous DVF.

range deformation, all characteristic values of the Jacobian distributions are increased compared to the small-range deformation of patient 1. For this patient the stiff parameter set yields better results than the elastic parameter set.

	patient 1				patient2	
	stiff		elastic		stiff	elastic
char. values	constr. viol.	timestamps	constr. viol.	timestamps	timestamps	
$J_{<0}$ [%]	8.7	8.1	4.5	5.3	22.7	23.8
$J_{>2}$ [%]	5.0	1.8	1.5	1.9	4.2	5.2
$J_{<0.5}$ [%]	0.2	0.5	2.7	3.0	1.5	3.0
$J_{\varnothing}$	1.25	1.05	1.02	1.02	1.50	1.54
J_{max}	83	32	17	25	258	258

Table 3.: Comparison of the characteristic values for the Jacobian distributions of a processing order based on constraint-violation and a processing order based on timestamps, for both parameter sets and deformation magnitudes, i.e. patients.

Table 4 depicts the mean relative residuals, as well as the standard deviation of the investigated soft-tissue landmarks. Upon the introduction of timestamps, the mean residuals strongly decrease for the stiff parameter set and slightly increase for the elastic parameter set. The overall smallest residuals are observed for a processing order based on timestamps and the stiff parameter set.

Summary For a processing order based on constraint-violation, the deformations propagate along the path of the largest absolute displacements. If multiple initiators are present, this

	stiff		elastic	
relative residuals	constr. viol.	timestamps	constr. viol.	timestamps
mean	1.82	0.74	0.81	0.84
std	0.86	0.27	0.26	0.20

Table 4.: Comparison of the mean relative residuals and standard deviation of a processing order based on constraint-violation and a processing order based on timestamps, for both parameter sets and patient 1.

means that the deformation with the largest initial displacement is propagated with highest priority. The initiator with the largest initial displacement, i.e. the humerus, has the largest overall region of influence, as illustrated in Fig. 28a. With the introduction of a processing order based on timestamps, the borderlines between the regions of influence are shifted to those positions which have the same temporal distance to the initiators. These are located within soft-tissue regions. Borderline irregularities still occur, if the information of the different initiators is conflicting as e.g. in the joint between humerus and scapula or between the scapula and the ribs. The handling of these DVF singularities will be further addressed in Sec. 6.1.4.
If rotated initiating structures are present, the length of the initial displacement vectors further varies within the individual structures. In this case, a deformation propagation along the path of largest constraints shows a directional bias within the individual regions of influence, which depends on the orientation of the initial rotation and on the geometry of the initiating structure itself. This is illustrated e.g. in Fig. 28a, where the humerus shows displacement vectors which decrease from medial to lateral direction. The deformation is propagated faster into medial direction and as a result the observed DVF irregularities at the surface of the humerus occur (Fig. 28a,b). Upon the introduction of timestamps, those DVF irregularities within the individual regions of influence which result from rotated initiating structures are resolved (Fig. 28d,e). The newly arisen small and irregularly distributed DVF irregularities in the muscular regions next to humerus and scapula can be attributed to the missing concept for rotational degrees of freedom, which will be further addressed in Sec. 6.1.3.

For the stiff parameter set and patient 1 an improvement of the characteristic values of the Jacobian distribution upon introduction of timestamps is observed. This can be explained by the fact that large DVF irregularities occur mainly at the borderlines between the different regions of influence. By the introduction of timestamps the regions of influence are redistributed and borderline irregularities are reduced. The newly arisen DVF irregularities within the individual regions of influence are small compared to the borderline irregularities so that an overall improvement of the characteristic values is observed. For the elastic parameter set, the characteristic values of the Jacobian distribution deteriorate upon the introduction of timestamp propagation. The overall borderline irregularities are smaller than for the rigid parameter set. Therefore, the newly arisen DVF irregularities have a larger overall weight and no improvement of the characteristic values is observed upon the introduction of timestamps.
The mean residuals also strongly decrease upon the introduction of timestamps, for the rigid parameter set. The model accuracy improves mainly in those regions, which fall into an incorrect region of influence for a constraint-based processing order. For the stiff parameter set, large changes in the extent of the regions of influence is observed upon the introduction of timestamps. Therefore, the largest improvement is observed for this parameter set. However, as discussed in the previous section, the limited number of landmarks allows no general statement about the model accuracy.

The differences in deformation magnitude between patient 1 and patient 2 result in a much more irregular DVF for the large-range deformation. Comparing the stiff and the elastic parameter set for the two deformation magnitudes, the small-range deformation showed lower characteristic values of the Jacobian distribution for the elastic parameter set, whereas the large-range deformation showed lower characteristic values for the stiff parameter set. The influences of the different parameterizations will be further investigated in the following sections.

6.1.3. Rotation

With the introduction of rotational degrees of freedom, the initiating transformations of the bones are considered as a combination of translation and rotation. The rotation points are individually defined for each bone, as the respective bone centroids. In the head and neck region, humerus and scapula are the bones with the largest rotation range. Therefore, the introduction of a concept to handle inter-element rotation into the CM-approach is expected to show the largest effect in the regions of influence of these bones. In the following, the influence of the two approaches of handling rotational degrees of freedom introduced in Sec. 5.3 on the deformation results is investigated. For the processing order, a sorting by timestamps is used, the multiple initiators are handled by the prioritization approach (Sec. 5.4.1), which will be investigated in detail in the next section.

Figure 31 illustrates the deformation results for the two approaches of handling rotational degrees of freedom for the small deformation magnitude, represented by patient 1. For both approaches, the DVFs look similar on the large scale (first column), showing borderline irregularities mainly between the regions of influence for humerus and scapula. For the elastic parameter set (Fig. 31g), these DVF irregularities, are less pronounced than for the stiff parameter set.
The Jacobian maps (second column) illustrate, that all bones have a Jacobian value of 1, i.e. they conserve their volume. The Jacobian maps further show, that for the constraint-based approach many small DVF irregularities arise within the individual regions of influence. These irregularities are resolved by the linear-decay approach. For the elastic parameter set (Fig. 31h), the Jacobian map shows small areas of extreme volume changes in the regions influenced by the ribs, as exemplary indicated for an area with high volume increase (reddish).
For both approaches, the artificially deformed images (third column), show an image artifact at the borderline between the regions of influence of humerus and scapula, which is marked by arrow 1. All other DVF irregularities are located in homogeneous tissue regions and therefore hardly visible in the images. For the elastic parameter set, the image artifact at the borderline between the regions of influence of humerus and scapula is not visible any more. However, the large volume changes in proximity to the ribs, result in soft tissue spreading into the lung, as indicated by arrow 2. All in all, the linear-decay approach results in a better DVF regularity than the constraint-based approach.
Comparing the results for the superior linear-decay approach to the results presented in the previous section, the largest changes in the DVF are observed in the regions of influence of humerus and scapula (compare Fig. 28d, Fig. 31d). This results in increased discrepancies at the borderlines, which result e.g. in the image artifact described above (compare Fig. 28f, Fig. 31f, arrow 1). Within the individual regions of influence, however, the Jacobian maps show a high improvement of DVF regularity upon the introduction of rotational degrees of freedom by the linear-decay approach.

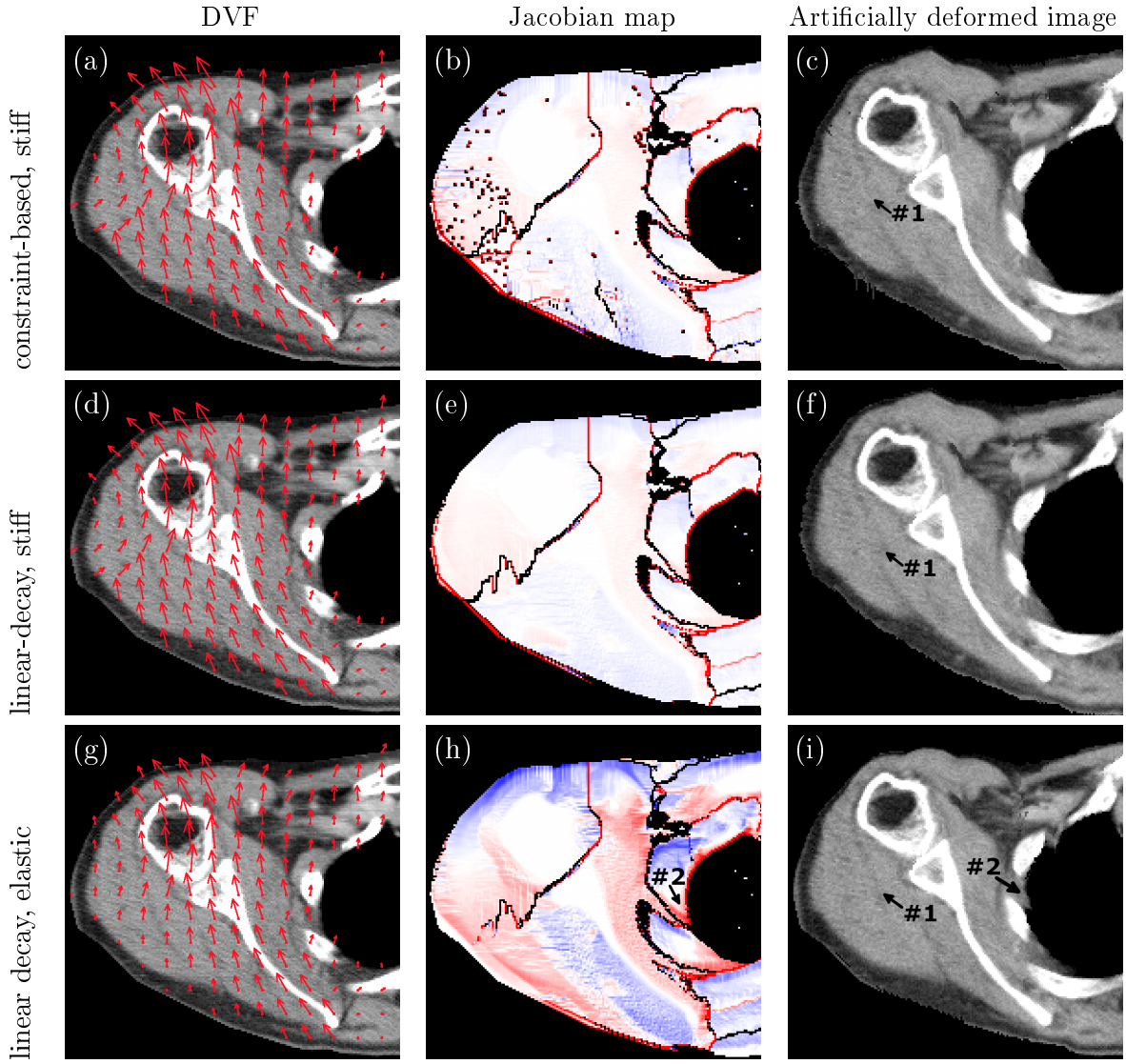

Figure 31.: Illustration of the influence of the two approaches to handle rotational degrees of freedom on the deformation results for patient 1. For the constraint-based approach and the stiff parameter set (upper row), the linear-decay approach and the stiff parameter set (middle row) and for the linear-decay approach and the elastic parameter set (lower row), the DVF overlayed on the planning CT (first column), the Jacobian map (second column) and the artificially deformed images (third column) are shown. Arrow 1 marks an image artifact in the deformed image that results from borderline DVF irregularities. Arrow 2 marks an area of unrealistically large volume changes, resulting in soft-tissue spreading into the lung.

Figure 32 illustrates the deformation results for the two approaches of handling rotational degrees of freedom for the large deformation magnitude, represented by patient 2. For the constraint-based approach and the stiff parameter set (upper row), extreme DVF irregularities are observed, mainly within the regions of influence of the humeri, as illustrated by the Jacobian maps. Especially the large areas of grid folding (black) are highly problematic (Fig. 32b, arrows 1,2). The artificially deformed image (Fig. 32c) shows the resulting image artifacts, for example the disruption of the muscle structures of the right arm, and even the left humerus bone.
For the linear-decay approach and the stiff parameter set (middle row), no DVF irregularities

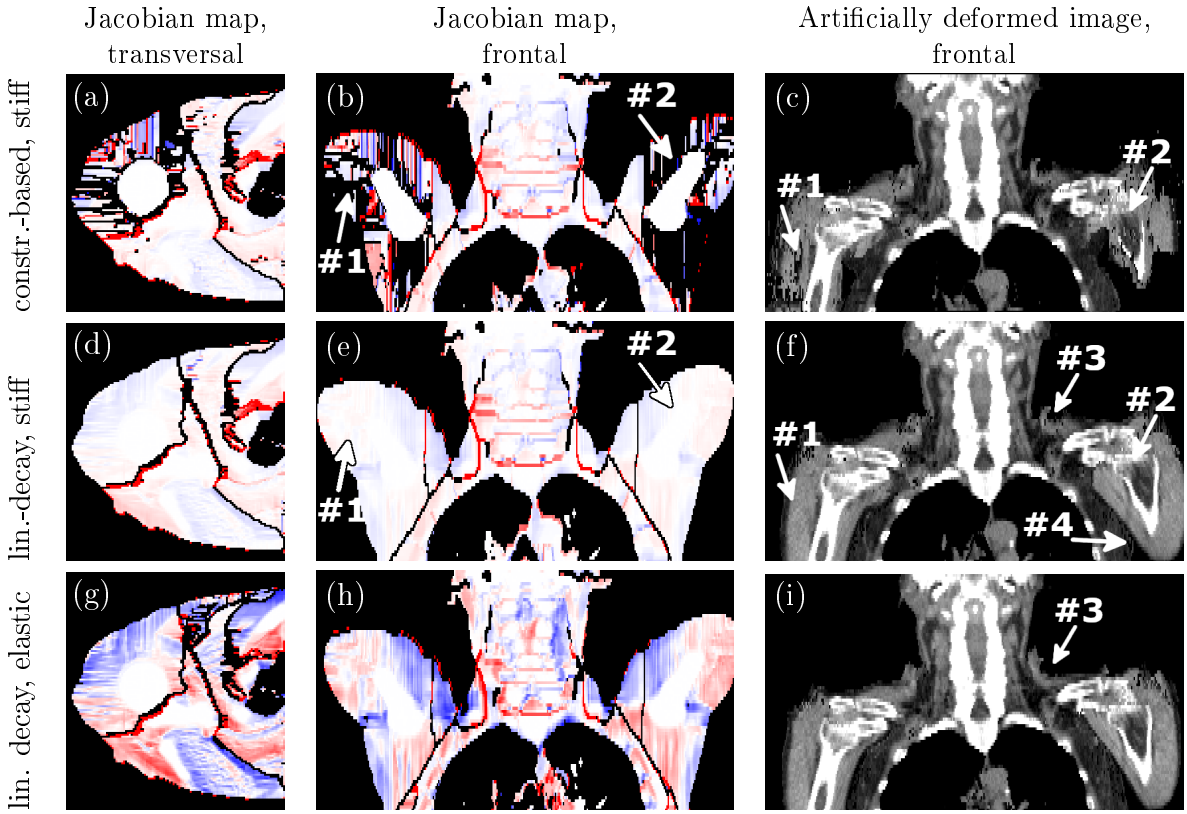

Figure 32.: Illustration of the influence of the two approaches to handle rotational degrees of freedom on the deformation results for patient 2. For the constraint-based approach and the stiff parameter set (upper row), the linear-decay approach and the stiff parameter set (middle row) and for the linear-decay approach and the elastic parameter set (lower row) the Jacobian map of a transversal slice (first column) and a frontal slice (second column), as well as a frontal slice of the artificially deformed images (third column) are shown. Arrows 1 and 2 mark large areas of grid folding and the corresponding image artifacts in the deformed image. Arrows 3 and 4 mark an image artifacts in the shoulder region, and at the border between arm and thorax.

within the individual regions of influence are observed, the only irregularities are those at the borderlines between different regions of influence. As a result, also the extreme image artifacts are resolved (Fig. 32f). Small image artifacts still occur at the patient surface, in the region of the shoulders and in the region where the arm and the thorax meet.
For the elastic parameter set and the linear-decay approach (lower row), the observed borderline irregularities are very similar to those for the rigid parameter set. The overall distribution of Jacobian values has become broader, as was also observed in the previous section. Finally, the image artifacts at the shoulder surfaces are reduced compared to the stiff parameter set, but still visible (Fig. 32f).

Table 5 compares the characteristic values of the Jacobian distributions for the two rotation approaches, the different parameter sets, and for both patients. For the small-range deformation of patient 1, the linear-decay approach improves all characteristic values, except for $J_{<0.5}$, compared to the constraint-based approach. Overall, the elastic parameter set yields better results concerning the physical plausibility of the deformations than the stiff parameter set. For the large-range deformation of patient 2, the linear-decay approach improves all characteristic val-

ues, except for J_{max}, compared to the constraint-based approach. For this patient, the differences between the constraint-based and the linear-decay approach are much more pronounced than for the small-range deformation of patient 1. Comparing the two parameter sets, the stiff parameter set yields better overall results. Comparing the characteristic values to those in the previous section (Tab. 3), an improvement upon the introduction of a rotation handling was achieved for both patients and parameter sets.

	patient 1				patient2			
	stiff		elastic		stiff		elastic	
char. values	cB	lD	cB	lD	cB	lD	cB	lD
$J_{<0}$ [%]	8.3	7.5	5.6	4.7	18.7	7.8	22.0	9.9
$J_{>2}$ [%]	2.1	1.8	2.1	1.7	4.0	2.5	5.0	3.0
$J_{<0.5}$ [%]	0.4	0.4	3.1	3.6	0.9	0.2	2.9	2.7
$J_{\varnothing}$	1.06	1.05	1.02	1.01	1.50	1.23	1.50	1.27
J_{max}	53	49	28	16	326	396	268	618

Table 5.: Comparison of the characteristic values for the Jacobian distributions of the constraint-based (cB) and the linear-decay (lD) approach, for both parameter sets and deformation magnitudes, i.e. patients.

Table 6 depicts the mean relative residuals, as well as the standard deviation, of the investigated soft-tissue landmarks. The constraint-based approach results in smaller mean residuals and standard deviation for both parameter sets. Overall, a small deterioration of the mean residuals is observed upon the introduction of rotational degrees of freedom (compare Tab. 4). In this context, it should be noted that none of the landmarks is located in the regions of influence of humeri or scapulae, so they do not represent those regions, where the introduction of rotational degrees of freedom is expected to have the largest effect.

	stiff		elastic	
relative residuals	constr. based	decayConst	constr. based	decayConst
mean	0.78	0.81	0.88	0.89
std	0.33	0.34	0.26	0.29

Table 6.: Comparison of the mean relative residuals and standard deviation for the constraint-based (cB) and the linear-decay (lD) approach, for both parameter sets and patient 1.

Summary The two presented approaches for the introduction of rotational degrees of freedom show very different deformation results. As already observed during the conceptual model development (Sec. 5.3), the orientations do not decay isotropically for the constraint-based approach. This can result in grid folding within the individual regions of influence, as observed e.g. for the humerus and scapula. Especially for the large-range deformation this results in large DVF irregularities, as well as strong image artifact.
With the linear-decay approach, a uniform decay of the orientations is introduced, which prevents the grid folding observed for the constraint-based approach. For the small- as well as the large-range deformation, this results in a large improvement of the biofidelity of the deformation results since grid folding only occurs at the borderlines between the different regions of influence. These remaining irregularities will be addressed in the next section.
The characteristic values of the Jacobian distributions also reflect the superiority of the linear-decay approach over the constraint-based approach. The only value that became worse for the

linear-decay approach is J_{max}. However, the observed extreme Jacobian values only occur at very few locations, so they have only a small influence on the overall deformation.
The observations show, that including rotational degrees of freedom strongly improves the biofidelity of the DVF for both patients and parameter sets.

6.1.4. Multiple Initiators

In the previous sections, multiple initiators were handled by the approach of prioritization, which was explained in Sec. 5.4.1. As a result, sharp boundaries were observed between the regions of influence of the individual bones. These boundaries are located at those positions, which are reached after equal propagation times by paths originating from different initiators (Sec. 6.1.2). Therefore, the boundaries inherently have the width of one voxel, although they sometimes the visualizations by Jacobian maps show a broader boundary width, if the grid folding is extreme. In the following, the deformation results for the superposition approach presented in Sec. 5.4.2 are investigated, with the focus on the influence of different weightings of local versus global information (α, Eq. 5.7). For the processing order, a sorting by timestamps is used and the rotational degrees of freedom are handled by the linear-decay approach.

Figure 33 illustrates the deformation results for different weightings of local versus global deformation behavior for the small deformation magnitude, represented by patient 1, and for the elastic parameter set. For a global weighting function (upper row), hardly any DVF irregularities are observed at the borderlines between the regions of influence, neither in the DVF itself (first column) nor in the corresponding Jacobian map (second column), as indicated by box 1 for an exemplary borderline. However, these irregularities are not completely resolved, but shifted to the bones surfaces, as exemplary illustrated by box 2. The irregularities at the bone surfaces are similar to those irregularities observed for the processing order based on constraint-violation (compare Fig. 28b). For an intermediate weighting function (Fig. 33, middle row), the DVF irregularities at the bone surfaces are strongly reduced, while the borderline irregularities are still not as prominent as they are for the prioritization approach. For a local weighting function (Fig. 33, lower row) the large grid irregularities at the bone surfaces are resolved. However, the borderline irregularities between the individual regions of influence become more prominent. They do not appear as a distinct, narrow line, as was observed for the prioritization approach, but are distributed over a larger area (compare Fig. 31h and Fig. 33h, box 1). Compared to the prioritization approach, many DVF irregularities are resolved (compare Fig. 31h). This is most prominent at the soft-tissue borderline between humerus and scapula and in the region marked by arrow 7 (Fig. 33h).
The artificially deformed images (Fig. 33, third column) reflect the boundary irregularities observed in the Jacobian maps. For the global weighting, image artifacts like soft tissue being folded over the bones, or disrupted bones are visible (Fig. 33c, arrows 3 and 4). For the intermediate weighting, grid folding is still observed, especially at the frontal edge of the humerus, but the bones themselves are resampled correctly (Fig. 33f). For the local weighting, even the frontal edge of the humerus is resampled correctly (Fig. 33i). Remaining image artifacts are the extreme compression of the fatty tissue at the patient surface and the soft tissue spreading into the lung. Based on the visual evaluation, the weighting by $\alpha = t^{-4}$ achieves the best results. For the stiff parameter sets, the results are similar to those illustrated for the elastic parameter set.

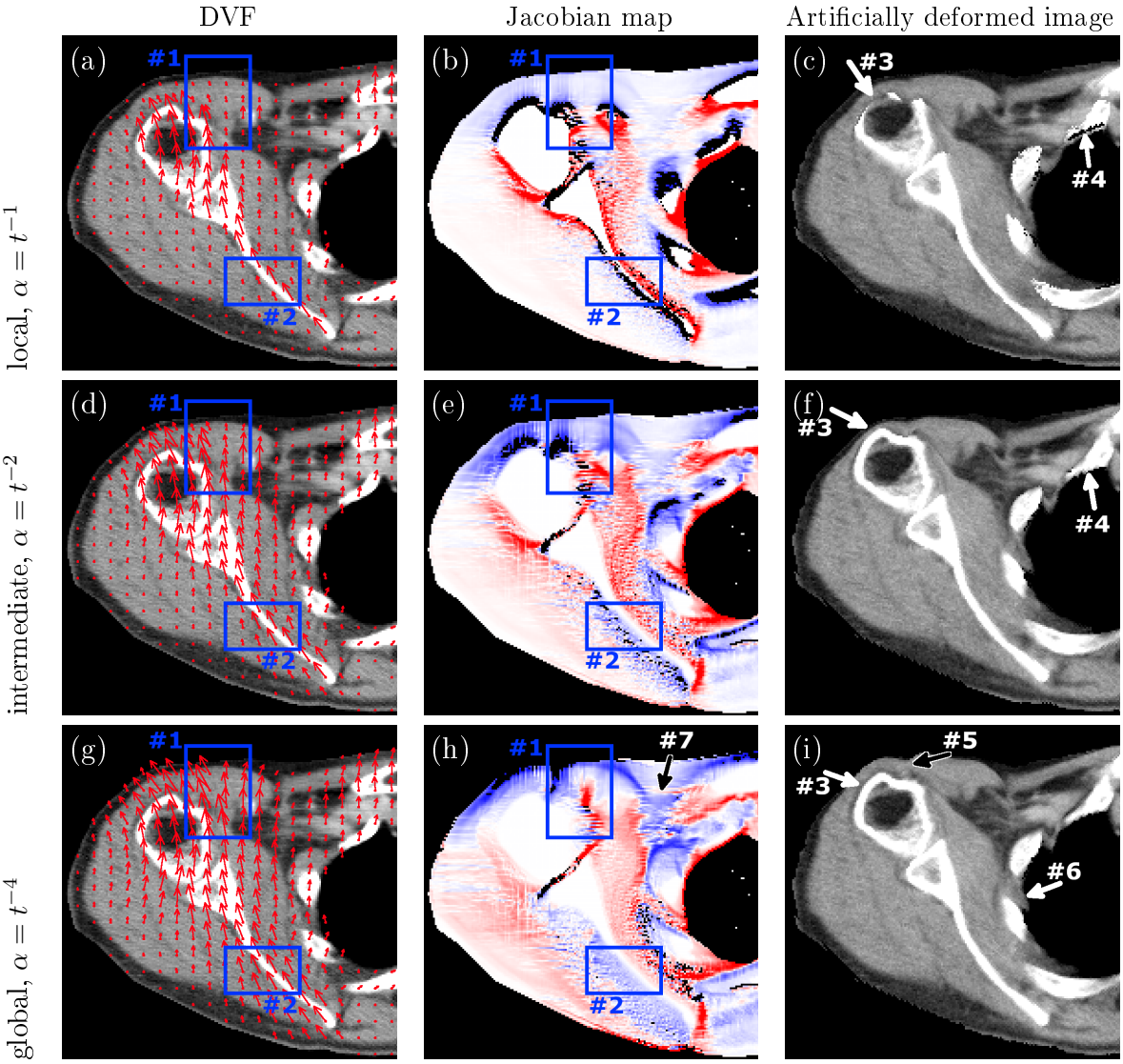

Figure 33.: Illustration of the influence of different weightings of local versus global information on the deformation results, for patient 1 and the elastic parameter set. For a weighting by $\alpha = t^{-1}$ (upper row), by $\alpha = t^{-2}$ (middle row) and by $\alpha = t^{-4}$ (lower row), the DVF overlayed on the planning CT (first column), the Jacobian map (second column) and the artificially deformed images (third column) are shown. Box 1 illustrates the deformation behavior of borderline irregularities with the different weightings, box 2 the deformation behavior at initiator, i.e. bone surfaces. Arrows 3 and 4 mark image artifacts, an area of soft-tissue folding, and respectively a disrupted bone. Arrow 5 marks an extreme compression of fatty tissue, arrow 6 soft tissue, being folded into the lung. Arrow 7 marks an area, in which DVF irregularities are resolved, compared to the prioritization approach (compare Fig. 31h).

Figure 34 illustrates the deformation results for different weights of local versus global deformation for the large deformation magnitude, represented by patient 2, and for the stiff parameter set. Similarly to the observations for patient 1, a global weighting (upper row) results in strong grid irregularities at the bone surfaces, as illustrated by the Jacobian maps (first and second column). With increasing weights for local deformations, these irregularities are shifted back to the locations of the borderlines between the regions of influence (middle and lower row). However,

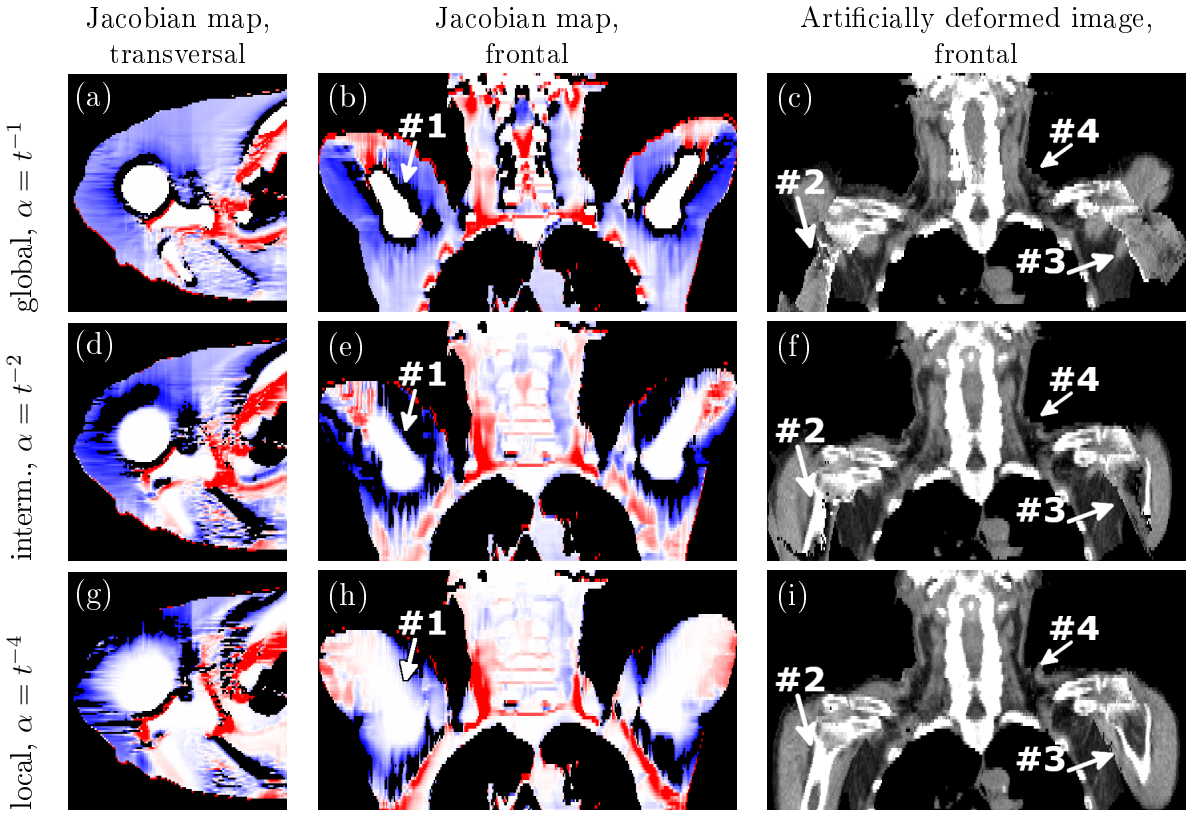

Figure 34.: Illustration of the influence of different weightings of local versus global information on the deformation results for patient 2 and the stiff parameter set. For a weighting by $\alpha = t^{-1}$ (upper row), by $\alpha = t^{-2}$ (middle row) and by $\alpha = t^{-4}$ (lower row), the Jacobian map of a transversal slice (first column) and a frontal slice (second column), as well as a frontal slice of the artificially deformed images (third column) are shown. Arrow 1 marks the development of grid irregularities at the humerus surface with different weighting functions. Arrow 2 marks the improvements in the resampled images for the bone appearance. Arrow 3 marks an area where the soft tissue of the arm is folded onto the thorax, arrow 4 image artifacts in the shoulder region.

even for a local weighting function, the boundary irregularities, extend over an area, which is broader than only a few voxels (compare lower row to Fig. 32e).
The resampled images (Fig. 34, third column) show even stronger image artifacts than were observed for patient 1. Only for the most local weighting function, these artifacts are resolved to an extent, at which the arms are completely resampled, without strong tissue distortions. Even for the local weighting function, grid folding is observed in the area, where the lowered arms approach the thorax (Fig. 34i). Compared to the prioritization approach, the image artifacts in the shoulder region have improved (compare Fig. 32i).

Table 7 compares the characteristic values of the Jacobian distributions for the different weightings, the different parameter sets and for both patients. In general, the intermediate ($\alpha = t^{-2}$) and local weighting ($\alpha = t^{-4}$) result in lower characteristic values than the global weighting, for both patients and parameter sets. Comparing the stiff and the elastic parameter set, for patient 1 not large differences are observed. For patient 2, the stiff parameter sets yields lower percentages of grid folding, but slightly higher mean and maximum Jacobians, compared to the elastic parameter set.

Comparing the characteristic values to those for the prioritization approach (Tab. 5), the values have improved for patient 1. Especially the percentage of voxels showing grid folding and the value of J_{max} strongly decreased. For patient 2, the introduction of deformation superposition results in an increase of $J_{<0}$, $J_{>2}$ and $J_{<0.5}$. However, the maximum Jacobians are reduced by more than 80% compared to the prioritization approach, and mean Jacobian decreased by more than 0.1.

	patient 1						patient 2					
	stiff			elastic			stiff			elastic		
char. values	t^{-1}	t^{-2}	t^{-4}	t^{-1}	t^{-2}	t^{-4}	t^{-1}	t^{-2}	t^{-4}	t^{-1}	t^{-2}	t^{-4}
$J_{<0}$ [%]	5.9	4.0	4.2	6.1	3.5	2.4	15.4	15.5	12.7	15.6	19.8	13.1
$J_{>2}$[%]	1.8	0.9	1.0	2.8	1.5	1.1	5.0	3.6	4.3	4.9	3.8	4.1
$J_{<0.5}$ [%]	2.0	2.6	1.8	1.6	4.5	4.6	7.4	8.8	5.5	7.0	9.2	6.5
$J_{\varnothing}$	1.03	0.995	0.999	1.05	1.007	0.992	1.10	1.09	1.15	1.08	1.07	1.13
J_{max}	7	7	10	7	7	8	118	75	57	79	50	53

Table 7.: Comparison of the characteristic values for the Jacobian distributions of differently weighted deformation superposition, different parameter sets and deformation magnitudes, i.e. patients.

Table 8 depicts the mean relative residuals, as well as the standard deviation of the investigated soft-tissue landmarks. For both parameter sets, the mean residuals decrease with increasing locality of the superposition weight, while the standard deviations increase.

	stiff			elastic		
relative residuals	t^{-1}	t^{-2}	t^{-4}	t^{-1}	t^{-2}	t^{-4}
mean	0.80	0.77	0.76	0.95	0.92	0.88
std	0.17	0.25	0.30	0.08	0.19	0.25

Table 8.: Comparison of the mean relative residuals and standard deviation for differently weighted deformation superposition and different parameter sets for patient 1.

Summary In the superposition approach, each initiator propagates its deformation through the whole volume, without initially being restricted to a certain region of influence. The weighting function determines how large the effective region of influence is, in which the respective deformation information actually contributes to the final DVF. The results show that the weighting function regulates the influence of local versus global deformation behavior. For a strong global deformation behavior, DVF irregularities occur at the initiator surfaces. For a very local deformation behavior, the deformations show grid irregularities at sharp borderlines, similar to the one observed in the prioritization approach.

The characteristic values of the Jacobian distributions reflect the decreasing occurrence of grid folding with an increasing locality of the weighting function. Compared to the prioritization approach, $J_{<0}$ and J_{max} have strongly decreased for $\alpha = t^{-4}$ in patient 1. The deformation superposition redistributes the conflicting information at borderlines between regions of interest, which were observed for the prioritization approach, over a larger area and thereby resolves many DVF irregularities. For patient 2, the percentage of voxels showing grid folding increases upon the introduction of superposition. The reason for this is, that the overall DVF irregularities are

larger than for patient 1 so that even the redistribution cannot completely resolve them. It only distributes the irregularities over a larger area, with the result that a larger absolute number of voxels is affected by grid folding. However, also for patient 2 a strong decrease in J_{max} is observed, which further results in a mean Jacobian much closer to 1.

All in all, the biofidelity of the DVF further improves by the introduction of information exchange between the different regions of influence. However, those weighting functions performing best concerning the DVF biofidelity, achieve the worse values concerning the model accuracy.

6.1.5. Initiating Structures

As shown in Sec. 5.5, deformation initiation by complex geometric structures results in grid irregularities. In this work, a concept to consider an adjustment of the processing order along the individual wave-fronts is developed to resolve the observed grid irregularities. On the level of basic shapes, obvious grid artifacts are resolved.
The transfer of the proposed concept to real patient data, however, showed no overall improvement. The DVF irregularities at borderlines between the different regions of influence even increased. This shows that the developed concept will have to be refined in order to apply it to the complex human anatomy. A starting point for the refinement could be to increase the level of deformation exchange along the wave fronts. This would further improve the grid regularity for cases similar to the U-shape (Fig. 24), for which sharp borderlines with potentially conflictive information occur. Moreover, the weighting of deformations along the wave front could be further investigated. However, it has to be considered that further refinements will also increase the computation times.

6.1.6. Computation Times

Table 9 depicts the computation times for the relevant model stages, for both patients and parameter sets. They are obtained by single-threaded processing on an IntelCore i7-5690@3.00 GHz processor. The computation times are in the order of 30 s for the prioritization approach.

	timing [min]			
model feature	patient 1		patient 2	
	stiff	elastic	stiff	elastic
original chainmail version	0:31	0:27	–	0:20
processing order by timestamps	0:27	0:24	0:15	0:14
rotational dof by the linear-decay approach	0:29	0:28	0:34	0:32
superposition with $\alpha = t^{-4}$	46:54	45:19	19:20	19:56

Table 9.: Computation times [min] for deformation modeling at the different stages of model development for both patients and parameter sets.

The introduction of timestamp-propagation slightly decreases the computation times compared to the original version of the enhanced chainmail algorithm, while the introduction of the linear-decay approach increased computation time again. For patient 2, the computation times are even doubled by the introduction of rotational degrees of freedom. The introduction of the superposition approach results in the largest increase in computation times to the order of 30 min, due to the sequential calculation of the individual initiators propagating through the whole

volume (Sec. 5.4). The stiff parameter set results in slightly larger computation times than the elastic parameter set, and the data set of patient 1 which contains a larger overall number of voxels, shows larger computation times at all model stages, except for the introduction of rotational degrees of freedom.

6.1.7. Summary

In complex human anatomies, a processing order based on timestamps has proven to be superior to a processing order based on constraint violation. The introduction of rotational degrees of freedom, which was introduced into the CM-concept for the first time, strongly improved the deformation behavior. All grid irregularities, except for those resulting from the conflicts between multiple initiating information, are resolved by the linear-decay approach. And finally, for the first time an approach for deformation superposition was introduced into the CM-concept. This further improved the regularity of the deformation grid. The final soft-tissue model is composed of a processing order by timestamps, rotation handling by the linear-decay approach and by deformation superposition with a weighting function with $\alpha = t^{-4}$. For the parameterization, the rigid parameter set is chosen.

6.2. Model Application

In the following, the final version of the soft-tissue model, which was derived in the previous section, is applied in the context of image registration and for forward deformations. The required input are the bone segmentations, as well as the initial translation and rotation of each bone which are derived from a kinematic skeleton for the bones (Sec. 4.2.1). For the first application the model input is derived from a registration of the bones, for the second application the input is created by artificial forward deformations of the skeleton.

6.2.1. Image Registration

In this subsection, the parameter for the bone transformations are obtained from a biomechanical image registration with the kinematic model for the skeleton. Based on this, the soft-tissue deformations are forwardly propagated by the developed deformation model. The resulting artificially deformed images are compared to the target images (fraction or post-treatment CT), which were used to derive the model input.

Figure 35 illustrates the deformation that has taken place between the original and the fraction CT based on a transversal slice of patient 1. The deformation is further illustrated by a fusion view of the two images (Fig. 35b). The artificially deformed image resulting from the soft-tissue deformation modeling, is illustrated by an analogous fusion view (Fig. 35d). The latter fusion shows that bones are rigidly transformed and match the positions of the bones in the fraction CT. A small misalignment is observed for a vessel at the left front of the patient. The largest misalignment is observed at the patient's surface and especially distal to the humerus and scapula. Here the model did not align the shape changes in the muscle and the resulting large change in the patient outline.
All in all, the soft-tissue is very well aligned, especially in the light of the fact, that no optimization of soft-tissue deformations has taken place. The presented results are achieved with the bone

transformations as the only input. The deviations in the surface regions are expected to be further improved by additional model input from the patient outline. Since the results are already close to the actual target image, a full registration, considering the optimization of soft-tissue deformation behavior, promises to achieve even better results.

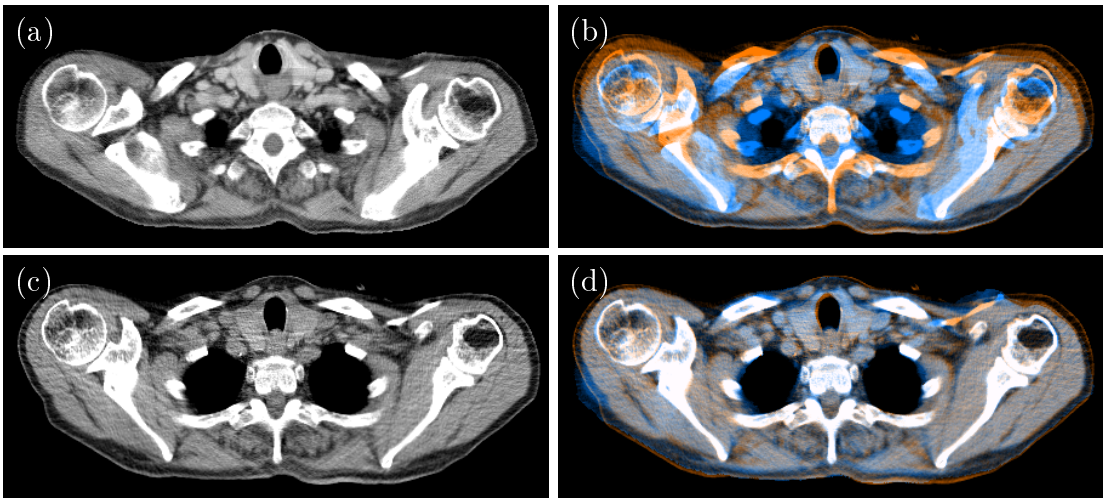

Figure 35.: Illustration of the deformation results of the final CM-version for patient 1. (a) Planning CT. (b) Fusion of planning CT (blue) and fraction CT (orange). (c) Fraction CT. (d) Fusion of the artificially deformed image (blue) and the fraction CT (orange).

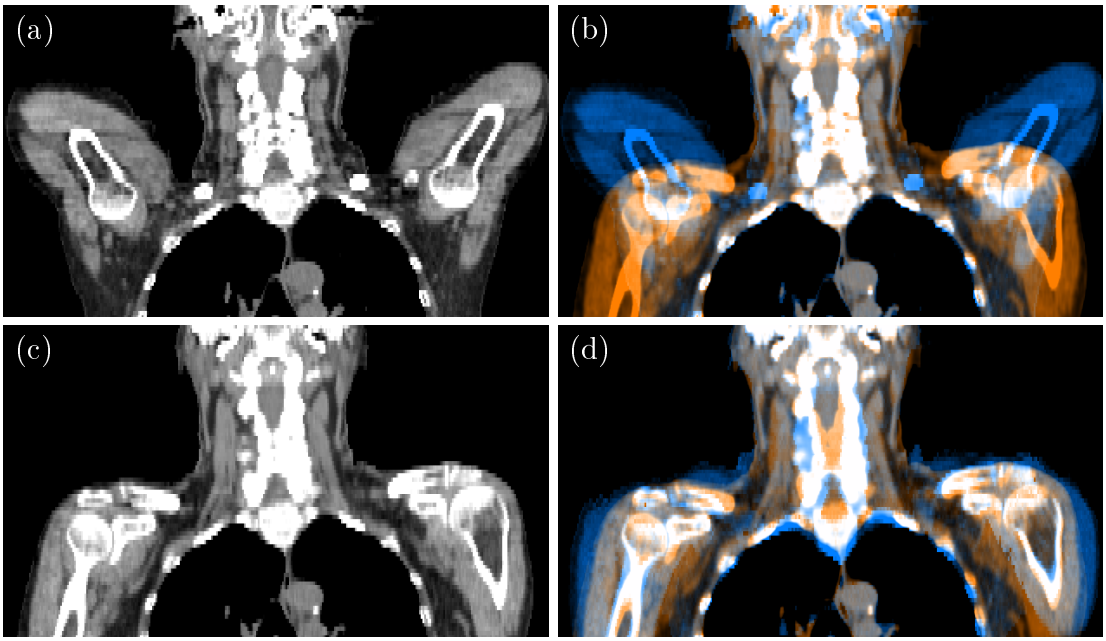

Figure 36.: Illustration of the deformation results of the final CM-version for patient 2. (a) Planning CT. (b) Fusion of planning CT (blue) and post-treatment CT (orange). (c) Fraction CT. (d) Fusion of the artificially deformed image (blue) and the post-treatment CT (orange).

Figure 36 illustrates the deformation that has taken place between the pre- and post-treatment CT of patient 2, based on an exemplary frontal slice. A fusion view (Fig. 36b) further illustrates the deformation range. The artificially deformed CT is illustrated in an analogous fusion view of the artificial and the fraction CT (Fig. 36d). For this large-range deformation, the focus is not

on the soft-tissue details, as for patient 1, but on the approximation of the overall final posture. The positions of the bones are not perfectly matched, but in the light of the extreme range of the deformation, this result is better than for most existing state-of-the-art models. The soft-tissue follows the bony deformations. Especially in the regions of the arms, which show an extreme rotation, this is remarkable, since no deformation input, except for the bones themselves is used. The deformation is solely based on the inherent connectivity of the CM-grid.
Deviations from the target image are observed mainly at the surface of the arms and in the shoulder region. These deviations are expected to be resolved by using the patient outline as additional deformation input.

6.2.2. Artificially Created Postures

In this subsection, the soft-tissue deformation model is used to model a shoulder elevation as an exemplary artificially created posture. To obtain the model input, the kinematic model

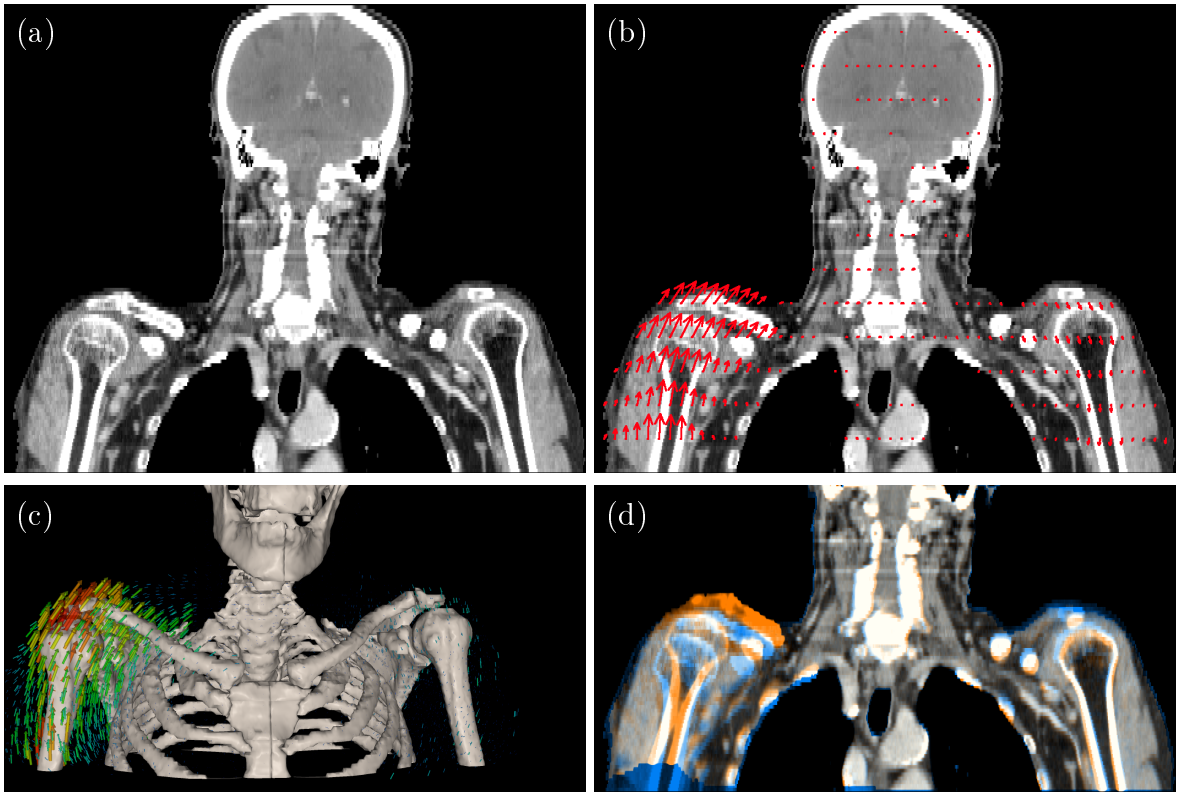

Figure 37.: Illustration of an artificial posture creation. Based on the planning CT (a), the kinematic model is set up. An artificial elevation of the right shoulder and arm is propagated into the soft-tissue, as illustrated by the 2D-DVF overlayed on the planning CT (b) and by the 3D-DVF, overlayed over a visualization of the kinematic skeleton model (c). The artificially deformed CT is shown as an image fusion with the planning CT (blue) (d).

(Sec. 4.2.1) is set up based on the planning CT of patient 1 and then manually manipulated to describe a shoulder elevation. The transformation parameter of the bones are propagated into the soft-tissue by the developed deformation model, the resulting DVF is depicted in Fig. 37b and c). From this, an artificial CT, mimicking the created posture is created as illustrated in the fusion view depicted in Fig. 37d. In this way, a variety of postures, describing deformations

typically occurring during radiotherapy can be reproduced based on the patient-specific planning CT.

6.3. Comparison to State-Of-The-Art Image-Based Models

In this section, the developed soft-tissue model is compared to the deformation results of two exemplary state-of-the art models used in the clinic, concerning the biofidelity of the deformations. For both models, the model input was approximated to be as similar to the input of the soft-tissue model as possible.

6.3.1. Thin-Plate-Splines

For the small-range deformation of patient 1, the deformation results of the soft-tissue model are compared to the deformation results of a thin-plate-splines (TPS) deformation. For both models, the final DVF has a resolution on voxel-level. The TPS requires computation times in the order of 10 s, the soft-tissue model in the order of 45 min, however, with the option to reach computation times of approximately 30 s by simple code parallelization. The model input for the TPS deformation (Sec. 4.2.3) is chosen as equivalent to the input of the soft-tissue model as possible, by approximating the bone deformations by 5 landmarks each. The landmarks transformations are derived from the same biomechanical registration of the skeleton, which also provide the input for the CM-model.
Figure 38 illustrates the deformation results for the TPS (upper) and soft-tissue model (lower). The TPS deformation is, in general, much stiffer than the deformation of the developed soft-tissue model as illustrated by the DVFs and the Jacobian maps. However, the DVF of the TPS is not confined to the patient, but also extends into the surrounding air and into the lung where no real deformations take place. In general, the volume changes of the individual voxels are much smaller for the TPS-deformation. This is reflected by the width of the Jacobian distribution, which is much smaller than for the soft-tissue deformation model. In the Jacobian map (Fig. 38b) hardly any color gradients are observed. The Jacobian map with a decreased width of the color-scale (Fig. 38b, inlay), however, illustrates that the strains within the Jacobian map do not reflect the underlying anatomy. Despite the use of rigidly transformed bony landmarks for the model input, the bones are not volume conserving. The soft-tissue deformation model does conserve the volume of all bones, but shows unrealistic DVF irregularities in soft-tissue regions.
Finally, in the artificially resampled images (Fig. 38, third column), the soft-tissue deformation model aligns tissue artifacts better than the TPS-deformation. Especially at the patient surface, the TPS over- or undershoots, resulting in a clear mismatch of the frontal and dorsal patient outline. In distal direction, both deformation models result in misalignment.
Table 10 compares the characteristic values of the Jacobian distributions for the two models. The characteristic values for the TPS reflect the narrow Jacobian distribution, which was also illustrated in the Jacobian maps. There are no extreme volume changes, $J_{<0.5}$ and $J_{>2}$ are both 0. Moreover, the TPS distribution shows no grid folding at all.
Table 11 compares the mean relative residuals of the exemplary soft-tissue landmark set. The TPS achieves a lower accuracy than the soft-tissue model, however, with both accuracies being rather low, resulting in mean residuals above 0.75. For similar input information, the soft-tissue model achieves a better biofidelity of the deformation results, mainly due to its ability to consider the information of tissue heterogeneity.

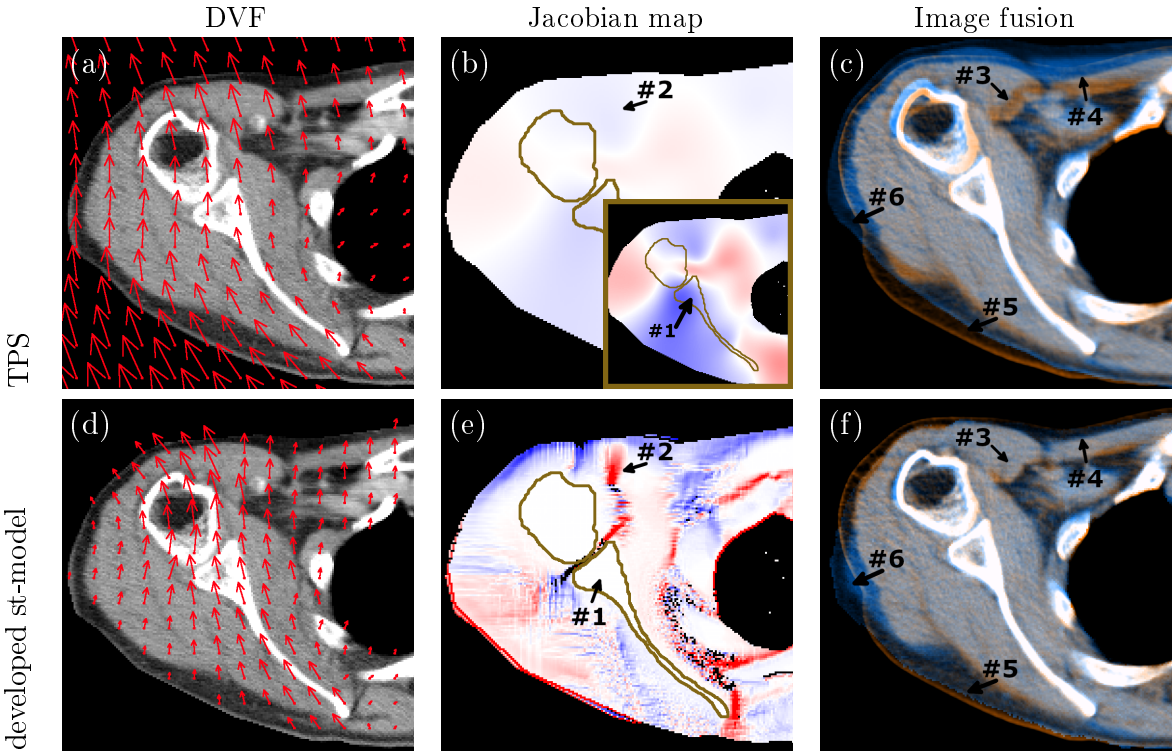

Figure 38.: Comparison of the deformation results for the thin-plate splines (upper, row) and the final version of the developed soft-tissue model (lower row), for patient 1. For both models, the DVF overlayed on the planning CT (first column), the corresponding Jacobian maps (second column), as well as the artificially deformed images(third column) are shown. The inlay in (b) shows the same Jacobian map, but with the width of the color-scale narrowed to one fourth of the original scale. Arrow 1 marks the Jacobian values within bones, which are not volume conserving for the TPS. Arrow 2 marks borderline irregularities, which only occur in the developed soft-tissue model. Arrow 3 marks areas in which the soft-tissue alignment is improved, arrows 3 and 4 areas, in which the deformation of the patient outline is improved, by the developed soft-tissue model. Arrow 6 marks misalignment of the patient outline, which occurs in both models.

char. values	TPS	st-model
$J_{<0}$ [%]	0	4.2
$J_{>2}$ [%]	0	1.0
$J_{<0.5}$ [%]	0	1.8
$J_{\varnothing}$	1.0003	0.999
J_{max}	1.4	10

Table 10.: Characteristic values for the Jacobian distribution for the TPS and the soft-tissue deformation model.

relative residuals	TPS	st-model
mean	0.81	0.76
std	0.50	0.30

Table 11.: Comparison of the mean relative residuals and standard deviation for the TPS and the soft-tissue model.

6.3.2. ANACONDA-algorithm

For the large-range deformation of patient 2, the deformation results of the soft-tissue model are compared to the results of the hybrid ANACONDA-algorithm (Sec. 4.2.4), implemented into the RayStation planning system. Since the functionality to export the DVF from the RayStation

was not available, no analysis of the Jacobian values is executed. The computation times for the ANACONDA-algorithm were >1 h, the computation times of the soft-tissue model approximately 20 min with the potential to decrease the times to about 30 s by simple parallelization.
In contrast to the developed soft-tissue model, the ANACONDA algorithm actually performs an image registration, optimizing the deformation results not only in the bones, but also in the soft-tissue regions. The model input used for the ANACONDA-registration algorithm are the image information of the planning CT and the post-treatment CT, as well as the segmentations of the patient outline, the skull and the right and left humerus and scapula, which were used as controlling ROIs. To produce a similar input for the soft-tissue model, the bone registration was based on only three landmarks each on the skull, humeri and scapulae [89]. Based on these landmarks, the kinematic model determined the transformations of all bones. The patient outline was not used as input, since the transformation parameter for the outline were not available.
Figure 39 compares the results for the ANACONDA-algorithm and the soft-tissue deformation model, based on the artificially deformed images. The image-based ANACONDA-algorithm deforms the bones, especially the humeri, although they were used as controlling ROIs. Such a deformation of rigid bones is a clear feature of physically implausible deformations. With the soft-tissue model all bones are rigidly deformed.
Regarding the soft-tissue details, they are aligned more correctly with the ANACONDA-algorithm, due to the applied registration. However, similarly as observed for the bones, the overall deformation in the shoulder region is distorted. The artificially deformed image looks similar to the post-treatment CT, but the overall deformation is not anatomically reasonable. Such deformation results are typical for image-based deformation models. With the soft-tissue model, no image distortions occur, due to the explicit consideration of tissue heterogeneity. However, in contrast to the results for the ANACONDA algorithm, in the shoulder region at the patient surface, as well as in the regions where the arms touch the thorax, image artifacts are observed. These can mainly be attributed to the missing information of the patient outline as explained in more detail in Sec. 6.1.4.

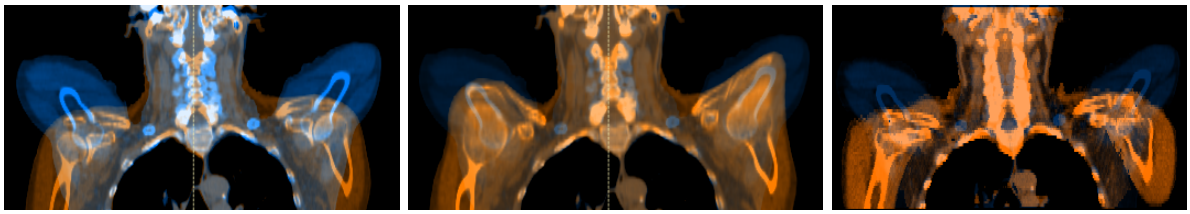

Figure 39.: Comparison of the deformation results for the ANACONDA-algorithm and the final version of the developed soft-tissue model for patient 2. A fusion view of the post-treatment CT in orange and in blue the (a) planning CT, (b) ANACONDA-deformation result and (c) soft-tissue model deformation result are shown.

7. Discussion

7.1. Methods for Model Validation

From the large number of evaluation metrics that are available, in this work the focus is set to those which investigate the physical consistency and biofidelity of deformations. The reason for this choice is that the DVF consistency is a necessary condition for a physically plausible deformation method [43]. At each stage of model development, as well as for the final soft-tissue deformation model, the physical consistency is evaluated based on the visualization of artificially deformed images and DVFs, as well as based on the Jacobian distributions and Jacobian maps. The artificially deformed images are the basis for a visual evaluation of the deformation results. They are obtained by an image resampling method, which potentially influences the appearance of the deformed image. The chosen resampling method (Sec. 4.2.5) achieves a smooth resampling for topology-conserving DVFs, so resampling artifacts appear only in those regions in which grid folding occurs.
In regions with low tissue contrast, erroneous deformations cannot be detected based on artificially deformed images. If voxels showing grid folding or extreme volume changes are located in tissue without density gradients, the image grey values are simply interpolated by the image sampling method. This is observed e.g. in Fig. 28e,f where most DVF irregularities are located in homogeneous tissue and smoothed out during image resampling. In high-contrast regions, however, unphysical deformation behavior is directly recognized since it results in image artifacts like rigid structures being torn apart (Fig. 28c), muscular tissue being disrupted (Fig. 32c) or soft tissue spreading into the lung (Fig. 31i).
The DVFs are visualized by projecting the 3D vectorfields to 2D slices. Although the 2D-projections complicate the interpretation of the DVFs, large irregularities can easily be detected, even in regions with low tissue contrast (Fig. 31a). Small DVF irregularities, however, can usually not be identified by DVF visualizations.
A more detailed analysis of the DVF regularity is executed by a visualization of Jacobian maps. These maps depict the values of the Jacobian determinant for each individual image voxel. In this way, even small irregularities in the vectorfield can be detected (Fig. 31b). Moreover, Jacobian maps picture the Jacobian values in the anatomical context. This is important for judging the biofidelity of deformation results. Usually, the occurrence of voxels showing grid folding is interpreted as a clear indicator for an inconsistent DVF. However, in some anatomical sites, observed grid folding can be anatomically reasonable, e.g. if it results from sliding motion. Therefore, the percentage of voxels showing grid folding alone does not indicate the biofidelity of a DVF, an interpretation in the anatomical context is required.
In addition to the local image-based evaluation of the DVF regularity, the global regularity is summarized by five characteristic values of the Jacobian distribution. These characteristic values allow a direct comparison of the DVF regularity for different deformations, as was used for comparing the deformation results at the different stages of model development. However, it has to be kept in mind that such global quantities average all local effects, and therefore give no information about local deformation behavior. All in all, the Jacobian values can indicate the absence of artifacts found in unphysical DVFs, but not the presence of realistic deformation behavior [41].

As an indicator for the model accuracy, a set of anatomical soft-tissue landmarks is used (Sec. 4.3.3). The definition of anatomical landmarks in soft-tissue is very challenging, espe-

cially for large-range deformations. Therefore, the landmark evaluation is executed only for the small-range deformation of patient 1, for which 16 landmarks were defined. Due to the limited number of landmarks, which are further limited to high-contrast regions, the results not reflect the overall model accuracy [47]. They are rather used as an indicator for estimating improvements in the accuracy at the different stages of model development.

In general, the lack of a gold-standard for evaluation of deformation models in human anatomies poses a large challenge to accurate model validation. In this work, the focus is set to the evaluation of DVF regularity by the Jacobian determinant, as well as to interpretation of the investigated DVF regularity in the anatomical context. For a comprehensive model validation, a combination of various evaluation metrics addressing DVF regularity as well as model accuracy is recommended [44]. Therefore, in future work additional evaluation metrics, especially for the model accuracy, should be assessed in detail. Since soft-tissue landmarks are difficult to define, DICE indices for soft-tissue structures like muscles as well as the comparison to physical phantoms are expected to provide a more comprehensive model validation. Finally, the requirements to model accuracy and DVF regularity always depend on the specific anatomical site and on the desired application. As indicated by the evaluation based on Jacobian maps, validation results should always be considered in the context of the underlying anatomy.

7.2. Model Concepts

In the course of this work, a soft-tissue deformation model for describing posture changes in the complex human anatomy was developed. To achieve a high biofidelity of the deformation results, as required for radiotherapy applications, various new concepts are introduced into the basic chainmail (CM)-approach. Two different processing orders were scrutinized for the deformation process. Additionally, two new methods for introducing rotational degrees of freedom into the model were developed. Instead of using a single point-correspondence as model input, the model was tailored to flexible anatomical input, as proven by coupling it to a kinematic skeleton model. To cope with the resulting multiple input structures, a concept for handling multiple initiators, as well as initiating structures was developed. Moreover, the model parameterization is adjusted to the application to patient CT-images.
In the following section, the newly introduced concepts are discussed concerning their influence on the biofidelity of the final deformation results. The evaluation of the model concepts is based on the deformation results for two exemplary patients representing a small-range and respectively large-range deformation. The applied evaluation methods were discussed in the previous section.

7.2.1. Model Input

As model input for the soft-tissue deformation model, the transformations of the skeletal bones are used. Taking the bone transformations as the input for soft-tissue deformation is standard in most state-of-the-art biomechanical models [34, 37–41]. For the developed soft-tissue model, the bone transformations are derived from a kinematic skeleton model, in order to provide an anatomical correct input. Still, in reality not all deformations in soft-tissue can be traced back solely to posture changes of the skeleton. Therefore, based on the limited input information, no perfect alignment of soft-tissue structures is expected for the final deformation results.
Further improvement of the deformation results is expected from additional model input. Other

state-of-the-art models additionally consider the displacements of the patient outline [34] or of the tumor outline [38]. Since the developed soft-tissue model implements input information on the level of voxel displacements, it is very flexible concerning possible input information. If available, information from patient or tumor outline could be implemented as well. In the future, also a coupling to radiation-response models for the tumor and for OARs, as well as the coupling to organ models e.g. for breathing motion, will allow a more comprehensive description of the global patient deformations.

7.2.2. Model Parameterization

In the CM-concept, the model elasticity is parameterized by geometric constraints limiting the compression, extension and shear of the links between neighboring CM-elements. There is no direct relation between the parameters of the CM-concept and actual physical parameters which describe the macroscopic deformation behavior. However, the resulting deformation behavior can be compared to the macroscopic parameters from continuum mechanics, like the Poisson's ratio and Young's modulus. When the initiating CM-element is displaced by Δx_e, this results in a stress $\sigma_e \propto \Delta x_e$, and induces a strain ε_n in the neighboring CM-elements. The induced strain is equivalent to the deviation between the final position of the neighboring CM-element and the midpoint of the respective valid region (Fig. 40a).

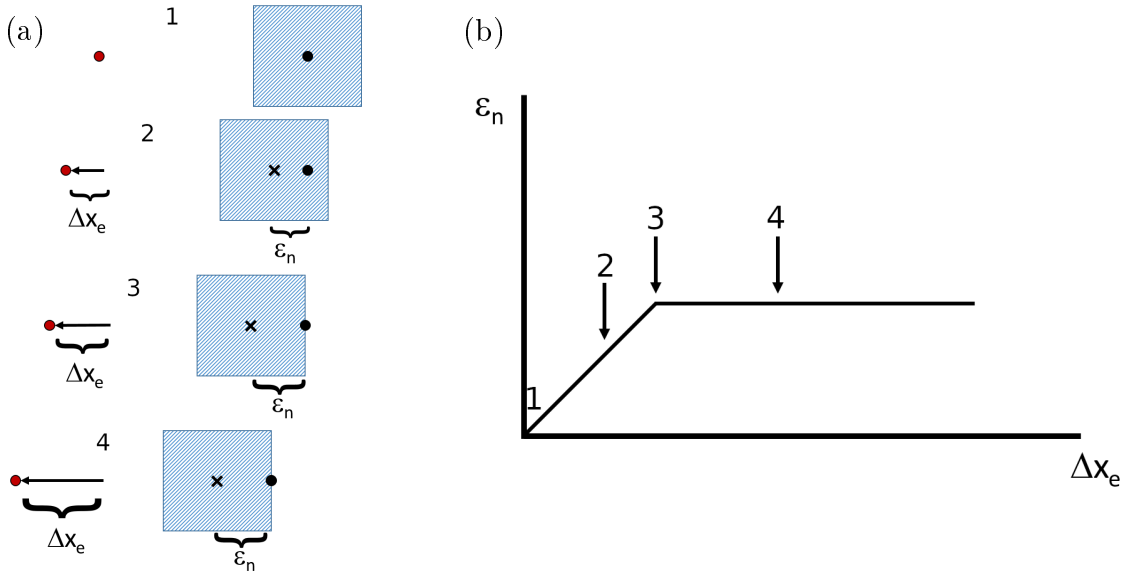

Figure 40.: (a) Illustration of the definition of strain (ε) in the CM-concept. The displacement Δx_e of the initial CM-element shifts the valid regions for the neighboring CM-elements. This results in a deviation between the mid-point of the valid region to the actual position of the neighboring CM-element. This deviation is equivalent to the strain of the neighboring CM-element (ε). (b) Illustration of the stress-strain relationship in the CM-concept. The arrows mark the different scenarios illustrated in (a).

The resulting relationship between stress and strain is linear for small displacements (Fig. 40b). This is the same behavior as described in continuum mechanics by Young's modulus Y for the linear elastic regime (Eq. 2.5). For large displacements, for which neighboring CM-elements do not stay in the respective valid regions (Fig. 40a,4), the resulting strain remains constant

(Fig 40b). In this non-linear regime, Y linearly increases with increasing stress, i.e. with initial displacements.
In the CM-concept, the geometric constraints are evaluated independently for the different directions. The strain resulting from compression or extension of a link has no influence on the perpendicular shear strain. In continuum mechanics, Poisson's ratio (Eq. 2.6) describes the response of tissue in direction orthogonal to stress application. For considering this behavior within in CM-concept, a coupling between the different directions would have to be introduced. However, the simple definition of the valid regions and the independent evaluation of constraints into different directions is the computationally fastest approach. Therefore, the benefit of a more complex definition of the geometric constraints will have to be weighted against the draw-back of increasing computation times.
The particular values for the geometric constraints are assigned by a material transfer function, which maps the HU-values of the underlying CT images to the constraint values of the individual CM-elements. This function distinguishes between three different tissue types, which are bones, elastic tissue, and air. Within the category of elastic tissue, varying elasticity is further approximated by linearly interpolating the values for the geometric constraints over the respective range of HU-values. Refinements of the material transfer functions, as presented e.g. by Rodriguez et al. [11], might improve the deformation results. For physical phantoms, it was shown that the consideration of three soft-tissue types is sufficient [90]. Most state-of-the-art biomechanical models also use only 2-3 different tissue types [38, 41], without further refinement within the individual tissue categories.
The presented material transfer functions are tailored to CT-images. However, such functions can also be introduced for MR images as presented e.g. by Rodriguez et al. [11]. The challenge for MR images as well as for CT images of other anatomical sites like the thorax is that materials with different elasticity are represented by identical grey values. In such cases additional input, e.g. from tissue and organ segmentation, might be required for a proper model parameterization.
Other methods used for assigning tissue properties to a biomechanical model are manual and (semi-)automatic tissue segmentation. Manual tissue segmentation still is one of the most commonly used methods [38, 40], although it is very time-consuming. A method for semi-automatic tissue classification is the Fuzzy C-Means algorithm [91, 92]. Automatic segmentation is also applied for specific applications [41], but in general still is a field of research.
The final parameterization of the soft-tissue deformation model is determined empirically. During model development, the influence of different parameterizations was investigated by comparing the deformation results for a stiff and an elastic parameter set for the elastic tissue category. In general, it is not possible to exactly determine in-vivo material properties. Methods like MR-elastography, in principle, allow for the experimental determination of tissue elasticity [93], however they are very resource-intensive and not applicable in vivo.
In the presented model the final model parameterization is globally defined. A local parameter optimization, similarly as used for mass-spring-models (Sec. 2.2.3), is expected to further improve the deformation behavior. For radiotherapy applications, the decision for a certain parameter set should, in general, be based on the anatomical site and the specific application.

7.2.3. Processing Order

The general idea to adjust the processing order of CM-elements for improving the deformation behavior of heterogeneous tissue, was introduced by Schill [10]. He stated that deformations have to travel faster through stiff tissue to ensure a realistic deformation behavior, e.g. rigid

structures not being torn apart. In this context, he introduced the constraint-violation as a sorting criterion for the CM-algorithm, assuming that the path of largest constraint violation is identical to the path of largest material stiffness (Sec. 2.4). However, the constraint violation simply prioritizes the largest displacements.
With the occurrence of multiple initiating structures and initial rotations, as required for modeling complex human anatomies, the largest displacements not necessarily correspond to the largest underlying material stiffness any more. Therefore, a processing order based on timestamps as proposed by Rodriguez et al. [11] was implemented. In this approach, a deformation propagates along the path of smallest traversal times. These traversal times solely depend on tissue stiffness as initially intended by Schill et al. [10]. In this way, the processing order is decoupled from the influences of multiple initiators and initial rotations, and a more regular propagation pattern was achieved.

The validation based on patient data showed that the DVF regularity improved upon the introduction of timestamps (Sec. 6.1.2). Only for the small-range deformation and the elastic parameter set, some additional DVF irregularities were observed (Fig. 28e). However, these irregularities were resolved with the introduction of subsequent model features like rotational degrees of freedom. Therefore, timestamps have shown to be the most favorable sorting criterion for an application of the CM-concept in complex human anatomies.

All in all, the introduction of timestamps has decoupled the processing order from all influences but the tissue heterogeneity, resulting in an improvement of the physical plausibility of the DVF for both patients and parameter sets. Therefore, the final soft-tissue deformation model uses timestamp-based deformation propagation.

7.2.4. Rotational Degrees of Freedom

In the original CM-concept, all initial displacements are interpreted as translations, which linearly decrease with increasing distance from the initiator (Sec.2.4). I, however, the initial displacements originate from initial rotations, this assumption does not hold any more. For rotations, not the displacement itself but the orientation, respectively rotation angle, decreases with increasing distance from the initiator. However, for different distances to the rotation point, identical rotation angles result in different absolute displacements. Therefore, depending on the exact location of the rotation point and the direction of deformation propagation, a decreasing rotation angle can even result in an increasing absolute displacement.

To address the conceptual problem described above, two approaches for handling rotational degrees of freedom were developed (Sec. 5.3). The validation based on patient data showed that the linear-decay approach is superior to the constraint-based approach (Sec. 6.1.3).
For the constraint-based approach, large areas of grid folding were observed (Fig. 31b, Fig. 32a,b), resulting from a non-isotropic decay of orientations. For the linear-decay approach, all local grid irregularities were resolved (Fig. 31e, Fig. 32d,e). Grid folding only occurred at the borderlines between regions influenced by different deformation initiators. This however, resulted from the introduction of multiple deformation initiators, and will be discussed in the next section. The superiority of the linear-decay approach was further reflected by the characteristic values of the Jacobian distributions (Tab. 5).
Compared to the previous model stage, at which no rotational degrees of freedom were considered, the landmark evaluation indicated a decreasing model accuracy (Tab. 6). However, due to the overall small number of landmarks, the validity of the accuracy evaluation is limited, especially

because none of the landmarks is located in proximity of humeri and scapulae, where the largest improvements are expected. The physical plausibility of the Jacobian distributions, as well as of the artificially deformed images, strongly improved upon the introduction of rotational degrees of freedom. Only for the large-range deformation, the artificially deformed images still showed obvious image artifacts in the shoulder region, located at the patient's surface (Fig. 32f,i). This is expected to be improved by additional model input, e.g. from the patient's outline.

The exact locations of rotation points are usually not known for the bones, so they were approximated by the bone centroids. A more physiological location for the rotation points would be the respective joints. However, shifting the rotation points to approximated joint positions had only a very low influence on the deformation results. Therefore, the influence of the rotation point does not seem to be as large as expected from the conceptual observations in Sec. 5.3. However, it should be kept in mind, that the location of the rotation point is a potential source of uncertainty that could show a larger effect e.g. in different anatomical sites.

All in all, the introduction of rotational degrees of freedom by the linear-decay approach strongly improved the physical plausibility of the DVF. The largest improvement is observed for the large-range deformation, which describes arm rotations of almost 180°. Therefore, rotational degrees of freedom were implemented into the final soft-tissue model by the linear-decay approach.

7.2.5. Multiple Initiators

As discussed in the previous sections, the local deformation behavior of the developed soft-tissue model has been improved by introducing a timestamp-based processing order and rotational degrees of freedom. However, in the complex human anatomy, not only local deformations but also global ones have to be described. Most existing CM-approaches use only single deformation initiators or do not offer sophisticated concepts for handling global deformations. In this work, a new concept for handling the input from multiple initiators, e.g.. all skeletal bones, was developed to approximate global deformation behavior.
In classical physics models like mass-spring models or continuum models, the model input consists of force and boundary conditions. Such physical models are defined by systems of differential equations. When solving these systems of equations, all forces and boundary conditions are balanced in order to obtain the final deformation.
In the CM-concept, the input information is based on displacements and orientations, which represent forces as well as boundary conditions. For multiple initiators, it has to be defined how far the deformation information of each initiator spreads into the surrounding CM-grid, and if and how information is exchanged between the different initiators.

For simple prioritization of the information from different initiators, which was also used by Rodriguez et al. [11], no information exchange between the initiators is considered. This results in sharp borderlines, separating the different regions of influence (Fig. 31e, Fig. 32e). Such sharp borderlines occurring in homogeneous tissue are not realistic, so this approach is not suitable for the desired radiotherapy applications. Therefore, an introduction of information exchange between the different initiators is required.
The developed concept for deformation superposition makes use of the analogy to sound waves, which was introduced by Schill et al. [10] in the context of the processing order (Sec. 5.4). The deformation waves sent out by all initiating bones are assumed to interfere with each other. The intensity of the deformation waves, is assumed to decrease with increasing distance from the initiator, as well as with increasing tissue stiffness along the deformation path. This behavior is

approximated by a timestamp-dependent weighting function. A similar superposition of DVFs by a weighted superposition was used by Gering et al. [42], however with a weighting by the Euclidean distance to the model initiators. In contrast to a timestamp-based weighting, the Euclidean distance neglects the influence of tissue stiffness.
The superposition acts as a kind of regularization, which transfers the local deformation behavior of the soft-tissue deformation model, to a global scale. An alternative, but much more complex approach for regularizing DVFs is proposed by Kracali et al. [94]. They developed a mathematical method to derive the closest topology preserving DVF for any DVF which shows grid folding. With regard to the requirement of low computation times, this method was not applied.

The validation based on patient data showed than an intermediate weighting yields the best results for the superposition (Sec. 6.1.4). A too global weighting function results in DVF irregularities and image artifacts at the bone surfaces (Fig. 33, upper row). A too local weighting function on the other hand, results in a deformation behavior similar to the prioritization approach (Fig. 33, lower row), going along with the draw-backs explained above.
Compared to the previous model stage, the Jacobian distributions, as well as the artificially deformed images, improved for the small-range deformation. For the large-range deformation, the overall percentage of voxels showing grid folding increased. The reason for this is that the information conflict between the multiple initiators was too large, to be resolved by the superposition. However, the appearance of the artificially deformed images showed less artifacts than without superposition, even for the large-range deformation.
The newly developed superposition approach does improve the overall regularity of the deformation grid, however, at the cost of dissolving the local deformation information. Especially for superposition in regions where initiating bones are located close to each other, like in the shoulder joint or between the scapula and the nearby ribs, even with the application of the superposition approach, grid folding is observed (Fig. 33, second column). In those regions most probably sliding motion occurs, e.g. due to the rotation of the humerus head in the socket, or due to a sliding of the scapula along the rib cage. This illustrates the importance of considering the anatomical context when evaluating and interpreting deformation results.
For all initiators the same weighting is used during superposition. In the future, it could be considered to introduce different weighting functions for different regions in the patient and treat e.g. those with sliding motion differently. However, this requires a more detailed analysis of tissue behavior in the different sites, first.
For large-range deformations, it is possible that areas which are not connected to each other are folded onto each other. This was for example observed for the arm being rotated onto the thorax (Fig. 34i). Since deformations are not propagated into the air surrounding the patient, no information exchange takes place between the arm and the thorax and collision detection is not possible. This shows, that especially for large-range deformations the patient outline is required as additional input. It will allow to detect such collisions and is the starting point to develop a solution for this problem.

The introduction of the superposition approach strongly increased the overall computation times for the soft-tissue model (Tab. 9). The reason for this is that the deformations of the individual initiators are propagated over a larger overall region of influence than at the previous model stages. Moreover, in the current implementation of the superposition approach, the initiators are processed sequentially, so that the deformation time multiplies approximately with the number of initiators. A simple parallelization of the sequential processing will achieve similar computation times as the prioritization approach, in the order of 30 s. With respect to the requirement of

low computation times for an application in adaptive radiotherapy, in future work, such a code parallelization should be implemented.

All in all, the introduction of information exchange between the different regions of influence further improved the biofidelity of the model results. However, those weighting functions performing best concerning the DVF biofidelity (Tab. 7) achieve the worse values concerning the model accuracy (Tab. 8). The introduction of additional model input is expected to increase the model accuracy while keeping the physically plausible deformation behavior. For the final soft-tissue deformation model, an intermediate weighting function with the weight $\alpha = t^{-4}$ is chosen.

7.2.6. Initiating Structures

In the existing CM-approaches, deformations are initialized by point-initiators. However, for the developed soft-tissue deformation model, anatomical structures like the bones are required for model input. Therefore, in this work a concept for handling the input information of anatomical structures was developed (Sec. 5.5).
In this concept, initiating structures are considered as collections of single initiating CM-elements. In the light of the results discussed for multiple initiators in the previous section, the deformation information of all CM-elements on a structure's surface should be combined by a weighted superposition. However, a superposition following the concept presented in the previous section, would be too time-consuming, especially for large structures. Therefore, a concept for exchanging deformation information along the individual wave fronts, already during the process of deformation propagation, is introduced. At the conceptual stage, the introduction of this concept did improve the regularity of the deformation results.

The validation based on patient data, however, showed no improvements (Sec. 6.1.5). On the contrary, the occurrence of grid irregularities and image artifacts increased. These observations showed, that a more detailed handling of information superposition is required, when applying the concept to the complex shapes occurring in real human anatomies.
Since the conceptual study clearly showed that the shapes of initiating structures influence the DVF regularity (Fig. 23-Fig. 25), further investigation of how to resolve the observed irregularities is required. Refinements of the developed concept should address an extension of the regions in which deformation superposition is executed. Moreover, the influence of the applied local weighting function (Eq. 5.8) should be investigated in more detail. Based on these results, in the final soft-tissue deformation model no information exchange along wave fronts is implemented.

7.3. Model Performance

The final version of the soft-tissue deformation model uses a timestamp-based processing order, considers rotational degrees of freedom by the newly introduced linear-decay approach, and considers information exchange between multiple deformation initiators by the developed superposition approach. For the weighting function of the superposition the weight $\alpha = \frac{1}{t^4}$ is used. For the applications to real patient data the stiff parameter set is used since it showed better overall results in the evaluation based on patient data.
In the following section, the model performance will be discussed concerning the achievable com-

putation times, concerning a comparison to state-of-the-art image-based deformation models, as well as concerning the capability of modeling different deformation ranges.

7.3.1. Computation Times

The computation time of the developed model, in general, depends on the number of CM-elements affected by the modeled deformation. Therefore, the size of the data set has a large influence on the computation time. The data set for patient 2 contains only about two third of the number of voxels of the data set for patient 1. In accordance with this, the computation times for patient 1 were observed to be much higher than for patient 2 (Tab. 9).
The number of affected CM-elements is expected to further depend on the stiffness of the parameterization, since the region into which a local deformation is propagated, increases with increasing tissue stiffness. The observations of the computation times confirm this dependence, however, the differences for the different parameterizations are low. It was shown that increasing the stiffness of the parameterization only makes a difference for those CM-elements which are located at the patient's surface (Fig. 31 middle vs lower row). These CM-elements make up only a small percentage of the overall number of CM-elements, so that only a small increase in the computation time is observed.
Furthermore, an increasing deformation magnitude is expected to increase the overall number of CM-elements affected by a deformation, and thereby the overall computation time. This relation could not directly be investigated, since the influence of the different sizes of the data sets on computation time was larger than the influence of the different deformation magnitudes. The increase of computation time is expected to be in a similar order as the increase due to increasing tissue stiffness, i.e. very low.
The developed soft-tissue model achieves low computation times in the order of 30 s at a high resolution in the order of the voxel sizes. Only for the superposition approach, the computation times strongly increase to approximately 45 min and 20 min for patient 1 and respectively patient 2. Due to the sequential processing of the individual initiators, the number of initiators has a strong influence of the computation times, for the superposition approach. For patient 1, 42 initiators and for patient 2, 32 initiators were used. This, in combination with the smaller overall number of CM-elements for patient 2, explains the much lower computation times for the data set of patient 2.
However, the superposition approach could easily be parallelized by processing all initiators at the same time. In this way, the influence of the number of initiators could be resolved and computation times could be reduced to the order of 30 s. Moreover, parallelization approaches for the general CM-concept exist [11, 78], which have the potential to further decrease the computation times. For applications in surgery simulation even real-time performance was achieved [11].

7.3.2. Comparison to State-of-the-Art Models

In the following, the deformation results of the developed soft-tissue model are compared to a thin-plate-splines deformation, as an exemplary interpolation-based method, as well as to the ANACONDA-algorithm, as an exemplary state-of-the-art image-based deformation model.
When comparing the deformation results for different deformation models, it always has to be considered, that different models require different kind of input. Since the input information can have a high influence on the deformation results, this is an important to consider, when interpreting differences between model performances.

The developed soft-tissue model requires as minimum input an image of the patient anatomy with segmentations of the bones, as well as the rigid transformations of each individual bones. The rigid transformations could in principle be depicted by a minimum of three landmarks per bone. For the presented deformation results, the deformation input for the bones is taken from a biomechanical registration of the skeleton (Sec. 4.2.1,) between the planning CT and the fraction or respectively post-treatment CT. The bone transformations were directly imposed on each voxel associated with the respective bone. The parameterization of soft-tissue is automatically derived from the input image, by a material transfer function.

The comparison of the soft-tissue model to a TPS-model, is based on the small-range deformation of patient 1 (Sec. 6.3.1). The thin-plate-splines (TPS) deformation requires as input a distribution of control points. The bone transformations, used as input for the soft-tissue model, are therefore approximated by landmarks which are placed on the bones' surfaces. For each bone, five landmarks are used, the transformations for these landmarks are obtained from the same biomechanical registration of the skeleton, which provided the input for the soft-tissue model.
The TPS-model performs well in proximity of the given control points. However, in regions with a low landmark density, larger deviations to the target image occur. Since the chosen landmarks on the bone surfaces do not result in a regular distribution of control points, the TPS struggles with the scarce input of only bone transformations (Fig. 38, upper row).
The developed soft-tissue model can cope with the minimal deformation input of bone transformations, due to its capability to consider the information of tissue heterogeneity during the deformation process. In regions too far away from the bone input, however, also for the soft-tissue model, the model performance declines. This is expected, since not all soft-tissue deformations can be traced back solely to bone transformations (Fig. 38, lower row).
In the TPS-transformation, the information of tissue heterogeneity is not considered. Between the given control points, soft-tissue deformations are simply interpolated as rigid as possible. This prevents unphysical behavior like grid folding or extreme volume changes. However, a regular DVF not necessarily corresponds to anatomical correct deformations. Since the TPS does not consider varying tissue elasticity in heterogeneous tissue, even the volume of rigid tissue like the bones is not necessarily conserved. For example, the TPS interpolates the deformations between humerus and scapula, by allowing small volume changes within both bones (Fig. 38b).
In contrast to that, the developed soft-tissue model, keeps the volume of bones strictly constant (Fig. 38e). This, in turn, results in small areas of grid folding, which for the example of humerus and scapula are located at the position of the shoulder joint. This example shows that even the absence of grid folding is not sufficient to determine the biofidelity of a deformation. At the same time, the occurrence of grid folding not necessarily is an indicator for erroneous deformations. For judging the biofidelity of a deformation, the anatomical context always has to be considered.
The computation times of the TPS are in the order of seconds, i.e. lower than for the soft-tissue model. However, for modeling large-range deformations as those depicted by the patient data set of patient 2, the TPS requires a higher number of input control points, which in turn will increase the computation times. Therefore, the developed soft-tissue model obtains better results concerning the computation time and modeled deformation behavior for modeling multi-range deformations.

The comparison of the soft-tissue model to the ANACONDA-algorithm is based on the large-range deformation of patient 2 (Sec. 6.3.2). The ANACONDA-algorithm combines image information, i.e. intensities, with the anatomical information provided by bone contours [86]. Additionally to the image input, the contours of skull, humeri and scapulae are used, which represent those areas in the image, where the largest deformations occur.

In principle, soft-tissue details should be better aligned than with the developed soft-tissue model, due to the explicit registration of soft-tissue. However, the deformations results showed that despite the consideration of the bone contours, the humerus and the surrounding soft-tissue are strongly distorted by the ANACONDA-transformation (Fig. 39b). Although the model is stated to be suitable for large-range deformations [86], extreme deformations like the one depicted by the data set of patient 2, cannot be modeled. The information of image intensities, used for the soft-tissue registration, is not sufficient, the model misses the consideration of tissue elasticity in the heterogeneous soft-tissue. This, in combination with an explicit optimization of grid regularity, results in the observed strong and non-volume conserving deformation of the bones. The computation times of the ANACONDA-algorithm are >1 h for the investigated data set. Therefore, the developed soft-tissue model obtains better results concerning the computation time, as well as concerning the biofidelity of the deformations.

Both, the TPS and ANACONDA show that for scarce model input (TPS) and large-range deformations (ANACONDA) the consideration of different elasticity in heterogeneous soft-tissue is indispensable for anatomically correct deformations. Both deformation algorithms have a strong focus on preserving the grid regularity. In anatomical regions, where no grid regularity is expected, e.g. in the shoulder joint, this results in wrong deformation of the surrounding tissue, e.g. in the observed distortions of bones. Therefore, the developed soft-tissue model yields deformation results with higher biofidelity, although the soft-tissue is deformed solely based on the deformation input from the bones, and not explicitly optimized by registration. Further improvement of the alignment of soft-tissue details is expected from embedding the developed model into a registration algorithm which explicitly optimizes the soft-tissue, while still limiting the deformations to anatomical reasonable ones.

7.3.3. Deformation Ranges

The developed deformation model is capable of handling small-range deformations as occur between different fractions, as well as large-range deformations as can occur between images of different modalities. Therefore, it is more flexibility than most state-of-the-art models. Most FE-models are limited to the linear elastic regime, i.e. deformation in the order of interfractional changes [34, 37]. A transfer to the non-linear regime, usually goes along with a strong increase in the computation times. For mass-spring models, large deformations also result in very high computation times, due to the interactive integration pattern for solving the underlying differential systems of equations. [38].
The developed soft-tissue model is capable to model the large-range as well as the small-range deformations by the same basic concepts. For the large-range deformation (Fig. 34), the deformation results showed more areas with DVF irregularities, as well as more artifacts in the artificially deformed images, in comparison to the small-range deformation (Fig. 33). This observation is in accordance with the findings of Varadhan et al. [47], who showed that the performance of DIR is strongly dependent on the magnitude of the described deformation, for a deformable bladder phantom.
For the developed model it is expected that all deformation magnitudes can be modeled according to the concepts presented in this work. The quality of the deformation results for large-range deformations is expected to be improved by improved deformation input for the bones (Sec. 6.1.1), as well as by additional model input, e.g. from the patient outline.

7.4. Model Applications

The two main concepts for applying deformation models in radiotherapy, are forward deformation and image registration. The soft-tissue model developed in this work executes forward deformations, but could in principle be embedded into an image registration algorithm. To approximate registration scenarios even for forward deformations, the model input was taken from a biomechanical image registration of the skeleton (Sec. 4.2.1). By coupling the soft-tissue deformation model to the kinematic model, which performs the skeleton registration, results in a biomechanical deformation model for the HN-region.
In general, the transfer of deformation models to clinical applications is slowed down by the missing gold standard for model evaluation [43]. To make the developed model suitable for clinical applications, a more detailed model evaluation is required. The evaluation should include further investigation of the model accuracy, e.g. by DICE-coefficients, as well as an evaluation of the overall model performance by comparison to physical and computational phantoms (Sec. 2.3.2). Moreover, additional model input should be included, especially the patient outline is expected to further improve the presented deformation results. Depending on the specific anatomical site and application, also the tumor outline could be considered for model input (Sec. 6.1.1).

7.4.1. Forward Deformation

For forward deformation modeling, no image-based deformation input is available. Therefore, it is important that the used input information is anatomically correct. The developed model, is very flexible concerning the deformation input it can take. For the exemplary HN-data sets, anatomically correct input was ensured by the coupling to a kinematic skeleton model, which describes anthropomorphic deformations (Sec. 4.2.1).
One important application of forward deformations by the developed model is the creation of computational phantoms (Sec. 2.3.2). These are required for benchmarking DIR algorithms during quality assurance [3, 41]. For virtual phantom creation, the deformation has to show a high biofidelity, i.e. correspond to the underlying physiological changes. Moreover, the deformation behavior should not be biased towards a specific deformation concept, to prevent bias during benchmarking. The developed soft-tissue model achieves a high biofidelity, due to the usage of anatomically correct deformation input (Sec. 6.1.1) and the consideration of tissue heterogeneity during the deformation process. By combining the anatomical information of the kinematic model and of the soft-tissue heterogeneity with the geometric deformation rules of the CM-concept, different concepts are united. This diminishes the bias towards a specific deformation concept, similarly to the computational phantoms developed by Pukala et al. [41].
The combined soft-tissue and skeleton model is also able to advance the possibilities of the construction of plan libraries. Typical anatomical changes occurring during fractionated radiotherapy, like a shoulder elevation (Sec. 6.2.2), can be constructed based on the patient-specific planning CTs. Since the artificially deformed CTs are used for dose calculation, it is even more important to obtain reliable images, than for the creation of virtual phantoms. In this context, the developed model shows a higher biofidelity than e.g. image-based and interpolation-based models. When applying additional deformation input, e.g. from the patient outline, to further improve the accuracy of the deformation results, the model can provide the patient images required for the creation of plan libraries. In case of volume changes being present, the interpolation of HU-values will have to be adjusted during the resampling process (Sec. 4.2.5). If this is not considered, the artificial images will show appearing and disappearing tissue, instead of

volume changes and dose calculation would yield wrong results [66].
And finally, in the new field of machine learning, the artificially deformed images can be used for data augmentation. The information provided by a single patient data set can be multiplied by creating artificial posture changes. In this way, less overall patient data is required, and the effort for data processing can be reduced. For data augmentation, the requirements to the quality of the deformed images strongly depends on the focus specific applications and will have to be defined based on the goal of the machine learning approaches.

7.4.2. Deformable Image Registration

Currently, only the input for the soft-tissue deformation model is generated by a true image registration, the soft-tissue itself is forwardly deformed according to the provided deformation input. In the light of the fact, that the soft-tissue deformations are approximated only by the skeletal input, no perfect alignment of soft-tissue is expected. However, especially for the small deformation, despite the limited model input, a good soft-tissue alignment is achieved (Sec. 6.2.1). Due to the low computation times of the model, the implementation into a registration algorithm is expected to be computationally feasible. Optimization of soft-tissue deformations will further improve the deformation results.
The main applications of deformable image registration in adaptive radiotherapy are contour propagation and dose accumulation (Sec. 2.3.3). The main advantages of the developed soft-tissue model for these applications are the low computation times and the high biofidelity of the deformation results.

For an application in contour propagation, the accuracy of the soft-tissue-model will have to be evaluated in more detail. In general, deformation methods that include image information, i.e. true registration-algorithms like the ANACONDA-algorithm, might be suited better for this kind of application. Such registrations achieve a high local accuracy, for specific contrast-rich anatomical features.
The strength of the developed soft-tissue model, however, is to achieve a high biofidelity for global deformations, even in low-contrast regions. The high resolution of the CM-grid allows to model deformations on voxel-level. The direct connections between neighboring CM-elements allows the propagation of deformations even into regions with low soft-tissue contrast. And finally, soft-tissue heterogeneity is considered on voxel-level.
For applications in dose accumulation, all the above mentioned aspects are highly relevant, since the accuracy of dose accumulation was shown to correlate with DVF consistency [70]. In this work, the consistency of the DVF, as measured by the Jacobian determinant, was strongly improved by the introduction of new model features (Chap. 5).
Tilly et al. [69] stated, that for deformation fields applied in dose warping, the Jacobian determinant has to be positive, in all relevant anatomical regions. In this work it was shown, that this general statement has to be relativized. The presented deformation results show that also negative Jacobians can be anatomically reasonable (Sec. 7.2.5). Sliding motion, which results in extreme volume changes, or grid folding, occurs not only for breathing motion, but also in joints or for the scapula sliding along the rib-cage. Therefore, a negative Jacobian determinant, or extreme Jacobian values not necessarily indicate unphysical deformations, but have to be interpreted in the anatomical context.
In any case, all DVF irregularities have to be carefully evaluated for their influence on dose accumulation. The effect of grid folding and extreme volume changes in individual voxels has to be considered in the context of the explicitly applied dose accumulation methods [95].

Overall, the DVF consistency has been strongly improved by introducing new model concepts into the CM-approach. The accuracy of the soft-tissue model will have to be evaluated in more detail, and if necessary improved by using additional model input. To minimize the effort for creating additional deformation input, while maximizing its benefit, an a-priori estimation of the required accuracy in different regions could be performed. As proposed by Saleh et al. [74], it can be estimated in which regions high-dose gradients occur, so that the model input has to be refined only in those regions.

8. Conclusion

Until now, most state-of-the-art deformation models that are used for radiotherapy applications either require high computation times or produce physically or anatomically unreasonable deformations. In this work, a soft-tissue deformation model was developed which exhibits low runtimes and, in contrast to commonly used image-based deformation methods, considers underlying tissue properties.
The model is based on the chainmail (CM)-approach [1, 2], which was tailored to radiotherapy applications by introducing three novel basic concepts. Rotational degrees of freedom were introduced into the CM-approach, as well as a concept for handling multiple deformation initiators to address global deformation input, and a concept for handling model input from anatomical structures. The resulting improvement of the characteristic deformation behavior was demonstrated based on two exemplary head-and-neck patients, which represented two different deformation ranges. The first patient showed an interfractional deformation in the order of a few millimeters, the second patient showed an extreme deformation from an arms-up to an arms-down positioning. For both patients, the physical and anatomical plausibility of the generated displacement vectorfields (DVFs) improved, as was illustrated qualitatively by Jacobian maps and measured quantitatively by characteristic values of the overall Jacobian distribution. The improved deformation behavior resulted in realistic artificially deformed CT images.
Computation times of the developed model are in the order of 30 min for single-threaded calculation of a DVF on voxel-level. By simple code parallelization, runtimes in the order of 1 min can be expected, by more complex code parallelization, even real-time deformations can be achieved [11]. It was shown that the computation times have a low dependency on the deformation magnitude, in contrast to most physical-based models.
The final model concept does not completely prevent DVF irregularities. However, it was shown that deformation models which focus on globally maintaining the DVF regularity, like the thin-plate-splines or the ANACONDA-algorithm, result in unphysiological deformations like distorted bones. Therefore, the general statement that the occurrence of DVF irregularities and grid folding indicates unphysical deformation behavior has to be revisited. As the presented results indicate, grid folding can also result from anatomically reasonable sliding motion, not only in the lung but also e.g. in joints or for the scapula sliding along the rib-cage. Therefore, neither a negative Jacobian determinant nor extreme Jacobian values necessarily indicate unphysical deformations. Instead, their meaning has to be interpreted in the specific anatomical context, e.g. by means of Jacobian maps.
The high flexibility of the developed soft-tissue model concerning the deformation input was proven by coupling it to a kinematic skeleton model for the head and neck (HN) region [3]. Additional input, e.g from the patient outline or from various organ models can easily be included. The combined model was capable to produce realistic artificially deformed CTs by forward deformation. This offers the possibility to contribute to the generation of virtual phantoms, to the generation of patient-specific plan libraries, as well as to data augmentation in deep learning.

Outlook Although the model development was focused to the head-neck region, the model concept can easily be extended to other parts of the body. The next step, after modeling the soft-tissue connecting rigid bones in the head and neck region, will be to consider more complex deformation input. For the abdominal region, various specialized organ models e.g. for liver, bladder or lung exist. However, a model describing the deformations in the remaining tissue that links the individual organs is missing. The developed soft-tissue model has the potential to close

this gap by linking the information of the different organ models to provide a DVF covering the whole abdomen.
Concerning the considered imaging modalities, the soft-tissue model was focused to CT images. However, the model concepts can also be transferred to other imaging modalities like MR. This offers the potential for multimodality image matching, even in the presence of large-range deformations as between the illustrated arms-up, arms-down postures. Especially in the upcoming field of MR-guidance, multimodality deformations will be of use for the generation of pseudo CTs.
In adaptive radiotherapy, the developed soft-tissue deformation model is envisioned to contribute to more accurate dose accumulation. To achieve this goal, first a more detailed model evaluation based not only on two patients but on a whole patient population has to be performed. Then the remaining irregularities observed for the soft-tissue model have to be addressed. For this, the implementation of a direct volume control to describe volume conservation as well as volume growth and shrinkage is expected to achieve further improvements. And finally, an explicit optimization of the soft-tissue deformations by image registration is expected to increase the model accuracy to the requirements of high-precision adaptive radiotherapy.

A. Appendix

A.1. Quaternions

A quaternion is represented in the form

$$\mathbf{q} = q_0 + \mathbf{i}q_1 + \mathbf{j}q_2 + \mathbf{k}q_3 \tag{A.1}$$

with $q_0, q_1, q_2, q_3 \in \mathbb{R}$ and $\mathbf{i}^2 = \mathbf{j}^2 = \mathbf{k}^2 = \mathbf{ijk} = -1$ [96].

When representing a rotation, a quaternion can be derived from the rotation angle α and the rotation axis $\mathbf{a}$ in the following:

$$\begin{aligned} q_0 &= \cos(\frac{\alpha}{2}) \\ q_1 = a_x \cdot \sin(\frac{\alpha}{2}), &\quad q_2 = a_y \cdot \sin(\frac{\alpha}{2}), \quad q_3 = a_z \cdot \sin(\frac{\alpha}{2}). \end{aligned} \tag{A.2}$$

An ordinary vector $\mathbf{p} = (p_x, p_y, p_z)$ is represented as $\mathbf{p} = p_x\mathbf{i} + p_y\mathbf{j} + p_z\mathbf{k}$ with $q_0 = 0$. A rotation of such a vector is then calculated by:

$$\mathbf{p}' = \mathbf{q} \cdot \mathbf{p} \cdot \mathbf{q}^{-1} \tag{A.3}$$

List of Publications

Peer-Reviewed Articles

H. Teske, K. Bartelheimer, J. Meis, R. Bendl, E.M. Stoiber, K. Giske (2017). Construction of a biomechanical head and neck motion model as a guide to evaluation of deformable image registration. *Physics in Medicine and Biology* 62.12: N271-N284

Conference Articles

K. Bartelheimer, H. Teske, R. Bendl, K. Giske (2017). Tissue-Specific Transformation Model for CT-images. *Current Directions in Biomedical Engineering* 3.2: 525-528

H. Teske, K. Bartelheimer, R. Bendl, E.M. Stoiber, K. Giske (2017). Handling of patient postures in arms up and arms down position using a biomechanical skeleton model. *Current Directions in Biomedical Engineering* 3.2: 469-472

Conference Abstracts

K. Bartelheimer, H. Teske, A. Czekalla, K. Giske (2019). Anthropomorphic Chainmail for Fast Soft-Tissue Deformation in Human Anatomies. *BiGART2019, Aarhus, Denmark* (Poster)

K. Bartelheimer, H. Teske, R. Bendl, K. Giske (2017). Tissue-Specific Transformation Model for CT-images. *DGMP Tagung, Dresden, Germany* (Poster)

K. Bartelheimer, H. Teske, R. Bendl, K. Giske (2017). Soft Tissue Modeling with the Chainmail Approach. *BVM 2017, Heidelberg, Germany* (Talk)

K. Bartelheimer, J. Merz, H. Teske, R. Bendl, K. Giske (2016). Application of the Enhanced ChainMail algorithm with inter-element rotation in adaptive radiotherapy *Estro 35, Turin, Italy* (Poster)

Bibliography

[1] S. F. Gibson. "3D ChainMail: A fast algorithm for deforming volumetric objects". In: *Proceedings of the 1997 Symposium on Interactive 3D Graphics* 97 (1997), pp. 149–154.

[2] M. Schill. "Biomechanical soft tissue modeling–techniques, implementation and applications". PhD thesis. 2001.

[3] H. Teske et al. "Construction of a biomechanical head and neck motion model as a guide to evaluation of deformable image registration". In: *Phys Med Biol* 62.12 (2017), N271–N284.

[4] H. Teske. "Articulated patient model in high-precision radiation therapy". PhD thesis. Universität Heidelberg, 2019.

[5] A. J. Lomax. "Intensity modulated proton therapy and its sensitivity to treatment uncertainties 2: The potential effects of inter-fraction and inter-field motions". In: *Physics in Medicine and Biology* 53.4 (2008), pp. 1043–1056.

[6] S. van Kranen et al. "Setup Uncertainties of Anatomical Sub-Regions in Head-and-Neck Cancer Patients After Offline CBCT Guidance". In: *International Journal of Radiation Oncology* Biology* Physics* 73.5 (2009), pp. 1566–1573.

[7] J. L. Barker et al. "Quantification of volumetric and geometric changes occurring during fractionated radiotherapy for head-and-neck cancer using an integrated CT/linear accelerator system". In: *International Journal of Radiation Oncology*Biology*Physics* 59.4 (2004), pp. 960–970.

[8] P. Castadot et al. "Adaptive Radiotherapy of Head and Neck Cancer". In: *Seminars in Radiation Oncology* 20.2 (2010), pp. 84–93.

[9] A. Sotiras, C. Davatzikos, and N. Paragios. "Deformable medical image registration: A survey". In: *IEEE Transactions on Medical Imaging* 32.7 (2013), p. 1153.

[10] M. a. Schill et al. "Biomechanical simulation of the vitreous humor in the eye using an enhanced chainmail algorithm". In: *Miccai98* Lecture No (1998), pp. 679–687.

[11] A. Rodríguez, A. León, and G. Arroyo. "Parallel deformation of heterogeneous ChainMail models Application to interactive deformation of large medical volumes - 2016 - Rodriguez, Leon, Arroyo.pdf". In: *Computers in Bi* 79 (2016), pp. 222–232.

[12] C. P. Karger. "Der Strahlentherapie-Prozess". In: *Medizinische Physik*. Springer, 2018, pp. 399–404.

[13] R. Mohan and Bort. "The potential and limitations of IMRT: a physicist's point of view". In: *Image-Guided IMRT*. Springer, 2006, pp. 11–18.

[14] O. Jäkel. "Bildgebung für die Strahlentherapie". In: *Medizinische Physik*. Springer, 2018, pp. 473–484.

[15] V Grégoire and T. Mackie. "State of the art on dose prescription, reporting and recording in intensity-modulated radiation therapy (ICRU report No. 83)". In: *Cancer/Radiotherapy* 15.6-7 (2011), pp. 555–559.

[16] L. A. Dawson and M. B. Sharpe. "Image-guided radiotherapy: rationale, benefits, and limitations". In: *The lancet oncology* 7.10 (2006), pp. 848–858.

[17] D. Yan et al. "Adaptive radiation therapy". In: *Physics in Medicine and Biology* 42.1 (1997), pp. 123–132.

[18] J. C. O'Daniel et al. "Parotid Gland Dose in Intensity-Modulated Radiotherapy for Head and Neck Cancer: Is What You Plan What You Get?" In: *International Journal of Radiation Oncology* Biology* Physics* 69.4 (2007), pp. 1290–1296.

[19] C. Lee et al. "Assessment of Parotid Gland Dose Changes During Head and Neck Cancer Radiotherapy Using Daily Megavoltage Computed Tomography and Deformable Im-

age Registration". In: *International Journal of Radiation Oncology* Biology *Physics* 71.5 (2008), pp. 1563–1571.

[20] E. K. Hansen et al. "Repeat CT imaging and replanning during the course of IMRT for head-and-neck cancer". In: *International Journal of Radiation Oncology* Biology* Physics* 64.2 (2006), pp. 355–362.

[21] B. Van Asselen et al. "The dose to the parotid glands with IMRT for oropharyngeal tumors: The effect of reduction of positioning margins". In: *Radiotherapy and Oncology* 64.2 (2002), pp. 197–204.

[22] D. L. Schwartz et al. "Adaptive radiotherapy for head-and-neck cancer: Initial clinical outcomes from a prospective trial". In: *International Journal of Radiation Oncology Biology Physics* 83.3 (2012), pp. 986–993. arXiv: `NIHMS150003`.

[23] Q. Wu et al. "Adaptive Replanning Strategies Accounting for Shrinkage in Head and Neck IMRT". In: *International Journal of Radiation Oncology Biology Physics* 75.3 (2009), pp. 924–932.

[24] J. Castelli et al. "Impact of head and neck cancer adaptive radiotherapy to spare the parotid glands and decrease the risk of xerostomia." In: *Radiation oncology (London, England)* 10.1 (2015), p. 6.

[25] D. L. Schwartz et al. "Adaptive radiotherapy for head and neck cancer - Dosimetric results from a prospective clinical trial". In: *Radiotherapy and Oncology* 106.1 (2013), pp. 80–84.

[26] E. Brown et al. "Predicting the need for adaptive radiotherapy in head and neck cancer". In: *Radiotherapy and Oncology* 116.1 (2015), pp. 57–63.

[27] T. W. Sederberg and S. R. Parry. "Free-Form Deformation of Solid Geometric Models". In: *ACN SIGGRAPH computer graphics* 20.4 (1986), pp. 151–160.

[28] M. Velec and K. K. Brock. "Biomechanical Modeling Applications in Image-Guided Radiotherapy". In: *Biomechanics of Soft Tissue*. 2018, pp. 117–144.

[29] F. L. Bookstein. "Principal Warps: Thin-Plates Splines and the decompostion of deformations". In: *IEEE Transactions on Pattern Analysis and Machine Intelligence* 11.6 (1989), pp. 567–585.

[30] D. Rueckert et al. "Nonrigid registration using free-form deformations: application to breast MR images." In: *IEEE Transactions on Medical Imaging* 18.8 (1999), pp. 712–21.

[31] L. P. Nedel and D. Thalmann. "Real time muscle deformations using mass-spring systems". In: *Proceedings - Computer Graphics International, CGI 1998* (1998), pp. 156–165.

[32] J. P. Da Silva, G. A. Giraldi, and A. L. Apolinário. "A new optimization approach for mass-spring models parameterization". In: *Graphical Models* 81 (2015), pp. 1–17.

[33] R. Varadhan et al. "A framework for deformable image registration validation in radiotherapy clinical applications". In: *Journal of Applied Clinical Medical Physics* 14.1 (2013), pp. 192–213.

[34] A. Al-Mayah et al. "Biomechanical-based image registration for head and neck radiation treatment." In: *Physics in medicine and biology* 55.21 (2010), pp. 6491–6500.

[35] A. Al-Mayah et al. "Radiation dose response simulation for biomechanical-based deformable image registration of head and neck cancer treatment". In: *Physics in Medicine and Biology* 60.21 (2015), pp. 8481–8489.

[36] K. K. Brock et al. "Accuracy of finite element model-based multi-organ deformable image registration;" in: *Medical Physics* 32.6 (2005), pp. 1647–1659.

[37] J. Kim et al. "A finite element head and neck model as a supportive tool for deformable image registration". In: *International Journal of Computer Assisted Radiology and Surgery* 11.7 (2016), pp. 1311–1317.

[38] J. Neylon et al. "A GPU based high-resolution multilevel biomechanical head and neck model for validating deformable image registration". In: *Medical Physics* 42.1 (2015), pp. 232–243.

[39] F. P. Vidal, P.-F. Villard, and É. Lutton. "Tuning of Patient-Specific Deformable Models Using an Adaptive Evolutionary Optimization Strategy". In: *IEEE Transactions on Biomedical Engineering* 59.10 (2012), pp. 2942–2949.

[40] F. P. Vidal and P.-F. Villard. "Development and Validation of Real-time Simulation of X-ray Imaging with Respiratory Motion". In: *Computerized Medical Imaging and Graphics* 49 (2016), pp. 1–15.

[41] J. Pukala et al. "A virtual phantom library for the quantification of deformable image registration uncertainties in patients with cancers of the head and neck." In: *Medical physics* 40.11 (2013), p. 111703.

[42] D Gering et al. "Anatomy Driven Deformation". In: *Proceedings of the XVIth ICCR, Amsterdam, The Netherlands* (2010).

[43] C. Paganelli et al. ""Patient-specific validation of deformable image registration in radiation therapy: Overview and caveats"". In: *Medical Physics* 45.10 (2018), e908–e922.

[44] K. K. Brock et al. "Use of image registration and fusion algorithms and techniques in radiotherapy: Report of the AAPM Radiation Therapy Committee Task Group No. 132: Report". In: *Medical Physics* 44.7 (2017), e43–e76.

[45] R. Castillo et al. "A framework for evaluation of deformable image registration spatial accuracy using large landmark point sets". In: *Physics in Medicine and Biology* 54.7 (2009), pp. 1849–1870.

[46] K. K. Brock. "Results of a Multi-Institution Deformable Registration Accuracy Study (MIDRAS)". In: *International Journal of Radiation Oncology Biology Physics* 76.2 (2010), pp. 583–596.

[47] R. Varadhan, T. Magome, and S. Hui. "Characterization of deformation and physical force in uniform low contrast anatomy and its impact on accuracy of deformable image registration". In: *Medical Physics* 43.1 (2016), pp. 52–61.

[48] A. Kumarasiri et al. "Deformable image registration based automatic CT-to-CT contour propagation for head and neck adaptive radiotherapy in the routine clinical setting". In: *Medical Physics* 41.12 (2014), p. 121712.

[49] L. Zhang et al. "The impact of robustness of deformable image registration on contour propagation and dose accumulation for head and neck adaptive radiotherapy". In: *Journal of Applied Clinical Medical Physics* 19.4 (2018), pp. 185–194.

[50] P. Castadot et al. "Comparison of 12 deformable registration strategies in adaptive radiation therapy for the treatment of head and neck tumors". In: *Radiotherapy and Oncology* 89.1 (2008), pp. 1–12.

[51] A. S. Mohamed et al. "Quality Asssurance Assessment of Diagnostic and Radiation Therapy – Simulation CT Image Registration for Head and Neck Radiation Therapy : Anatomic Region of Interest – based Comparison of Rigid and Deformable Algorithms". In: *Radiology* 274.3 (2015), pp. 752–763.

[52] W. Nobnop et al. "Evaluation of deformable image registration (DIR) methods for dose accumulation in nasopharyngeal cancer patients during radiotherapy". In: *Radiology and Oncology* 51.4 (2017), pp. 438–446.

[53] C. Fiorino et al. "Introducing the Jacobian-volume-histogram of deforming organs: application to parotid shrinkage evaluation." In: *Physics in Medicine and Biology* 56.11 (2011), pp. 3301–3312.

[54] E. Schreibmann et al. "A measure to evaluate deformable registration fields in clinical settings". In: *Journal of Applied Clinical Medical Physics* 13.5 (2012), pp. 126–139.

[55] R. Kashani et al. "Technical note: A physical phantom for assessment of accuracy of deformable alignment algorithms". In: *Medical Physics* 34.7 (2007), pp. 2785–2788.

[56] N. Kirby, C. Chuang, and J. Pouliot. "A two-dimensional deformable phantom for quantitatively verifying deformation algorithms". In: *Medical Physics* 38.8 (2011), pp. 4583–4586.

[57] Y. Liao et al. "An anthropomorphic abdominal phantom for deformable image registration accuracy validation in adaptive radiation therapy". In: *Medical Physics* 44.6 (2017), pp. 2369–2378.

[58] K. Singhrao, N. Kirby, and J. Pouliot. "A three-dimensional head-and-neck phantom for validation of multimodality deformable image registration for adaptive radiotherapy". In: *Medical Physics* 41.12 (2014), p. 121709.

[59] K. Nie et al. "Site-specific deformable imaging registration algorithm selection using patient-based simulated deformations". In: *Medical Physics* 40.4 (2013), p. 041911.

[60] R. B. Ger et al. "Accuracy of deformable image registration on magnetic resonance images in digital and physical phantoms". In: *Medical Physics* 44.10 (2017), pp. 5153–5161.

[61] K. S. Chao et al. "Reduce in Variation and Improve Efficiency of Target Volume Delineation by a Computer-Assisted System Using a Deformable Image Registration Approach". In: *International Journal of Radiation Oncology Biology Physics* 68.5 (2007), pp. 1512–1521.

[62] N. Hardcastle et al. "A multi-institution evaluation of deformable image registration algorithms for automatic organ delineation in adaptive head and neck radiotherapy". In: *Radiation Oncology* 7.1 (2012), p. 90.

[63] G. Loi et al. "Performance of commercially available deformable image registration platforms for contour propagation using patient-based computational phantoms: A multi-institutional study: A". In: *Medical Physics* 45.2 (2018), pp. 748–757.

[64] C. Veiga et al. "Toward adaptive radiotherapy for head and neck patients: Feasibility study on using CT-to-CBCT deformable registration for "dose of the day" calculations". In: *Medical Physics* 41.3 (2014), pp. 1–12.

[65] I. J. Chetty and M. Rosu-Bubulac. "Deformable Registration for Dose Accumulation". In: *Seminars in Radiation Oncology* 29.3 (2019), pp. 198–208.

[66] C. Veiga et al. "Toward adaptive radiotherapy for head and neck patients : Uncertainties in dose warping due to the choice of deformable registration algorithm Toward adaptive radiotherapy for head and neck patients : Uncertainties in dose warping due to the choice of def". In: *Medical Physics* 42.2 (2015), pp. 760–769.

[67] K. Nie et al. "Performance variations among clinically available deformable image registration tools in adaptive radiotherapy - How should we evaluate and interpret the result?" In: *Journal of Applied Clinical Medical Physics* 17.2 (2016), pp. 328–340.

[68] B. Rigaud et al. "Evaluation of deformable image registration methods for dose monitoring in head and neck radiotherapy". In: *BioMed Research International* 2015 (2015).

[69] D. Tilly, N. Tilly, and A. Ahnesjö. "Dose mapping sensitivity to deformable registration uncertainties in fractionated radiotherapy - applied to prostate proton treatments". In: *BMC medical physics* 13.1 (2013), p. 2.

[70] E. T. Bender, N. Hardcastle, and W. A. Tomé. "On the dosimetric effect and reduction of inverse consistency and transitivity errors in deformable image registration for dose accumulation". In: *Medical Physics* 39.1 (2012), pp. 272–280.

[71] F. J. Salguero et al. "Estimation of three-dimensional intrinsic dosimetric uncertainties resulting from using deformable image registration for dose mapping". In: *Medical Physics* 38.1 (2011), pp. 343–353.

[72] M. J. Murphy et al. "A method to estimate the effect of deformable image registration uncertainties on daily dose mapping". In: *Medical Physics* 39.2 (2012), pp. 573–580.

[73] J. Pukala et al. "Benchmarking of five commercial deformable image registration algorithms for head and neck patients". In: *Journal of Applied Clinical Medical Physics* 17.3 (2016), pp. 25–40.

[74] N. K. Saleh-Sayah et al. "A distance to dose difference tool for estimating the required spatial accuracy of a displacement vector field". In: *Medical Physics* 38.5 (2011), pp. 2318–2323.

[75] A. Rodríguez Aguilera et al. "A parallel resampling method for interactive deformation of volumetric models". In: *Computers and Graphics* 53 (2015), pp. 147–155.

[76] T. L. Le Fol, O. Acosta-Tamayo, and P. Haigron. "Angioplasty simulation using ChainMail method". In: *Medical Imaging 2007: Visualization and Image-Guided Procedures*. 2007, p. 65092X.

[77] Y. Li and K. Brodlie. "Soft Object Modelling with Generalised ChainMail - Extending the Boundaries of Web-Based Graphics". In: *Computer Graphics Forum*. Vol. 22. 4. 2003, pp. 717–727.

[78] F Roessler, T. Wolff, and T. Ertl. "Direct GPU-based Volume Deformation". In: *Proceedings of CURAC* D (2008), pp. 65–68.

[79] A. Rodríguez et al. "SP-ChainMail: a GPU-based sparse parallel ChainMail algorithm for deforming medical volumes". In: *The Journal of Supercomputing* 71.9 (2015), pp. 3482–3499.

[80] S. F. Frisken-Gibson. "Using linked volumes to model object collisions, deformation, cutting, carving, and joining". In: *IEEE Transactions on Visualization and Computer Graphics* 5.4 (1999), pp. 333–348.

[81] F Baumgart. "Stiffness - an unknown world of mechanical science?" In: *Injury-International Journal for the Care of the Injured* 31.2 (2000), pp. 14–23.

[82] J. Zhang et al. "A new ChainMail approach for real-time soft tissue simulation". In: *Bioengineered* 7.4 (2016), pp. 246–252.

[83] K. Giske et al. "Local setup errors in image-guided radiotherapy for head and neck cancer patients immobilized with a custom-made device". In: *International Journal of Radiation Oncology Biology Physics* 80.2 (2011), pp. 582–589.

[84] K. Clark et al. "The cancer imaging archive (TCIA): Maintaining and operating a public information repository". In: *Journal of Digital Imaging* 26.6 (2013), pp. 1045–1057.

[85] W. R. Bosch et al. *Data from Head-Neck_ Cetuximab. The Cancer Imaging Archive*. 2015.

[86] O. Weistrand and S. Svensson. "The ANACONDA algorithm for deformable image registration in radiotherapy". In: *Medical Physics* 42.1 (2015), pp. 40–53. arXiv: `arXiv:1011.1669v3`.

[87] C. C. Bordt. "Analysis of the Displacement Vector Fields in Radiotherapy by Means of the Jacobian Determinant". Bachelor Thesis. University of Heidelberg, 2019.

[88] R. Bendl, A. Hoess, and W. Schlegel. "Virtual simulation in radiotherapy planning". In: *International Conference on Computer Vision, Virtual Reality and Robotics in Medicine*. 1995.

[89] H. Teske et al. "Handling images of patient postures in arms up and arms down position using a biomechanical skeleton model". In: *Current Directions in Biomedical Engineering* 3.2 (2017), pp. 469–472.

[90] D. L. Saenz et al. "The level of detail required in a deformable phantom to accurately perform quality assurance of deformable image registration". In: *Physics in Medicine and Biology* 61.17 (2016), pp. 6269–6280.

[91] J. Y. Zhang et al. "Patient-specific computational biomechanics of the brain without segmentation and meshing". In: *International Journal for Numerical Methods in Biomedical Engineering* 29 (2013), pp. 293–308.

[92] M. Li et al. "Patient-specific biomechanical model as whole-body CT image registration tool". In: *Medical Image Analysis* 22.1 (2015), pp. 22–34.

[93] D. Valtorta and E. Mazza. "Dynamic measurement of soft tissue viscoelastic properties with a torsional resonator device". In: *Medical Image Analysis* 9.5 (2005), pp. 481–490.

[94] B. Karaçalı and C. Davatzikos. "Estimating Topology Preserving and Smooth Displacement Fields". In: *IEEE Transactions on Medical Imaging* 23.7 (2004), pp. 868–880.

[95] H. S. Li et al. "Direct dose mapping versus energy/mass transfer mapping for 4D dose accumulation: fundamental differences and dosimetric consequences." In: *Physics in medicine and biology* 59 (2014), pp. 173–188.

[96] E. B. Dam, M. Koch, and M. Lillholm. *Quaternions, Interpolation and Animation*. Citeseer, 1998.

Acknowledgments

I would like to thank Prof. Oliver Jäkel for the opportunity to carry out my thesis in the division of *Medical Physics in Radiation Oncology* at the German Cancer Research Center. Thanks to him and to Prof. Joao Seco for being the referees for this thesis. I also thank Prof. Rüdiger Klingeler and Prof. Björn-Malte Schäfer for being part of my examination committee.

I especially want to thank Kristina, who offered me the possibility to become part of the group *Computational Patient Models* and to pursue this interesting topic in model development. Thanks for fruitful discussions and feedback, as well as for providing a nice group atmosphere. Thanks to Hendrik, for providing the puppet master, for discussing directions of coordinate systems with me again and again, and for answering all my virtuos/c++/.. questions. I also would like to thank all other members of E0401 for the nice working atmosphere.

Thanks to Oli and Kathrin, for being great office mates, and also to Nina, Kai and Christian for the great times we had during the last years, on conferences, during the "Weiterbildung" and during running, coffee and mensa breaks.

Finally, I wish to thank my family for supporting me on my whole way to accomplishing this thesis. And last but not least, thank you Jo - for your great support, especially during this last year!